Small Engine Technology
Task 4: Advanced Small Turboshaft Compressor (ASTC) Performance and Range Investigation

Jeff L. Hansen and Robert A. Delaney
Allison Engine Company
Indianapolis, Indiana

March 1997

**National Aeronautics and
Space Administration**

CONTENTS

i

LIST OF FIGURES

LIST OF TABLES

1.0 SUMMARY

This contract had two main objectives involving both numerical and experimental investigations of a small highly loaded two-stage axial compressor designated Advanced Small Turboshaft Compressor (ASTC) which had a design pressure ratio goal of 5:1 at a flowrate of 10.53 lbm/s. The first objective was to conduct 3-D Navier-Stokes multistage analyses of the ASTC using several different flow modelling schemes. The second main objective was to complete a numerical/ experimental investigation into stall range enhancement of the ASTC. This compressor was designed under a cooperative Space Act Agreement and all testing was completed at NASA Lewis Research Center.

For the multistage analyses, four different flow model schemes were used, namely: (1) steady-state *ADPAC* analysis, (2) unsteady *ADPAC* analysis, (3) steady-state *APNASA* analysis, and (4) steady state *OCOM3D* analysis. The results of all the predictions were compared to the experimental data.

The steady-state *ADPAC* and *APNASA* codes predicted similar overall performance and produced good agreement with data, however the blade row performance and flowfield details were quite different. In general, it can be concluded that the *APNASA* average-passage code does a better job of predicting the performance and flowfield details of the highly loaded ASTC compressor.

The stall range enhancement investigation involved studies of forward sweep for the first stage rotor and a tandem vane configuration for the outlet guide vane. The forward swept rotor was designed with the use of *ADPAC* and was tested at NASA Lewis Research Center in the same rig as the baseline rotor. The test results showed that the forward swept design had a large performance improvement over the baseline rotor with twice the high speed stall margin and four percent higher off-design efficiency.

For the tandem vane investigation, a parametric study was conducted to determine if a tandem vane could provide performance benefits over a conventional design of the ASTC second stage stator. No tandem configuration was found that had lower design point loss than the conventional design. However, it was determined that a tandem vane configuration maintains lower loss at off-design conditions extending it's stall range.

This Page Intentionally Left Blank

2.0 INTRODUCTION AND BACKGROUND

2.1 Introduction

Increased emphasis on improved fuel efficiency, reduced weight, and lower life cycle costs for turbofan and turboshaft engines has produced aggressive compression system design, performance and operability goals. Future fans and compressors will be required to have high stage loading to reduce the number of parts and engine length, cost and weight. However, high stage loading adversely affects efficiency because of attendant elevated shock, diffusion and secondary flow losses. In small machines and back stages of larger compressors, the efficiency penalty with high stage loading is amplified because regions of loss-producing viscous endwall, secondary, and tip clearance flows, driven by blade-to-blade pressure gradients, occupy a large portion of the flow passage. Efforts to reduce losses through the use of complex airfoil shapes have resulted in highly three-dimensional flows that are not adequately modeled with current-generation compressor design and analysis systems. High stage loading can also lead to stage mismatching because of significant rotor-stator interactions that are not accounted for in the design process. Therefore, to meet future compressor performance goals, there is a critical need to incorporate into the design process a 3-D Navier-Stokes multistage flow model with capability to model these 3-D and interactive flow phenomena.

Fan and compressor design systems have been evolving for over 50 years starting with the one dimensional fluid dynamics based designs used in the 1940's and 1950's. By the 1960's, 2D inviscid streamline throughflow calculations were available along with cascade test data derived correlations used for 2D blading. The introduction of blade-to-blade flow solvers with simple boundary layer models in the 1970's allowed designers to better optimize the 2D blade shapes. By the 1980's three dimensional Euler codes were used to analyze 3D airfoil shapes with the viscous blading effects accounted for by 2D Navier-Stokes solvers. Despite these flow modeling advances, empirical correlations derived from compressor test data was still relied upon to account for endwall, tip clearance and secondary flow effects. The introduction of faster computers and 3D viscous codes in the late 1980's allowed compression system designers to get a better understanding of the internal flow physics of a single blade row and rely less on empirical correlations. These 3D viscous codes became fairly reliable in the early 1990's for single stage fans or the first few blade rows of a multistage

compressor. However, blade row interaction effects and uncertain inlet boundary conditions for embedded stages render these isolated blade row codes nearly useless for multistage compressor design.

The latest evolution in compression system design is the development of viscous multistage CFD models that simultaneously solve multiple blade rows to include rotor-stator interaction effects. With the availability of more powerful computers it has become more practical to incorporate these models into compressor design systems. This allows the designer to evaluate new multistage design concepts and to progressively replace the empirical correlations with physics-based CFD models and to meet the future compression system goals.

This contract had two main objectives involving both numerical and experimental investigations of a small two-stage highly loaded axial compressor. The first objective was to conduct 3-D Navier-Stokes multistage analysis of this compressor using several different flow modelling schemes. The second main objective was a numerical and experimental investigation into stall range enhancement of the baseline compressor. This compressor has a design pressure ratio goal of 5:1 at a flowrate of 10.53 lbm/s and was designed with the use of a three-dimensional Navier-Stokes multistage code developed by Dr. John Adamczyk of NASA Lewis Research Center.

For the numerical performance analysis, three flow modeling schemes were used in addition to the Adamczyk average-passage code. Two of the performance predictions were obtained using the ADPAC analysis code. The ADPAC code is a general purpose code that solves the Reynolds-averaged Navier-Stokes equations using a proven time-marching formulation. Both multistage steady state and an unsteady flow solutions were obtained. A third analysis was obtained using the 3-D Navier-Stokes code OCOM3D. This code solves the full Navier-Stokes equations and was derived from the ARC3D code. The results of all the predictions were compared to the limited experimental data.

The stall range enhancement investigation utilized forward sweep in the first stage rotor and a tandem vane configuration for the outlet guide vane. The forward swept rotor design was completed with the use of ADPAC. The forward swept rotor was tested at NASA Lewis and the results compared to the baseline rotor test data. For the tandem vane investigation, a parametric study was conducted with ADPAC to determine if a tandem vane configuration could provide any performance benefits.

4

2.2 Baseline Compressor

The baseline compressor used in this study was designed under a 1991 Space Act Agreement Between Allison, NASA and the Army Propulsion Directorate. This agreement provided for the application of the *APNASA* multistage average-passage computational code to assess and design the highly loaded multistage Advanced Small Turboshaft Compressor (ASTC). Under this agreement Allison was to design and fabricate the compressor and NASA was to perform the *APNASA* analysis. In addition, NASA supported the test of this compressor in the Lewis Research Center's Small Compressor Test Cell. The final design and test results of this compressor are presented in this section.

2.2.1 Design

The compressor design was completed using Allison's Axial Compressor Design System with the guidance of the *APNASA* multistage code. This design system uses an axisymmetric, radial equilibrium, streamline curvature preliminary design module to conduct parametric studies on a wide range of design variables. This module establishes a reasonable approximation of the flow path, work distribution and blading parameters. The module uses correlations for profile and shock losses, deviation and tip clearance effects with the associated mixing losses. Through each step of the design, the airfoil shapes are updated to establish optimum configurations that can achieve the stage mass flow and work requirements with minimum loss. This process involves detailed analysis of the blade-to-blade flow, entrance region flow capacity, and blade surface boundary layers using 3D viscous single blade row models. Additionally, the aerodynamic design system is interfaced with the structural analysis system to provide structurally and aerodynamically sound airfoils.

For the design of the baseline compressor discussed here an additional iterative loop using the multistage *APNASA* code is included. This code was developed at NASA Lewis Research Center by Adamczyk (Ref 1-3) and solves the 3-D average-passage Navier-Stokes equations, which are obtained from the Reynolds-averaged form of the equations through the application of an averaging operator.

5

Averaging is first performed over the time period required for one rotor revolution. The resulting system of equations contains additional source terms with body forces, energy sources, energy correlations, and velocity correlations which account for the presence of neighboring blade rows. These additional terms must be appropriately modeled and require empirical modeling of the averaged turbulence effects, time-averaged effects, and passage-to-passage averaged effects. The resulting "average-passage" flow is steady relative to a given blade row and spatially periodic.

The *APNASA* results had considerable impact on design decisions concerning stage matching, flowpath and airfoil shapes of the ASTC. The resulting final design parameters are presented in Table 2-1. The compressor cross-section, shown in Figure 2-1, shows the design to have low aspect ratio blading, a constant outer diameter and variable inlet guide vanes (IGV) and first stator. The two rotors are integrally bladed disks (blisks) machined from Ti 6-2-4-6 pancake forgings. The second vane is fixed geometry and is a one piece ring machined from a 17-4PH forging.

Table 2-1. Baseline two-stage compressor design parameters.

Corrected flow, Wcor	10.53 lbm/sec	
Pressure ratio, Rc	5.0	
Adiabatic efficiency	83.2%	
Polytropic efficiency	86.5%	
Corrected speed	49,000 rpm	
Tip speed	1676 ft/sec	
Specific flow	42.5 lbm/sec-ft^2	
Inlet Rh/Rt	0.494	
Exit Rh/Rt	0.881	
Last Blade Height	0.468 in.	
	Stage 1	**Stage 2**
Rotor AR	0.733	0.803
Stator AR	0.680	0.550
Rotor solidity	1.77	1.71
Stator solidity	1.77	2.19
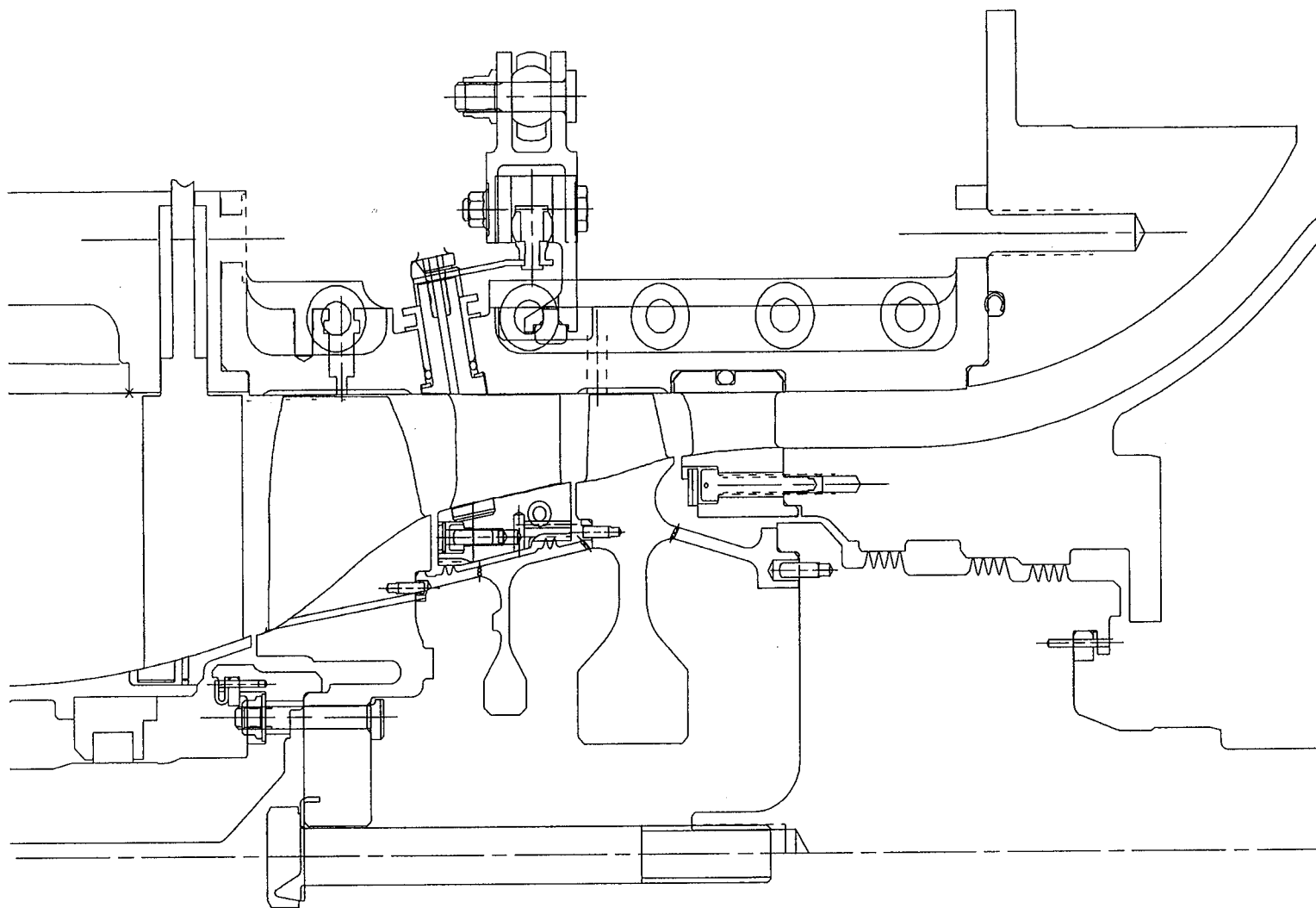
Figure 2-1. Baseline ASTC cross-section.

2.2.2 Instrumentation

The compressor was tested with a full set of aerodynamic instrumentation to ensure that adequate information was collected to fully understand the compressor aerodynamics. Total pressure and temperature rakes and static pressure taps positioned upstream in the plenum were used to determine inlet conditions. Interstage instrumentation consisted of a series of casing wall static pressure taps over the rotor blade tips and in the leading edge plane of each blade row, fast response dynamic pressure sensors over the blade tips, and total pressure and temperature probes located at the first stator leading edge. The small size of the second stator precluded the use of leading edge instrumentation, as the size of the probes could substantially affect the flowfield. Compressor discharge conditions were determined by six 5-element total pressure and temperature rakes and static pressure taps positioned in the same plane on the hub and casing. In addition, three clearance probes were positioned over each rotor to monitor blade tip clearance and to detect rotor/casing rub.

2.2.3 Two-Stage Baseline Test

The compressor was installed in the Small Compressor Test Facility at NASA Lewis Research Center (Ref 4). The schematic of this facility in Figure 2-2 shows it to have a typical compressor test facility layout with atmospheric or conditioned supply air that passes through a plenum chamber with screens to provide uniform flow into the compressor. The facility also has the ability to exhaust to atmospheric conditions or the altitude exhaust system. The installation drawing of Figure 2-3 shows this rig to have very long inlet bell that is over seven compressor diameters in length from the plenum to the compressor inlet face. Due to the concern of a large boundary layer build-up on the case wall, a boundary layer suction bleed system was installed just upstream of the IGV's. Bleed optimization tests showed that 2% bleed was required to remove the boundary layer sufficiently. The bleed could be modulated from the control room and was set at 2% of the supply air corrected to standard day for all compressor testing.

The compressor was mapped with distortion free ambient inlet conditions with the variable vanes scheduled with speed for best performance. The resulting compressor performance map is shown in Figure 2-4. The overall performance results at the design pressure ratio condition are listed in Table 2-2. The Figure 2-4 map shows the compressor had to be run at 102% design speed to achieve the design flow and pressure ratio. The efficiency at this condition was more than 2
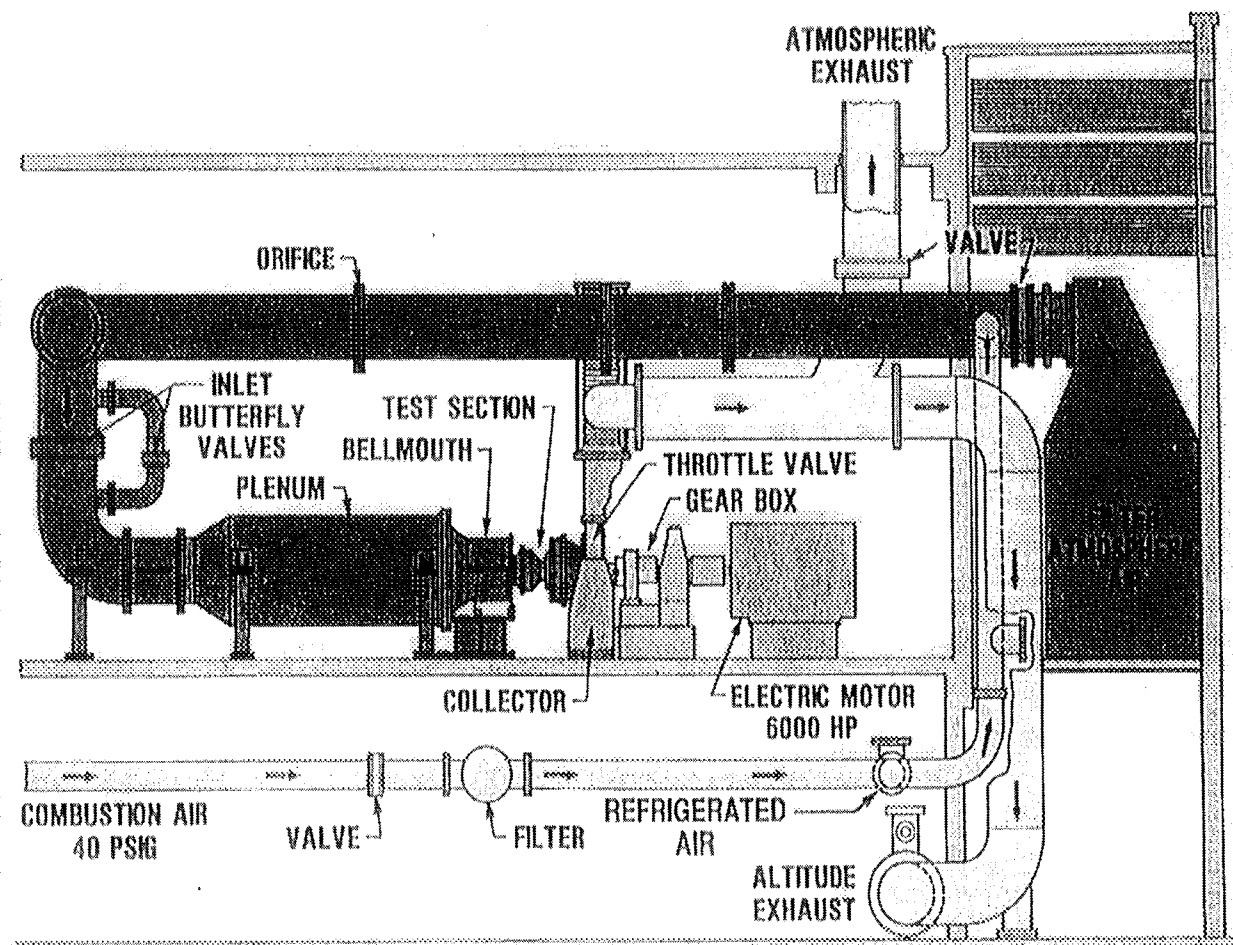
Figure 2-2. *Schematic of NASA Lewis Research Center's Small Engine Components Compressor Test Facility.*
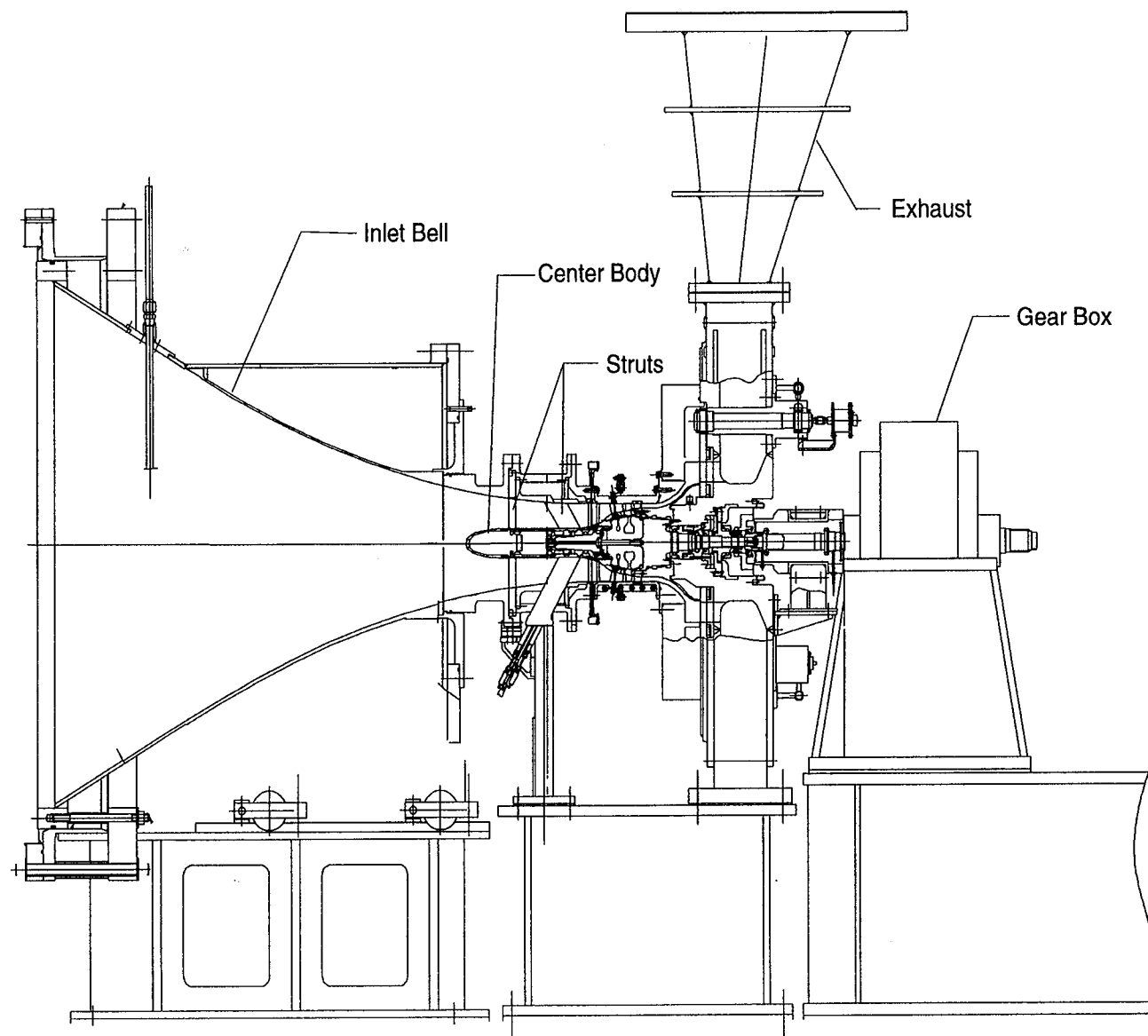
Figure 2-3. ASTC test rig installation.
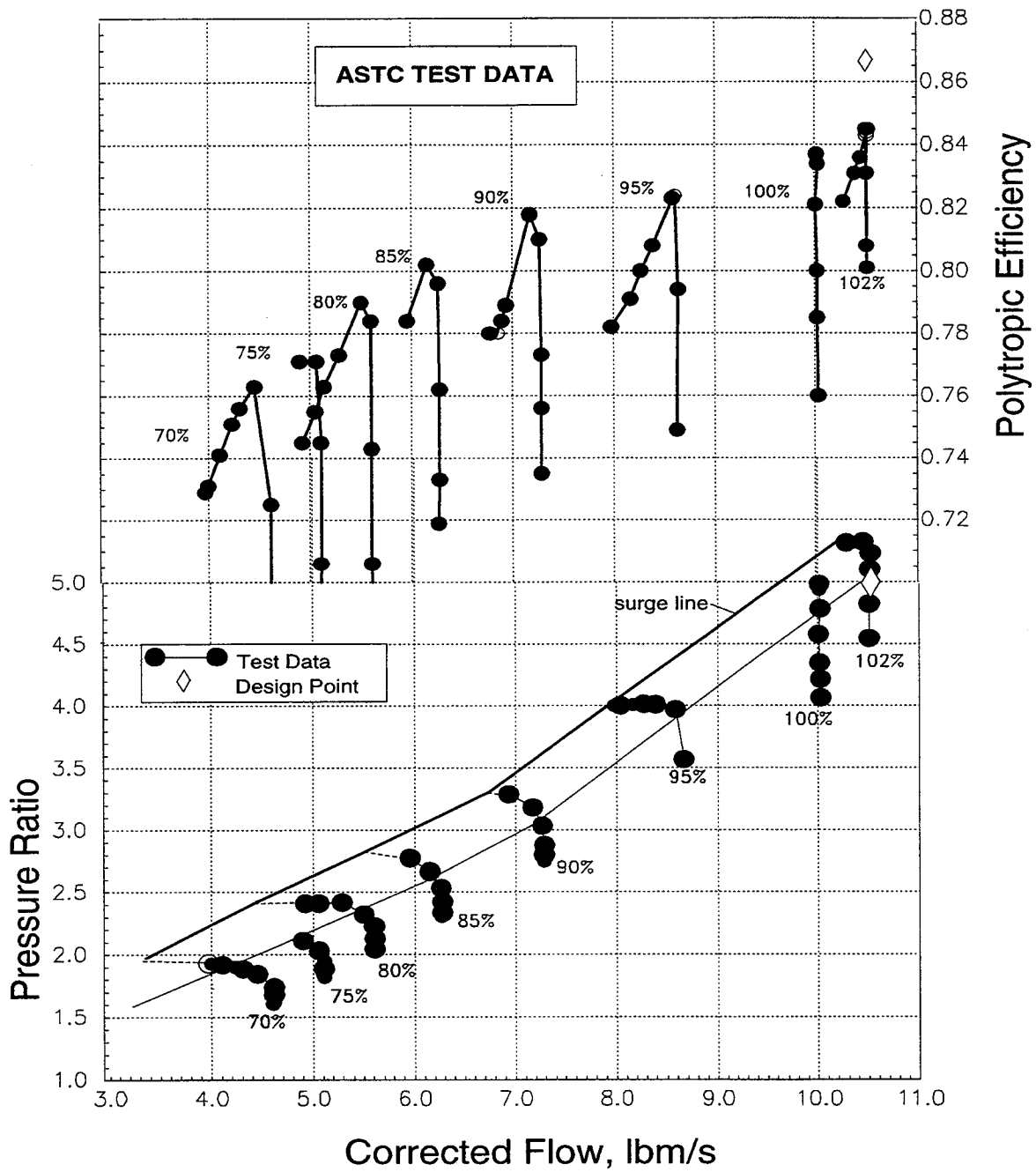
Figure 2-4. The two-stage compressor was fully mapped to 102% speed.

11

points lower than the design intent, partly due to the higher speed. The over-speed was required to get the first rotor to swallow the shock and to operate in a started condition as is evident by the large jump in flow and efficiency from 95% to 102% speed. This was also confirmed by the case mounted dynamic pressure transducers located near the leading edge. The transducer signals plotted in Figure 2-5 are for one rotor revolution and show a large decrease in shock strength between 95% and 102% speed for all 16 rotor passages. The first rotor could be made to start at 100% speed by opening the IGV 8 degrees but a substantial efficiency penalty was measured in this case. The poor starting characteristic of the first rotor was a result of the second stage back pressuring the first stage. This was indicated by the high measured first rotor pressure ratio of 2.78 or higher compared to the design value of 2.66. The source of the back pressure may be a result of the second stage having low flow capacity and/or excessive blockage produced by the first stator.

Table 2-2. Overall test performance at design pressure ratio.

	Design Pressure ratio
Corrected flow, lbm/s	10.5
Pressure ratio	5.0
Adiabatic Eff., %	80.9
polytropic Eff., %	84.8
Corrected speed, rpm	49,980
Stall margin, %	8.5

Much of the lower than goal efficiency may be attributed to effects of small size as the last blade height was less then 0.5 inches. These effects include large clearance to span ratios and large portions of the flow passage containing endwall boundary layers and secondary flows. Small size effects also include manufacturing limitations on fillet radii, blade leading edge radii and blade thickness to chord ratios. Also contributing to the low measured efficiency were losses associated with a long inlet containing two sets of struts and a long centerbody which were included in the measurements. When correcting for size and inlet loss, the compressor efficiency would be 88% which is exceptional when compared to efficiencies for other high tip speed compressors as shown in Figures 2-6 and 2-7.

12
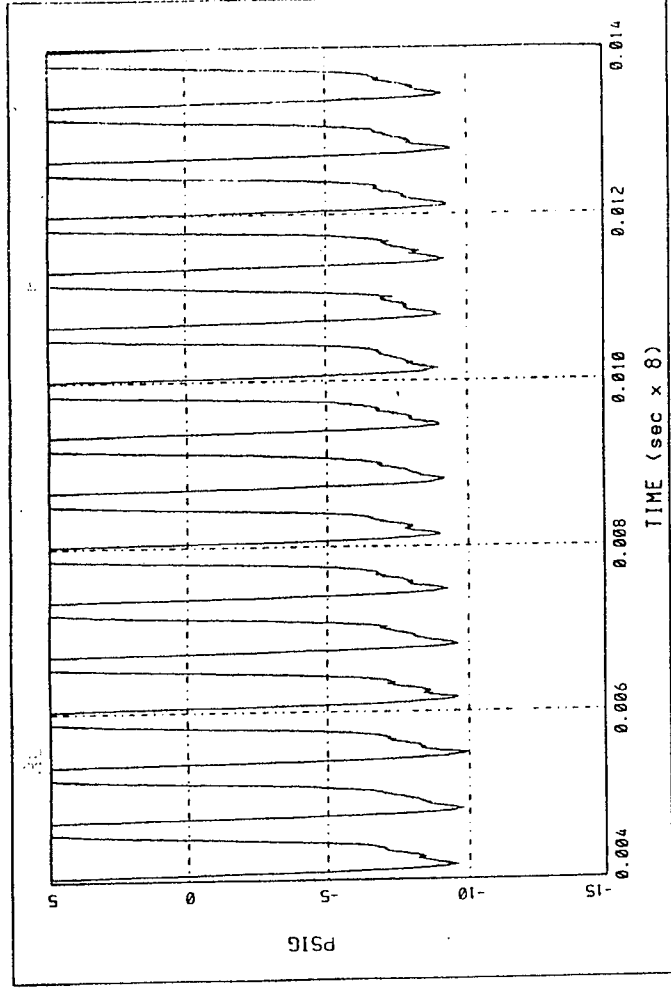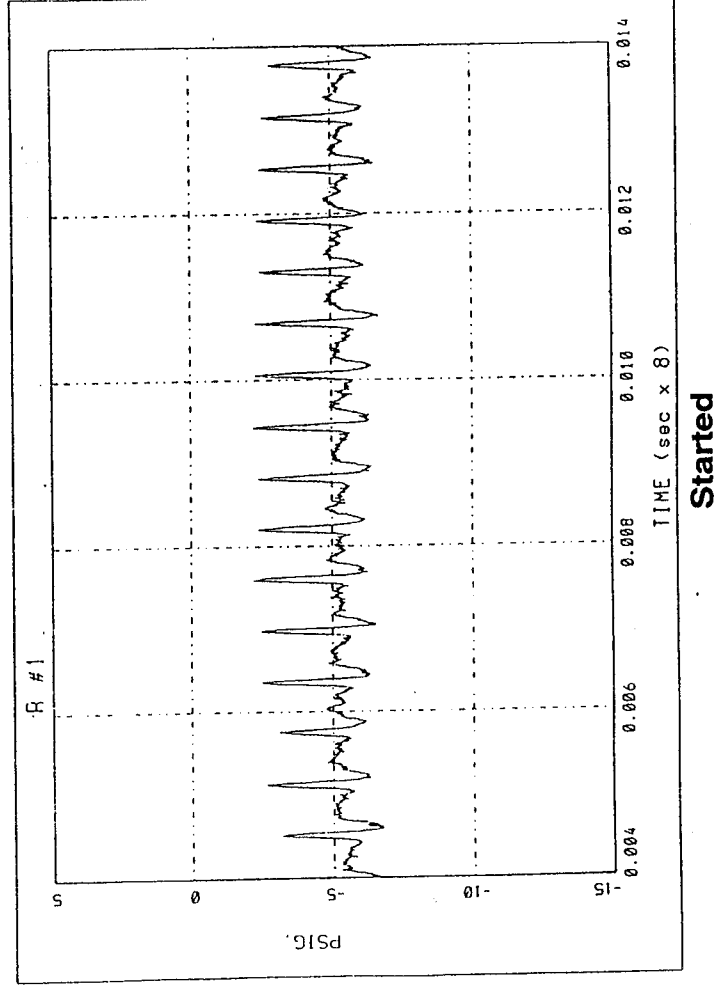
Figure 2-5. Dynamic pressure measurements indicate when first stage rotor has started.

13
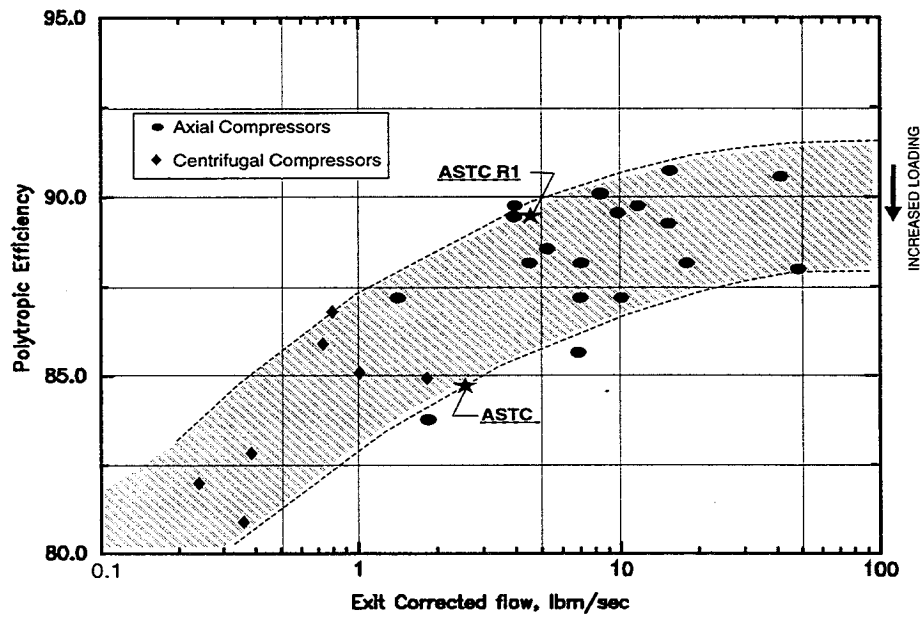
Figure 2-6. Compressor size effects on polytropic efficiency.
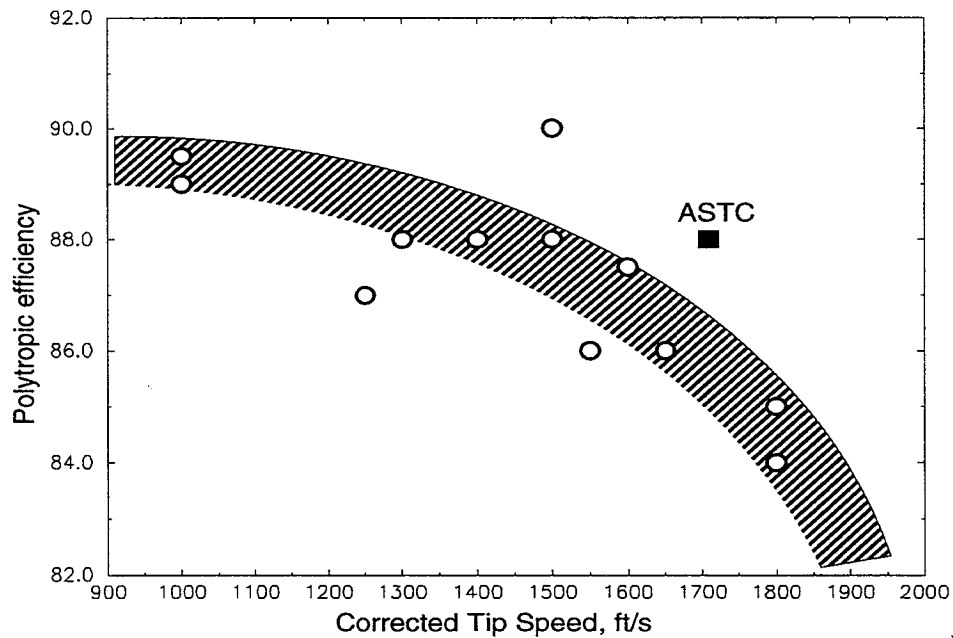
Figure 2-7. The ASTC first stage rotor had excellent efficiency compared to other high tip speed rotors.

14

2.2.4 Single Stage Baseline Test

To confirm that the poor starting characteristic of the first rotor was caused by back pressure from the second stage, the compressor rig was modified to run as a single stage compressor as shown in Figure 2-8. The inlet guide vanes were also removed from the single stage rig to allow for a forward swept rotor test described later in Chapter 4. The single stage rig was also modified to allow for a radial traversing eleven element total pressure and temperature wake rake located aft of the first vane for determining detailed stage and stator performance.
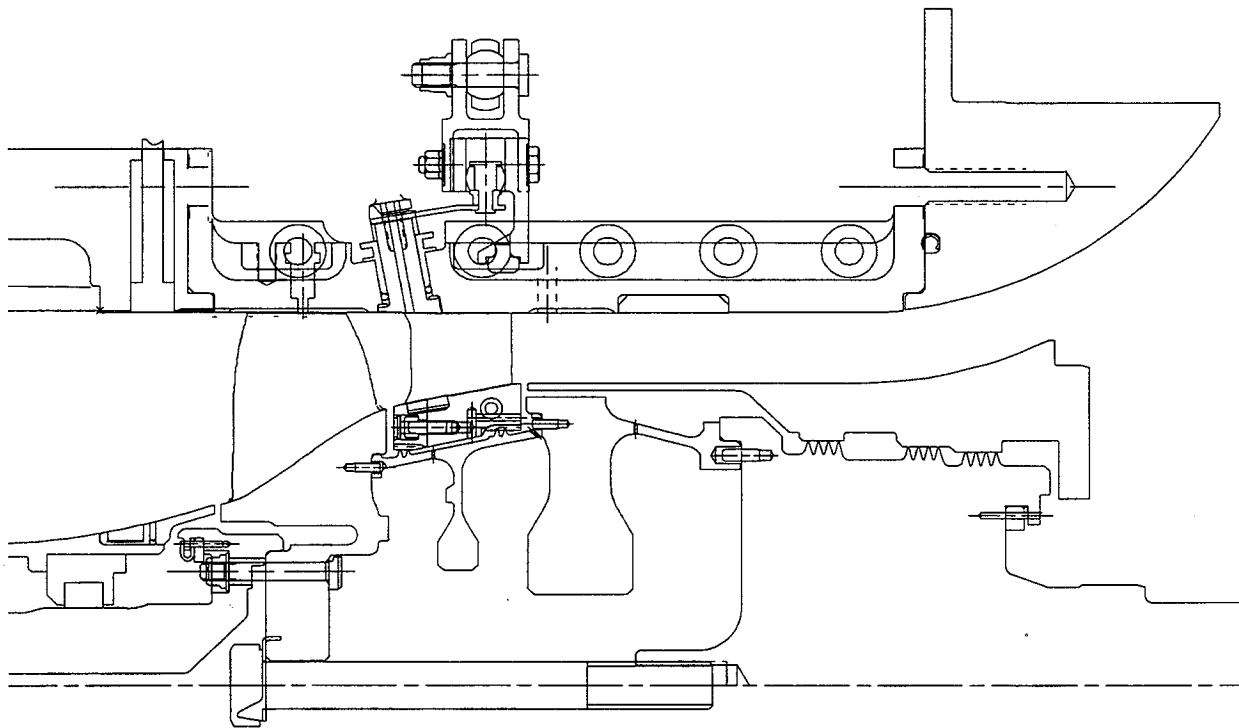
Figure 2-8. Single stage compressor rig.

The results of this test are compared with the rotor performance data from the two stage test in Table 2-3. The first rotor compressor map is shown in Figure 2-9 along with a few two stage test points with the inlet guide vane set at the nominal position. These results show that the rotor was started at 100% speed for the single stage test and even overflowed by 2%. This confirms that the second stage of the two-stage configuration was not matched properly with the first stage causing it to operate at a higher pressure ratio.

Table 2-3. First Rotor measured performance at 100% corrected speed.

	Single stage	Two stage
Corrected flow, lbm/s	10.75	10.0
Pressure ratio	2.66	2.65
Adiabatic Eff., %	87.8	84.2
polytropic Eff., %	89.3	86.2

More details of the single stage test will be provided in the comparison with the forward swept rotor results in Chapter 4.
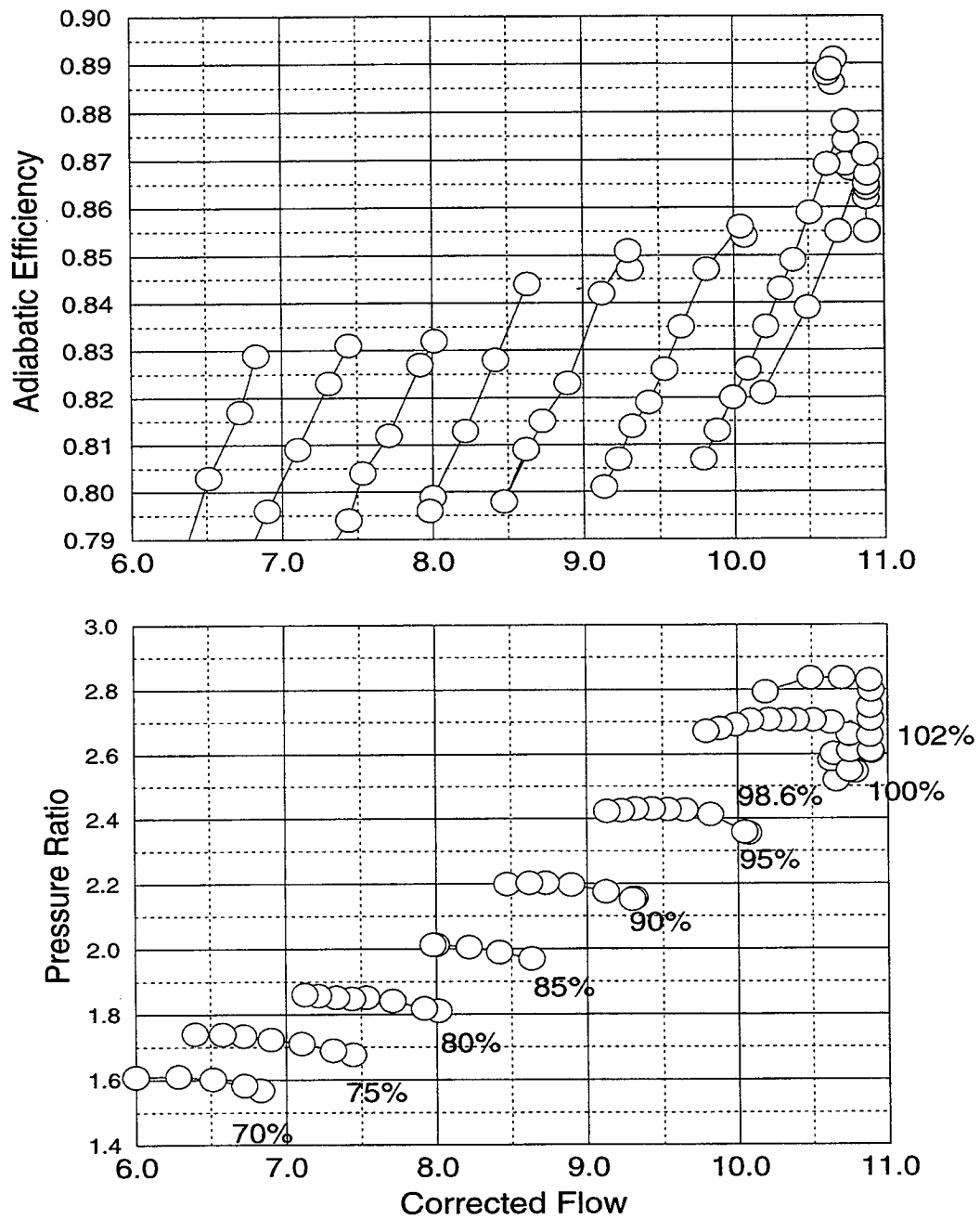
Figure 2-9. First stage rotor measured performance in single stage rig.

This Page Intentionally Left Blank

3.0 BASELINE COMPRESSOR ANALYSIS

The performance of the ASTC was predicted using the *ADPAC* multistage
Navier-Stokes code. This code was used to obtain both steady and unsteady
solutions to be compared to test data and to the results of the *APNASA* analysis
described above. The baseline compressor was also analyzed using the single
blade row OCOM3D code by 'stacking' the solutions from each blade row. Only a
few primary parameters that describe the performance of the compressor are
presented. The intent of this chapter is to compare the accuracies and
inaccuracies of three types of multistage analysis methods.

3.1 *ADPAC* MULTISTAGE ANALYSIS

The *ADPAC* code is a general purpose turbomachinery aerodynamic design
analysis tool which has undergone extensive development, testing, and
verification as described in Ref 5-8. Detailed code documentation is also available
for the *ADPAC* program in Ref 9-10. A brief description of the theoretical basis
for the *ADPAC* analysis is given below, and the interested reader is referred to
the cited references for additional details.

Briefly, the *ADPAC* analysis solves a time-dependent form of the three-
dimensional Reynolds-averaged Navier-Stokes equations using a proven time-
marching numerical formulation. Solutions may be obtained using either a
rotating cylindrical coordinate system for annular flows, or a stationary Cartesian
coordinate frame for linear cascades or other non-cylindrical geometries. The
numerical algorithm employs proven numerics based on a finite volume, explicit
multigrid Runge-Kutta time-marching solution algorithm derived from the
developmental efforts of Jameson, Adamczyk, and others. (Ref 3 and Ref 11-15).
A relatively standard implementation of the Baldwin-Lomax (Ref 16) turbulence
model is available to compute turbulent shear stresses. A turbulent wall function
formulation is also available to compute complex three-dimensional flows
economically on relatively coarse meshes. Steady state flows are obtained as the
time-independent limit of the time-marching procedure. Several steady state
convergence acceleration techniques (local time stepping, implicit residual
smoothing, and multigrid) are available to improve the overall computational
efficiency of the analysis. Nonsteady flows are captured through direct time-
accurate application of the time-marching solution procedure.

An attractive feature of the *ADPAC* code is the versatility and generality in mesh

systems upon which the analysis may be performed. The *ADPAC* code permits the use of a multiple-blocked mesh discretization which provides extreme flexibility for analyzing complex geometries. The block gridding technique enables the coupling of complex, multiple-region domains with common (non-overlapping) grid interface boundaries through specialized user-specified boundary condition procedures. Applications of the block-gridding techniques for multistage turbomachinery flows include circumferential averaging (mixing planes, Ref 17) between adjacent blade rows, or by solving the complete time-dependent rotor/stator aerodynamic interaction problem using spatial/temporal interpolation techniques. The *ADPAC* analysis has been successfully utilized to predict both the steady state and time-dependent aerodynamic interactions occurring in modern multistage compressors and turbines, and is believed to be sufficiently mature to be applicable to the multidisciplinary design optimization problem previously described (Ref 18-21).

<u>3.1.1 Steady State Analysis Results</u>

The steady state multistage *ADPAC* viscous solution was obtained for all five blade rows of the ASTC baseline compressor (IGV, rotor 1, stator 1, rotor 2 and stator 2) using a mesh similar to that used for the *APNASA* analysis and illustrated in Figure 3-1. Since *ADPAC* utilizes a mixing plane between blade rows, a separate mesh blocks were used for each row and were coupled at interblade row interface planes to construct the mesh. The individual mesh block sizes are given in Figure 3-1.

An *ADPAC* analysis was performed at standard day inlet conditions , 102% corrected speed and an exit static pressure value to give an overall pressure ratio near the design value of 5.0. An analysis by the *APNASA* code at this condition was also completed and compared to the *ADPAC* results. A comparison of the solutions for these two codes is of interest as each employs a different method of passing flowfield information between the blade rows. The *ADPAC* code uses mixing plane theory while *APNASA* uses the more complex average-passage formulation of the Navier-Stokes equations.

The overall performance predictions from these codes are compared with the two stage rig test data in Table 3-1. This table shows that there are significant differences between the solutions from these codes. Both codes overpredicted

Meridional View

Top View
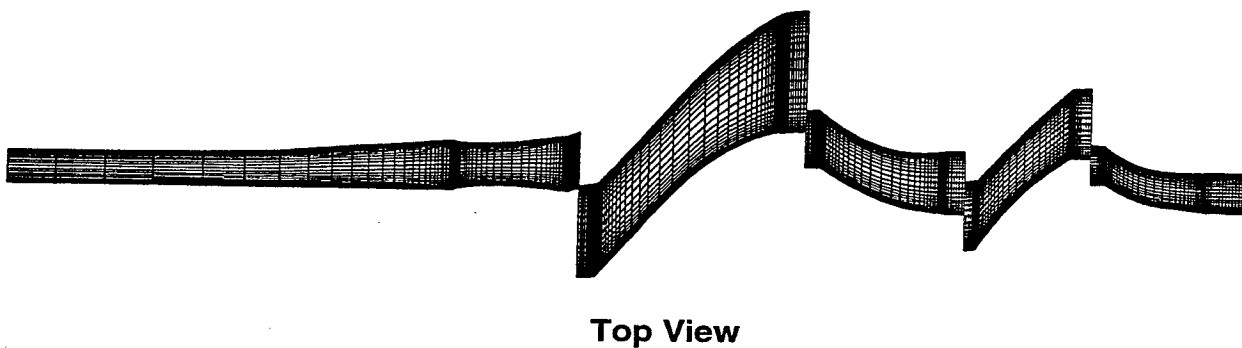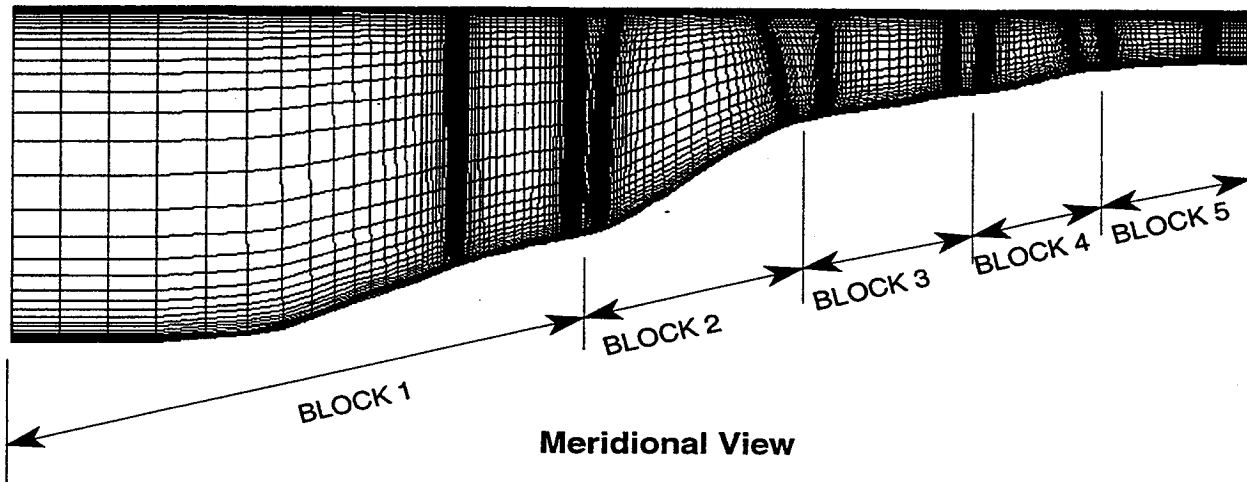
Mesh Block 1:	87x41x31 = 110,577
Mesh Block 2:	71x41x31 = 90,241
Mesh Block 3:	69x41x31 = 87,699
Mesh Block 4:	69x41x31 = 87,699
Mesh Block 5:	77x41x31 = 97,867
Total	373x41x31 = 474,083

Figure 3-1. ADPAC multistage mesh is made up of five blocks.

the mass flowrate from the measured value of 10.5 lbm/sec. The *ADPAC* flow rate prediction was 2.4% high while the *APNASA* code overpredicted the flow rate by only 1%. The measurement uncertainty for flowrate was 0.6%. Each code also predicted different adiabatic efficiencies, with *ADPAC* over predicting by 1.6% and *APNASA* under predicting by 0.9%. These inaccuracies compare to a measurement uncertainty error for efficiency of ±0.5%.

Table 3-1. Mass-average overall performance predictions from ADPAC and APNASA at 102% speed.

	Data	ADPAC	APNASA
Overall			
Wac	10.50 ±0.06	10.75	10.60
Rc	5.03 ±0.01	4.99	4.96
Efficiency	80.5 ±0.5	82.3	79.6

The stage performance data given in Table 3-2 show even further how the two analysis methods predictions differ for this compressor. Even though the overall performance predictions are similar, the intermediate values are quite different. For example, *ADPAC* predicted the first stage efficiency to be 4.7 points higher then the *APNASA* results. On the other hand, *ADPAC* predicted the second rotor efficiency to be 5.3 points lower then *APNASA*. Similar differences occur for the stage pressure ratios with APNASA predicting higher rotor pressure ratios then *ADPAC* but also higher stator total pressure loss to arrive at the same overall pressure ratio. A graphical representation comparing the cumulative pressure ratio and adiabatic efficiency differences through the compressor is provided in Figure 3-2.
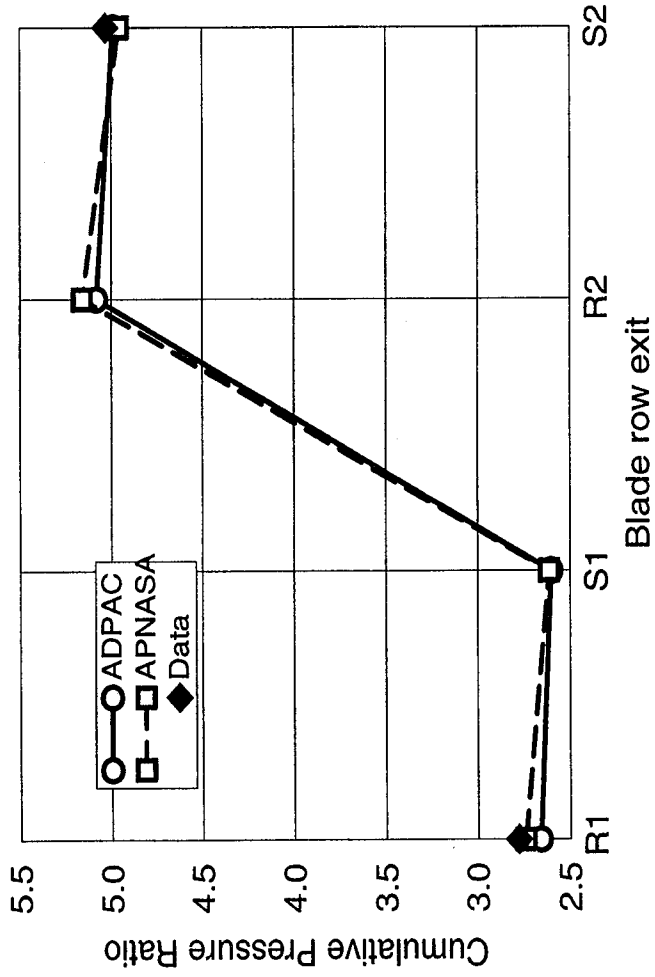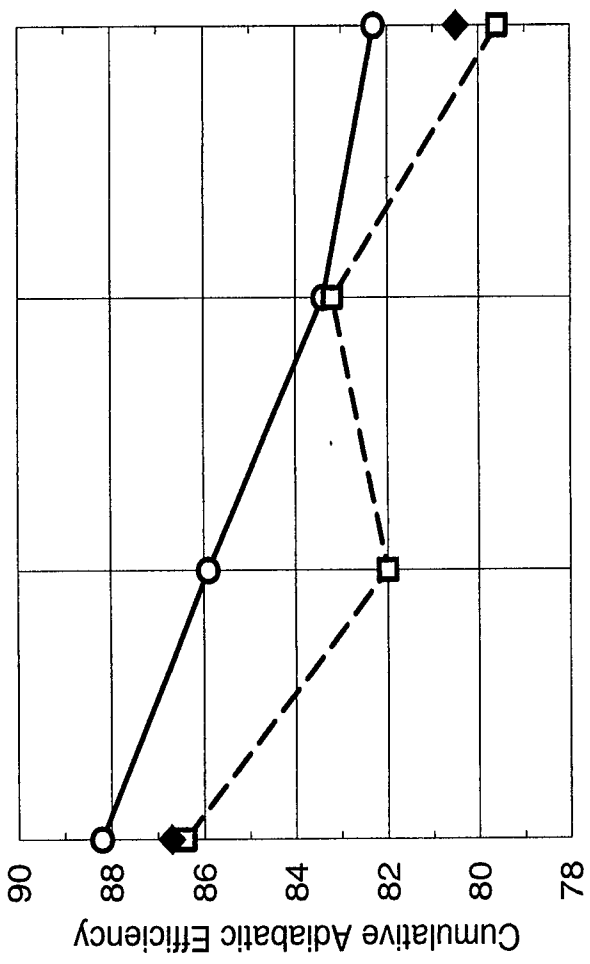
Figure 3-2. Predicted stagewise cumulative pressure ratio and efficiency compared to test data.

23

Table 3-2. Mass-average stage performance predictions from ADPAC and APNASA at 102% speed.

	Data		ADPAC		APNASA	
	Rc	Eff.	Rc	Eff.	Rc	Eff.
Stage						
IGV			0.977	-----	0.982	-----
Rotor 1	2.82 ±0.06	88.2 ±0.8	2.73	90.6	2.79	88.0
Stage 1			2.67	88.3	2.66	83.6
Rotor 2			1.96	83.6	1.98	88.9
Stage 2			1.92	81.2	1.90	80.9
Cumulative						
IGV			0.977	------	0.982	-----
Rotor 1	2.78 ±0.06	86.7 ±0.8	2.66	88.2	2.74	86.4
Stage 1			2.60	85.9	2.61	82.0
Rotor 2			5.08	83.4	5.16	83.2
Stage 2	5.03 ±0.01	80.5 ±0.5	4.99	82.3	4.96	79.6

The spanwise plots of pitchwise mass-averaged cumulative pressure ratio in Figure 3-3 show more details on where the analysis methods differ. The *APNASA* code correctly predicted the high hub pressure ratio of the first rotor, however both codes under-predicted the pressure ratio near the tip. Through the rest of the machine, it is evident that each code gives similar profile shapes with differences occurring near the endwall regions. The average level of pressure ratio differs between the codes with *ADPAC* having a lower level out of the rotors and a higher level out of the stators. This is caused by *APNASA* predicting higher rotor pressure ratios as shown in Figure 3-4 and higher stator total pressure loss as shown in Figure 3-5. Even though the codes predict very different stage pressure ratios, the overall pressure ratio profiles at the exit of the compressor are similar as a result of specifying a back pressure to obtain a pressure ratio of 5.0. The exit pressure ratio profiles agree well with the test data plotted in Figure 3-3 and are off mainly in the level of pressure ratio. The same overall average pressure ratio could be achieved by raising the specified value of exit static pressure for each analysis. Instead of re-running each solution, the exit total pressures have been normalized by their respective mass average values and plotted in Figure 3-6. This figure shows how similar the overall pressure profiles are for both methods and how well they compare to measured values.
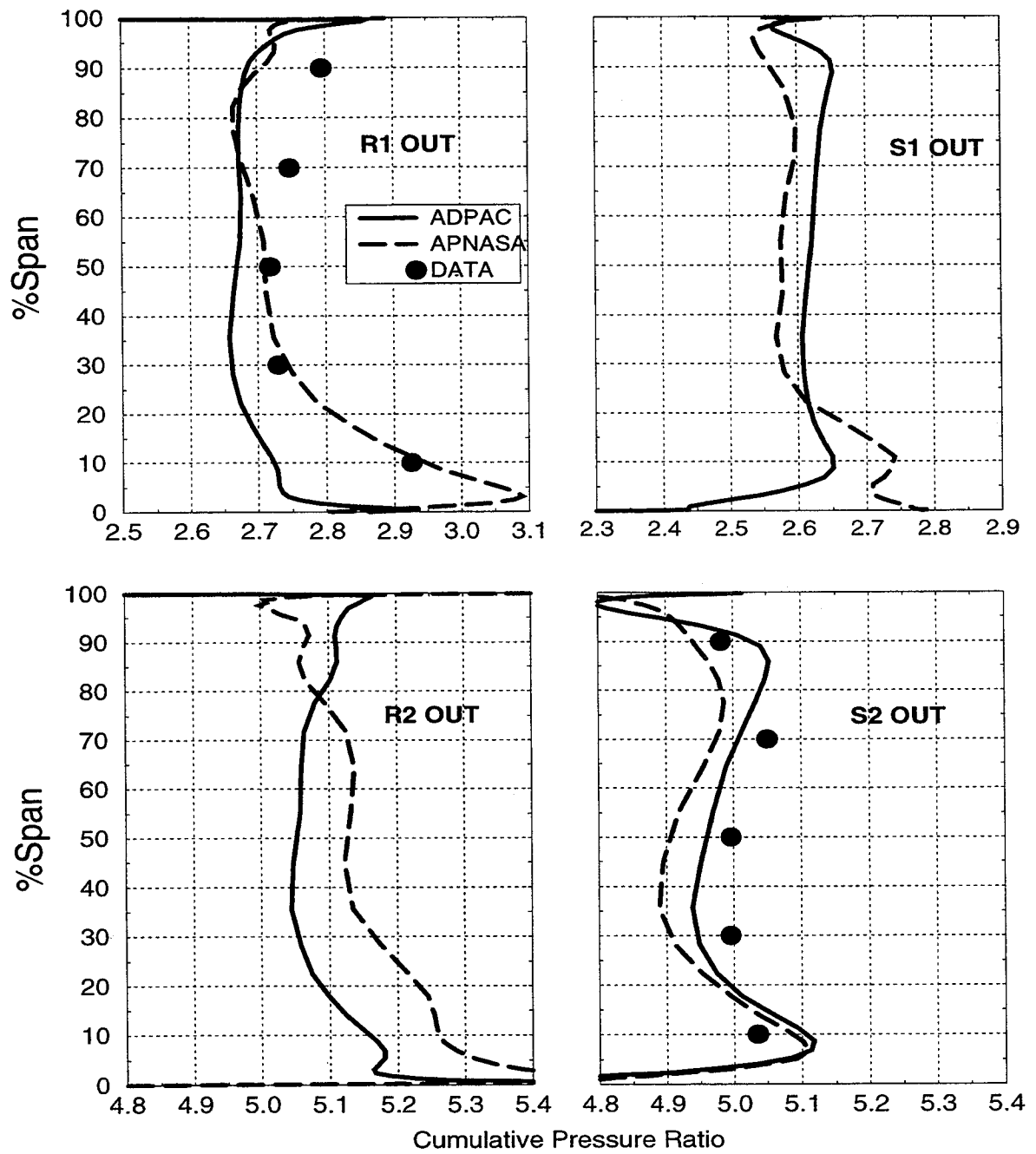
*Figure 3-3. Spanwise profiles of predicted cumulative pressure ratio
compared to test data.*
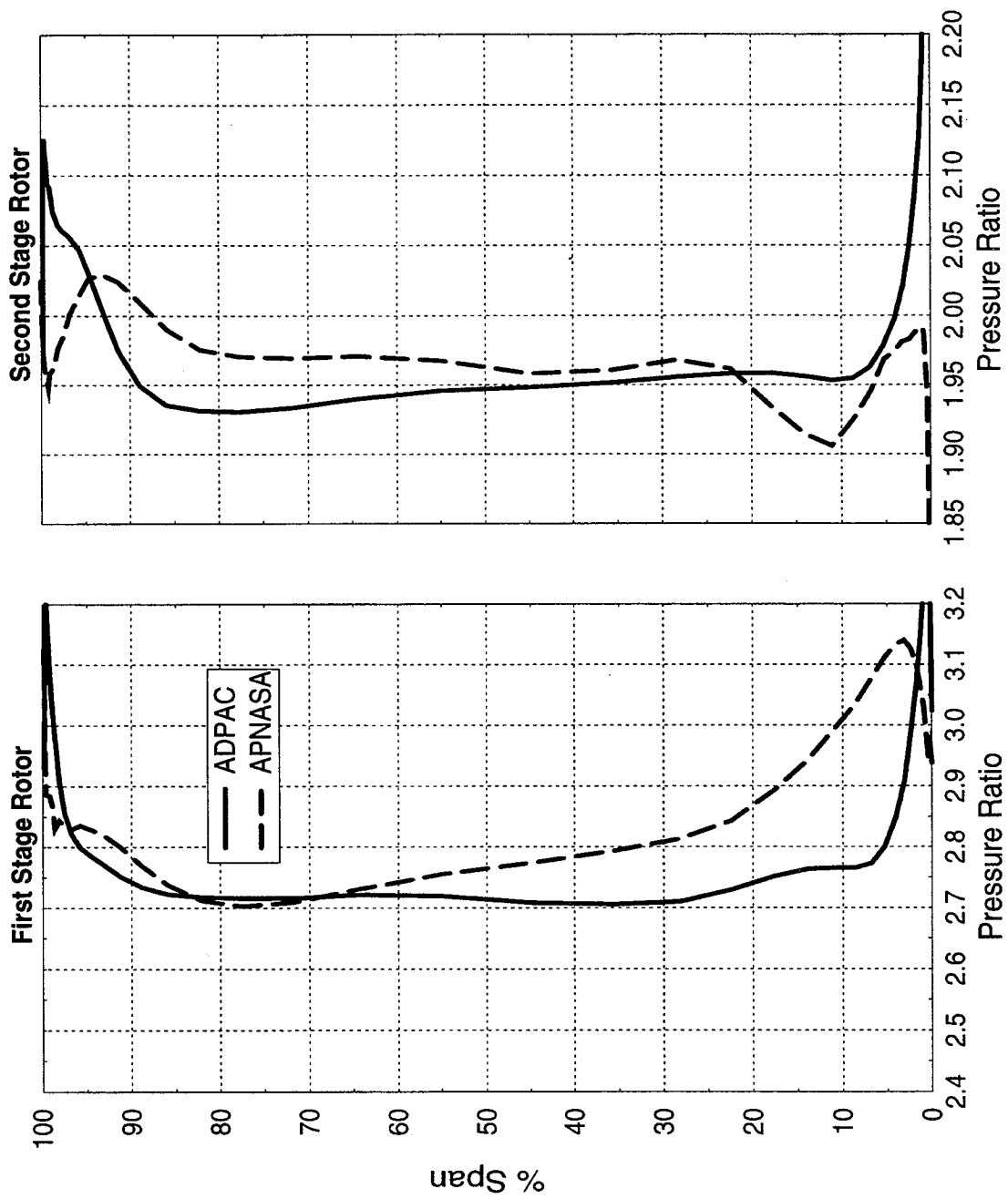
Figure 3-4. Predicted rotor pressure ratio profiles.
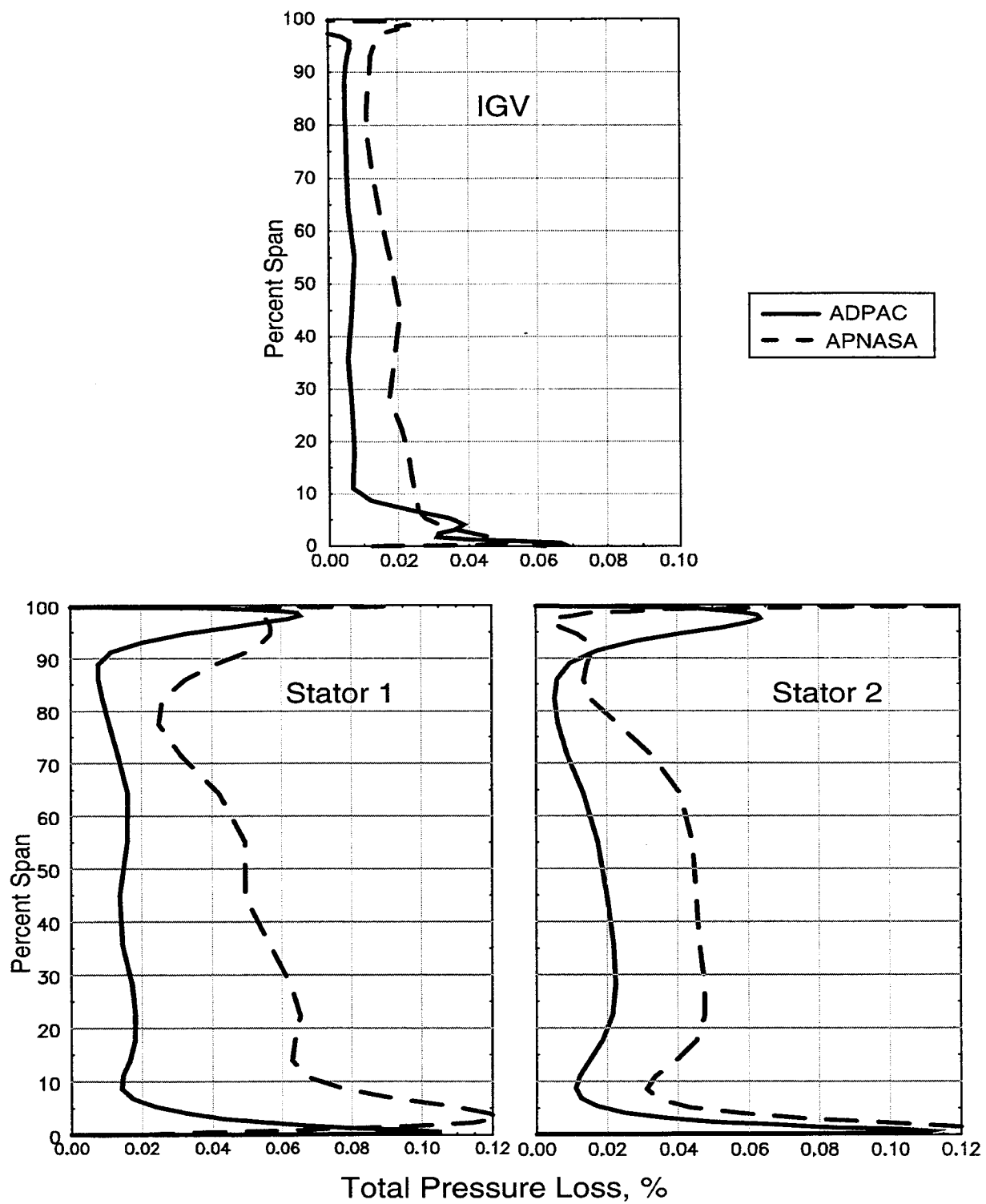
Figure 3-5. Predicted stator total pressure loss profiles.
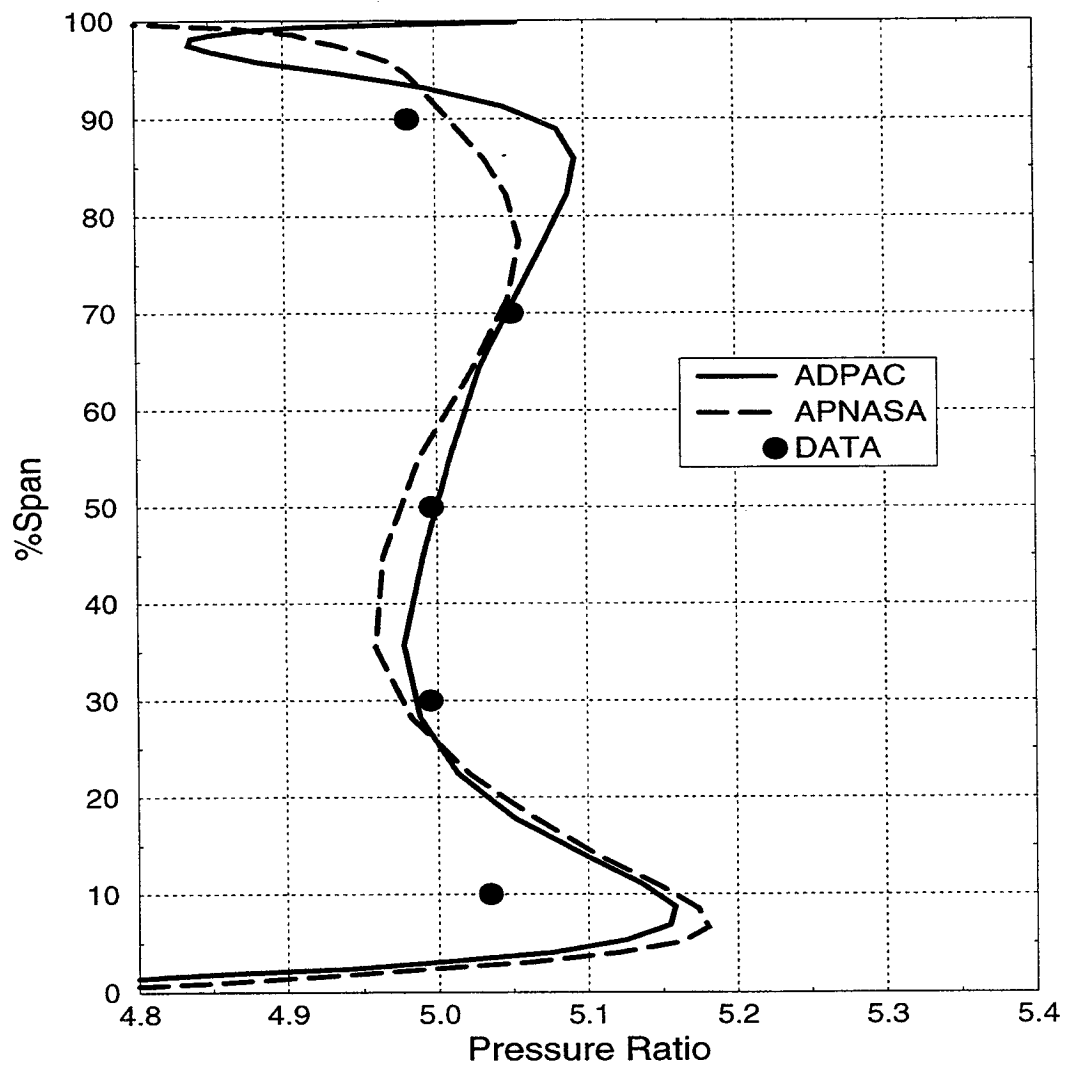
Figure 3-6. Predicted exit pressure ratio scaled to measured average value.

The spanwise profiles of circumferential mass-averaged cumulative adiabatic efficiency are compared in Figure 3-7. From this figure it can be seen that the *APNASA* model provides better agreement with the measured values at both rotor one exit and compressor exit. The predicted efficiencies for the first rotor is similar for each code except near the tip where the *APNASA* code predicts the higher loss consistent with the test data. It is also evident from this figure that higher loss in the first stator is predicted by *APNASA*. However, the efficiencies are roughly equal out of rotor 2 due to the lower rotor efficiency predicted by *ADPAC* as shown in Figure 3-8. The stator 2 exit cumulative efficiency presented in Figure 3-7 shows higher efficiency predicted by *ADPAC* over most of the span.

The predicted rotor inlet and exit relative flow angles are plotted in Figures 3-9 and 3-10, respectively. These figures show that both rotors are operating at 1 to 2 degrees higher incidence angles and lower deviation angles in the *APNASA* simulation. This is consistent with the lower flow and higher rotor work predicted by this model. The stator inlet flow angles of Figure 3-11 show the *APNASA* model to be operating with 2 to 4 degrees higher incidence for most of the span and as much as 8 degrees higher near the tip for both vanes. The stator exit flow angles shown in Figure 3-12 show the *ADPAC* code to predict lower exit swirl over much of the span, while APNASA predicts lower swirl near the tip for both vanes.

The final comparison to be made is with the case static pressures. The test rig was instrumented with static pressure taps located between each blade row and several over each rotor to fully describe the static pressure rise through the compressor. The tip circumferential mass averaged static pressures from both solutions are compared to the test data in Figure 3-13. This figure shows good agreement with the data for both models with APNASA doing a better job at predicting the location of the shock in rotor 2.
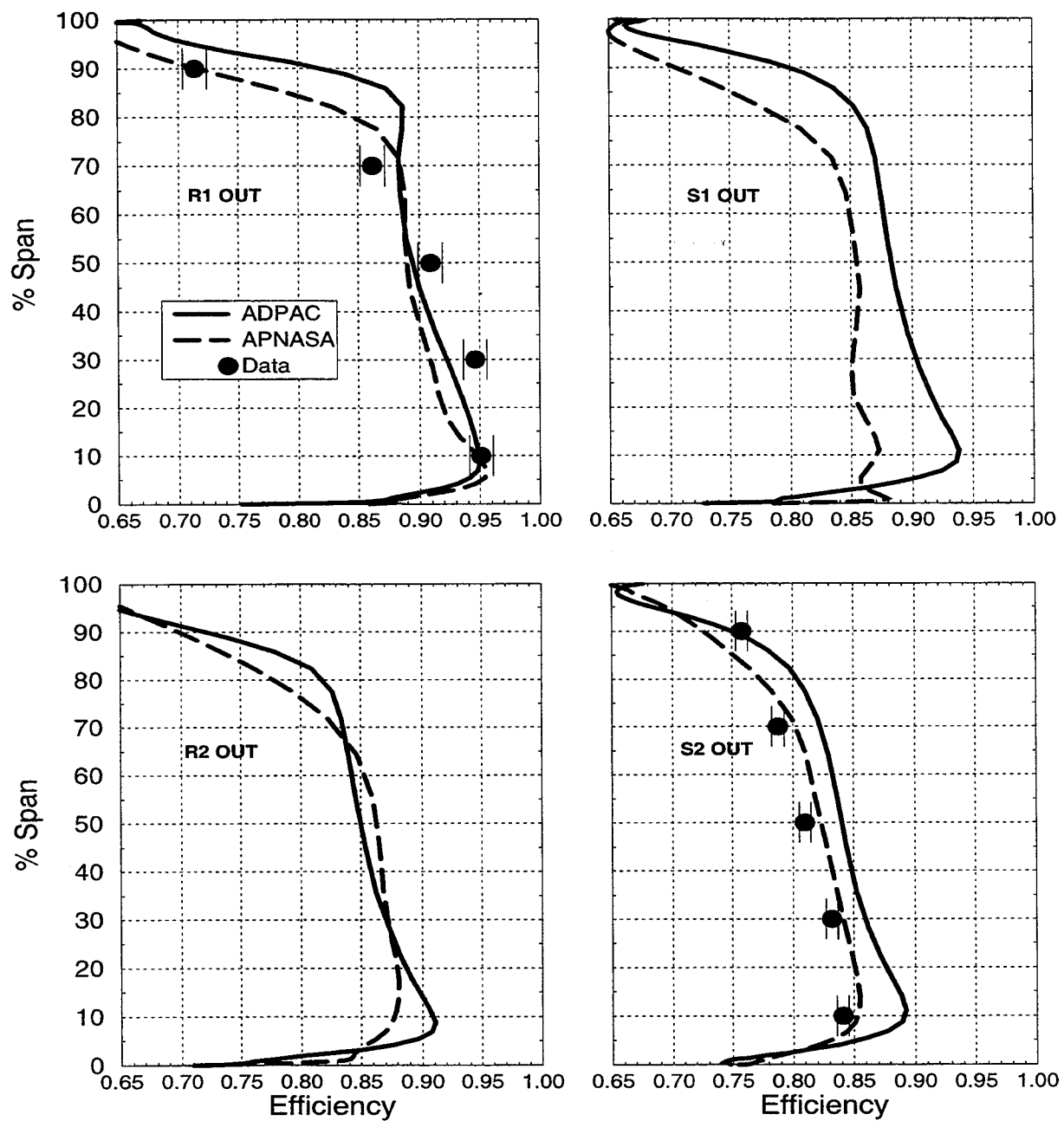
Figure 3-7. Spanwise profiles of predicted cumulative adiabatic efficiency.
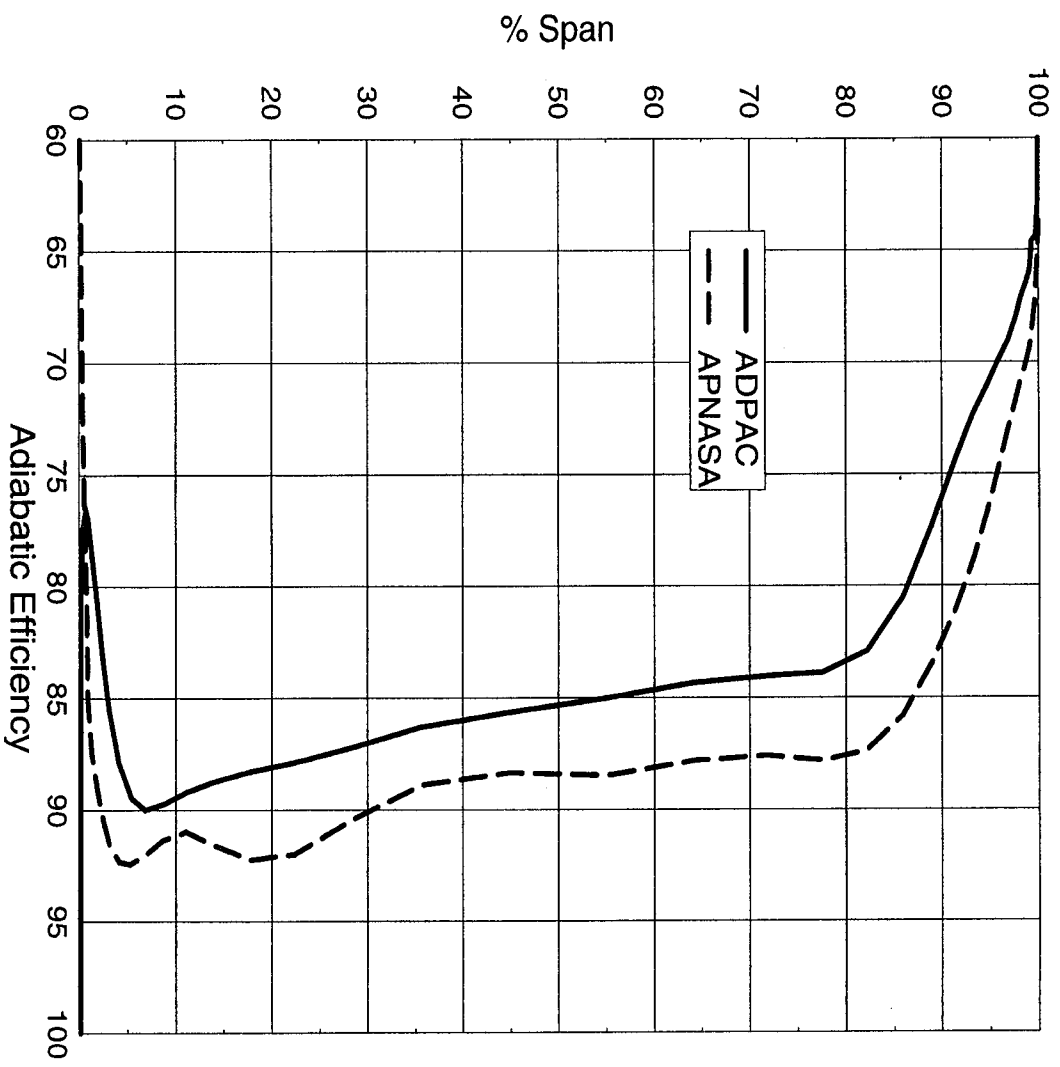
Figure 3-8. Predicted rotor 2 adiabatic efficiency profile.

31
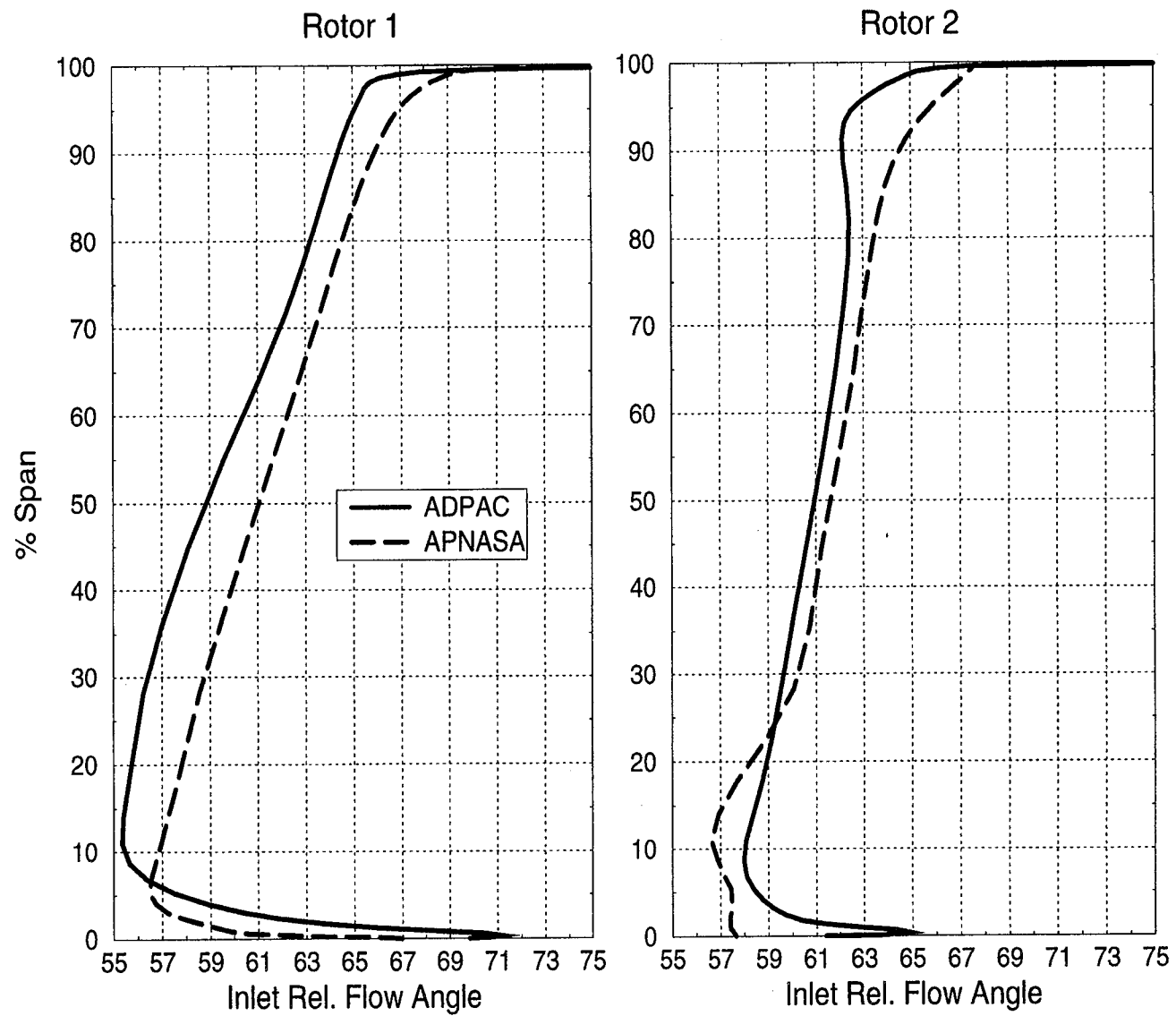
Figure 3-9. Predicted rotor inlet relative flow angle profiles.
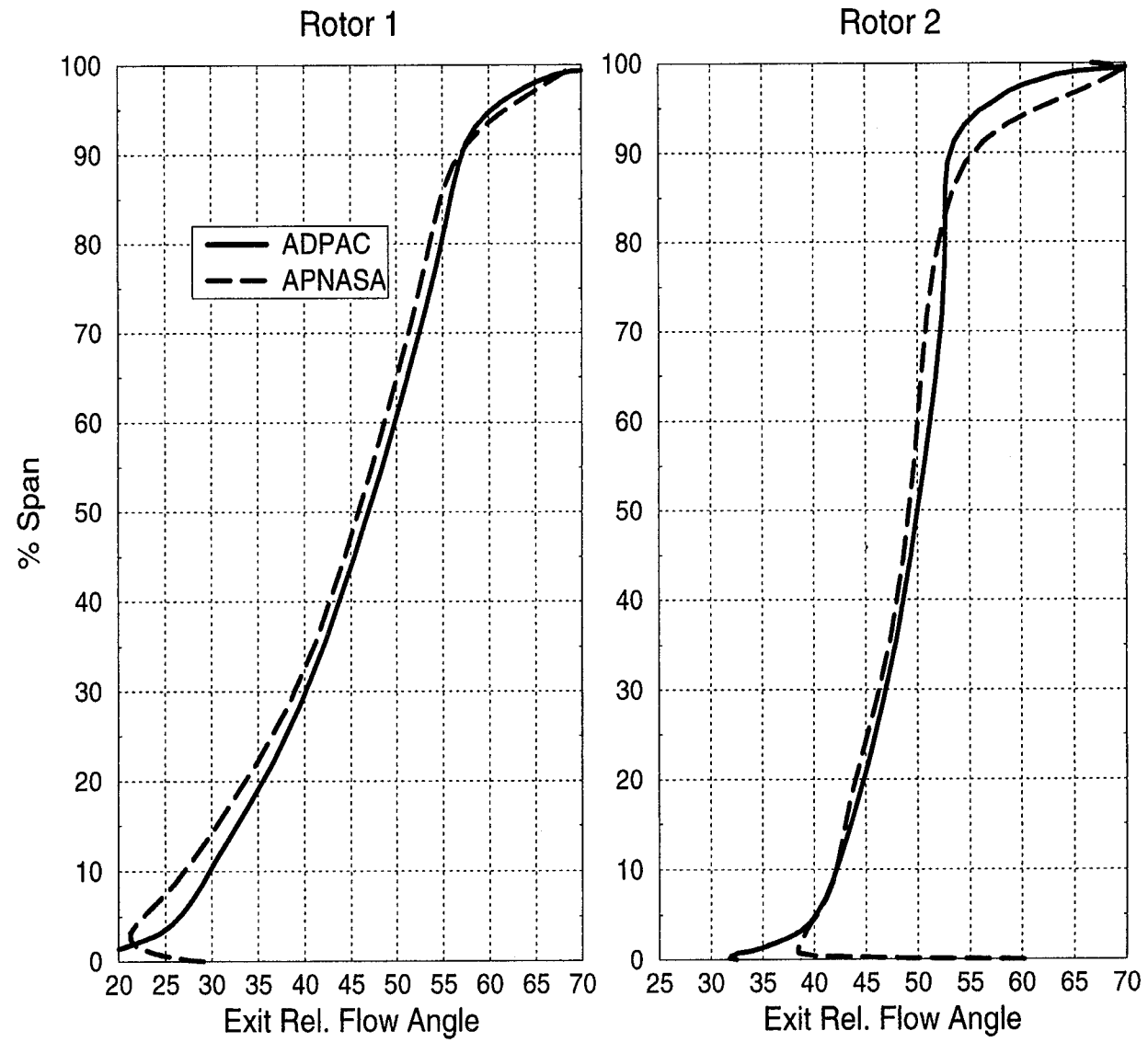
Figure 3-10. Predicted rotor exit relative flow angle profiles.
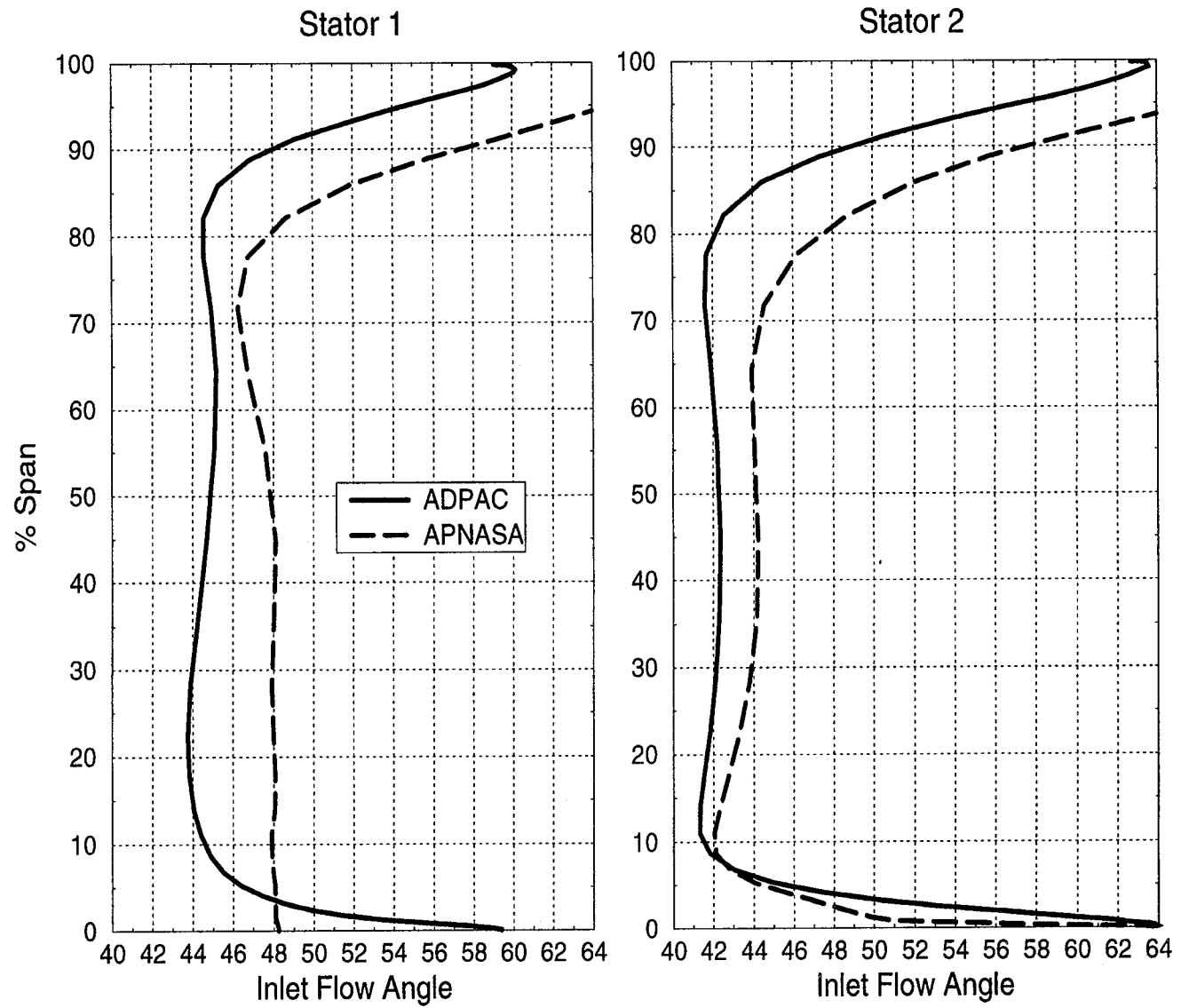
Figure 3-11. Predicted stator inlet absolute flow angle profiles.
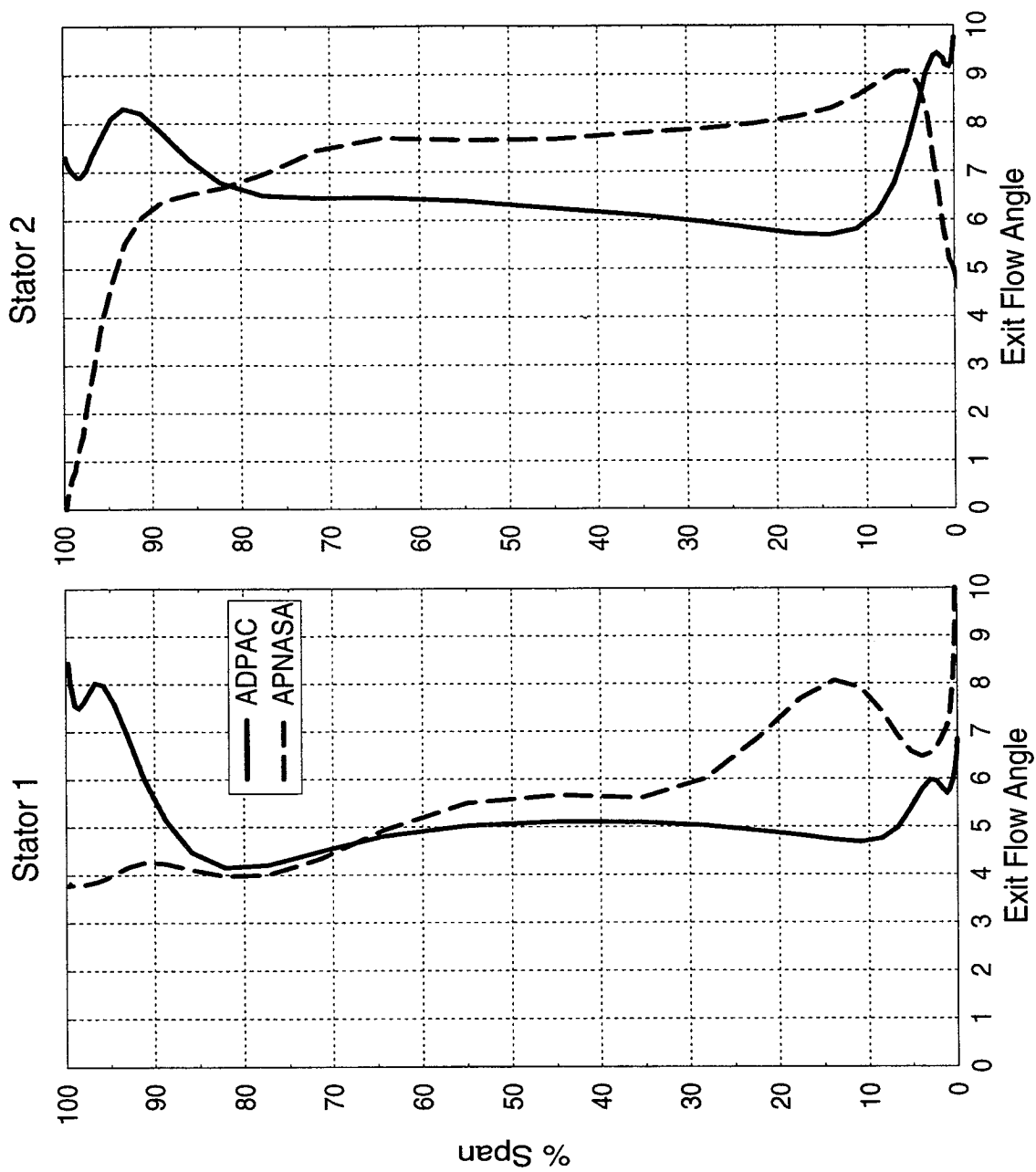
Figure 3-12. Predicted stator exit absolute flow angle profiles.

35
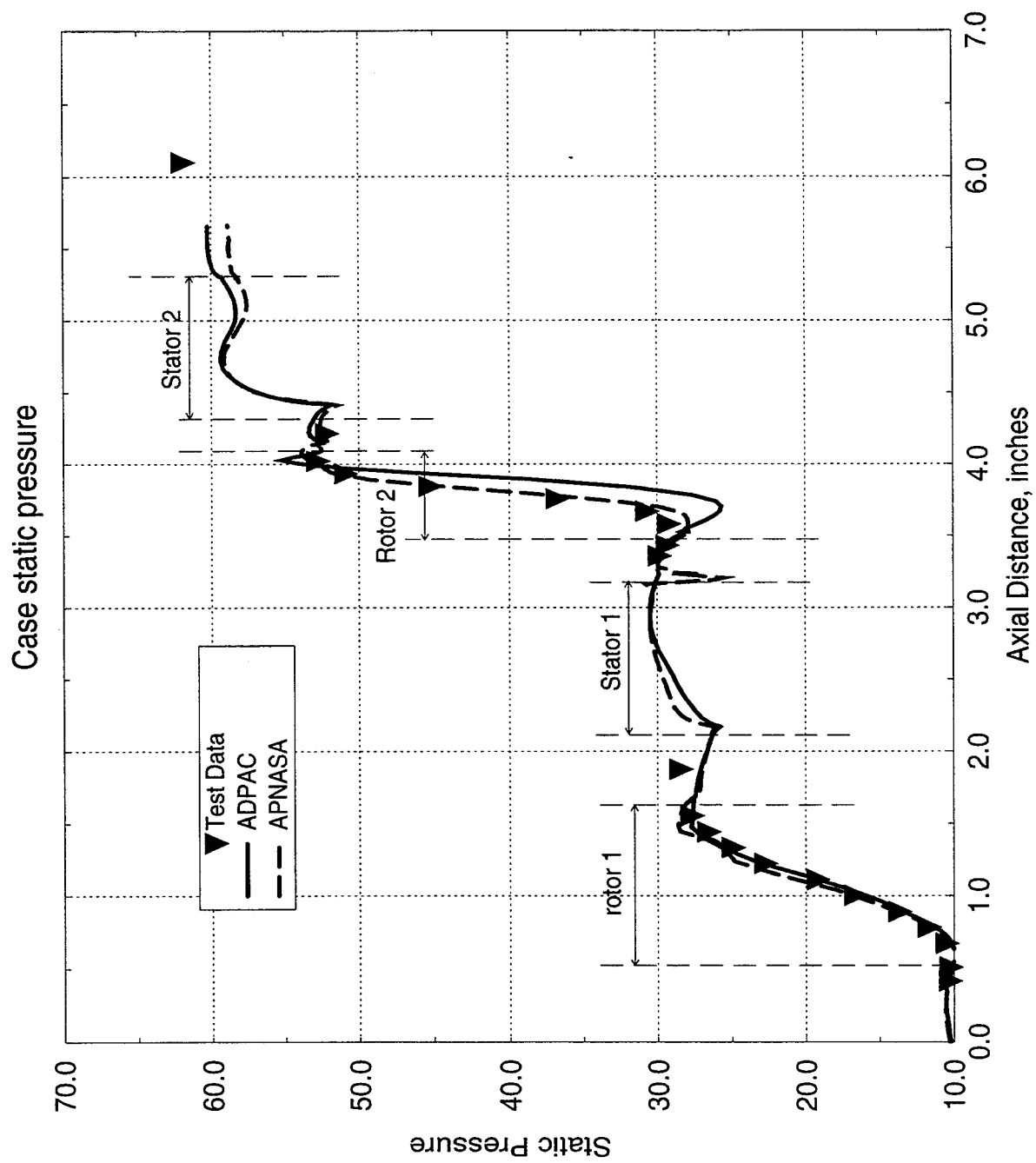
Figure 3-13. *Predicted case static pressure distribution compared to test data.*

3.1.2 Unsteady Analysis Results

The unsteady aerodynamics of the ASTC were analyzed by the *ADPAC* code at 100% speed. To simplify the analysis, the time-dependent solution was performed without inlet guide vanes and the second stage rotor count was reduced from 33 to 32. This slight blade count modification was made to permit a time-dependent analysis using a reduced domain consisting of 4, 9, 8, and 15 blade passages per blade row equaling a 90 degree sector of the compressor. The resulting computational mesh consisted of 36 blocks with a total of 1.8 million grid points and is presented in Figure 3-14. The time-dependent analysis was first initiated on a course mesh (half the grid points) before using this finer mesh. The solution was advanced over 20 thousand time-steps equalling approximately 2 revolutions requiring over 700 Cray C90 equivalent CPU hours before it was halted for data analysis.

Examination of the solution showed that the inlet flow was 10.6 lbm/sec and the outlet flow was 9.8 lbm/sec indicating the solution had not converged. Due to the large amount of CPU time that would be required to obtain convergence, it was determined not to advance the solution further. Since the solution was not fully converged only a few results are presented to provide an indication of the amount of unsteadiness occurring in the ASTC compressor and show the need to consider unsteady effects during the design.

The unsteadiness of the flowfield is evident in the instantaneous plot of entropy contours at 50% span in Figure 3-15. This figure shows the rotor wakes convecting through the downstream stator rows. The first stator wakes are not evident between second rotor airfoils due to the sparse mesh in that location as seen in Figure 3-14. The radial profiles of pressure ratio and efficiency fluctuations out of the first stage stator and compressor exit are compared to the steady-state *ADPAC* solution and test data in Figures 3-16 and 3-17, respectively. These figures show the time-dependent solution is significantly different from the steady-state analysis and has characteristics that more closely resemble the test data. It is unknown at this time if the time-dependent solution would continue to approach the experimental results if it were allowed to run to convergence.
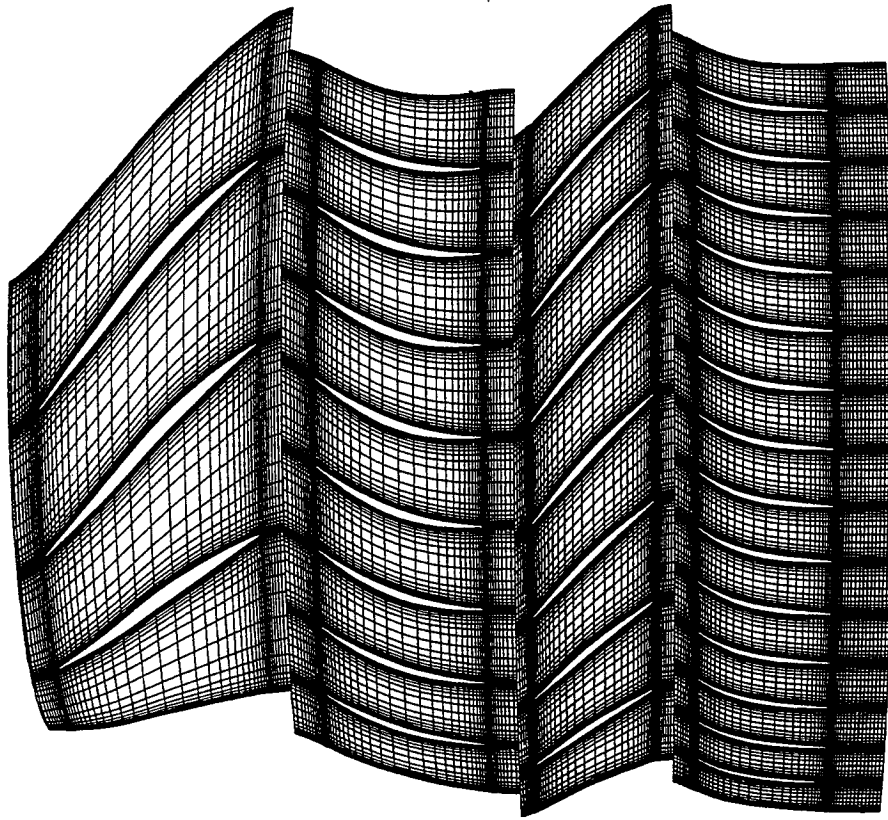
Figure 3-14. Section of ADPAC meshed used for multistage unsteady analysis.
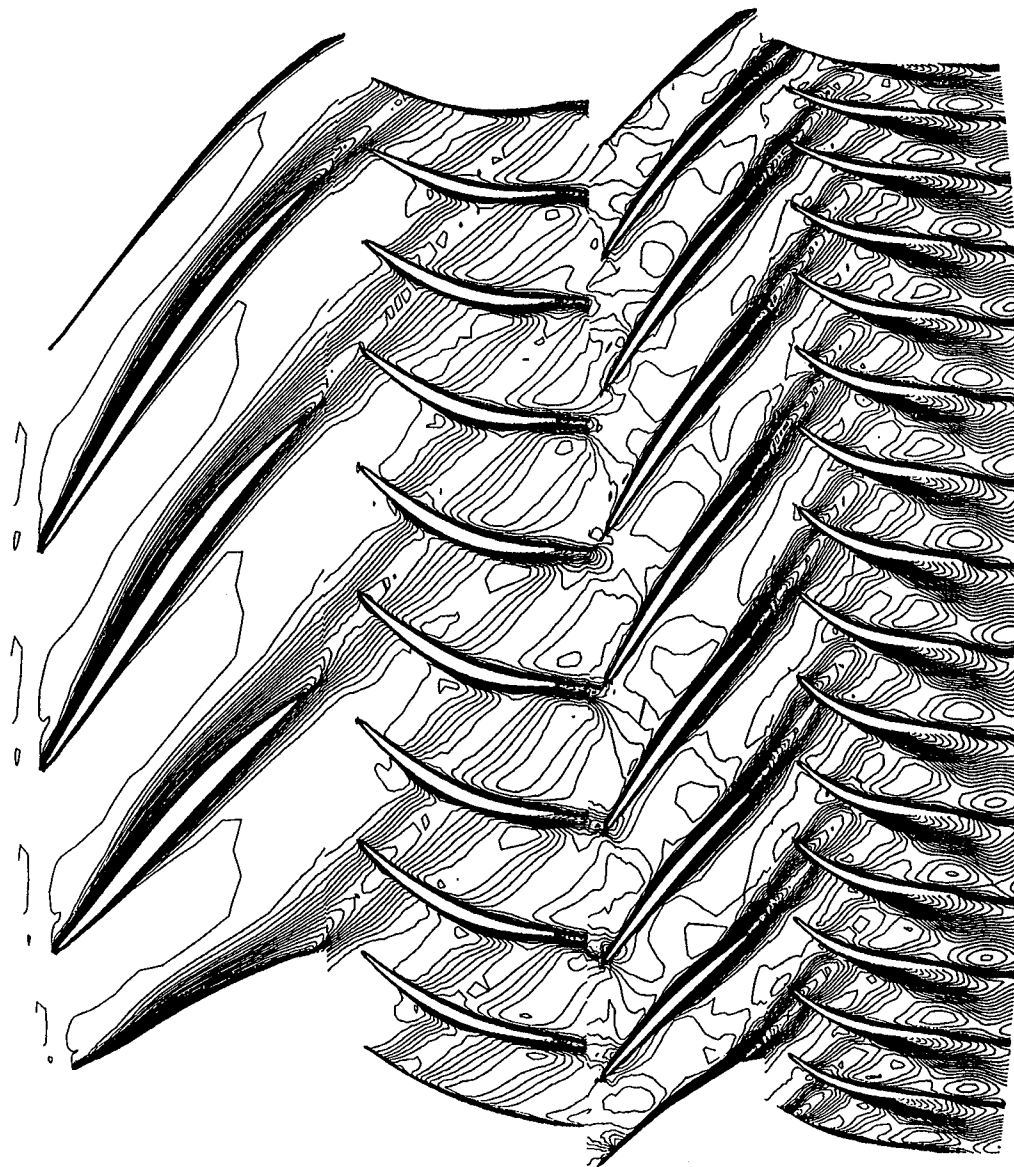
Figure 3-15. *Instantaneous plot of predicted entropy contours*
from ADPAC unsteady analysis.
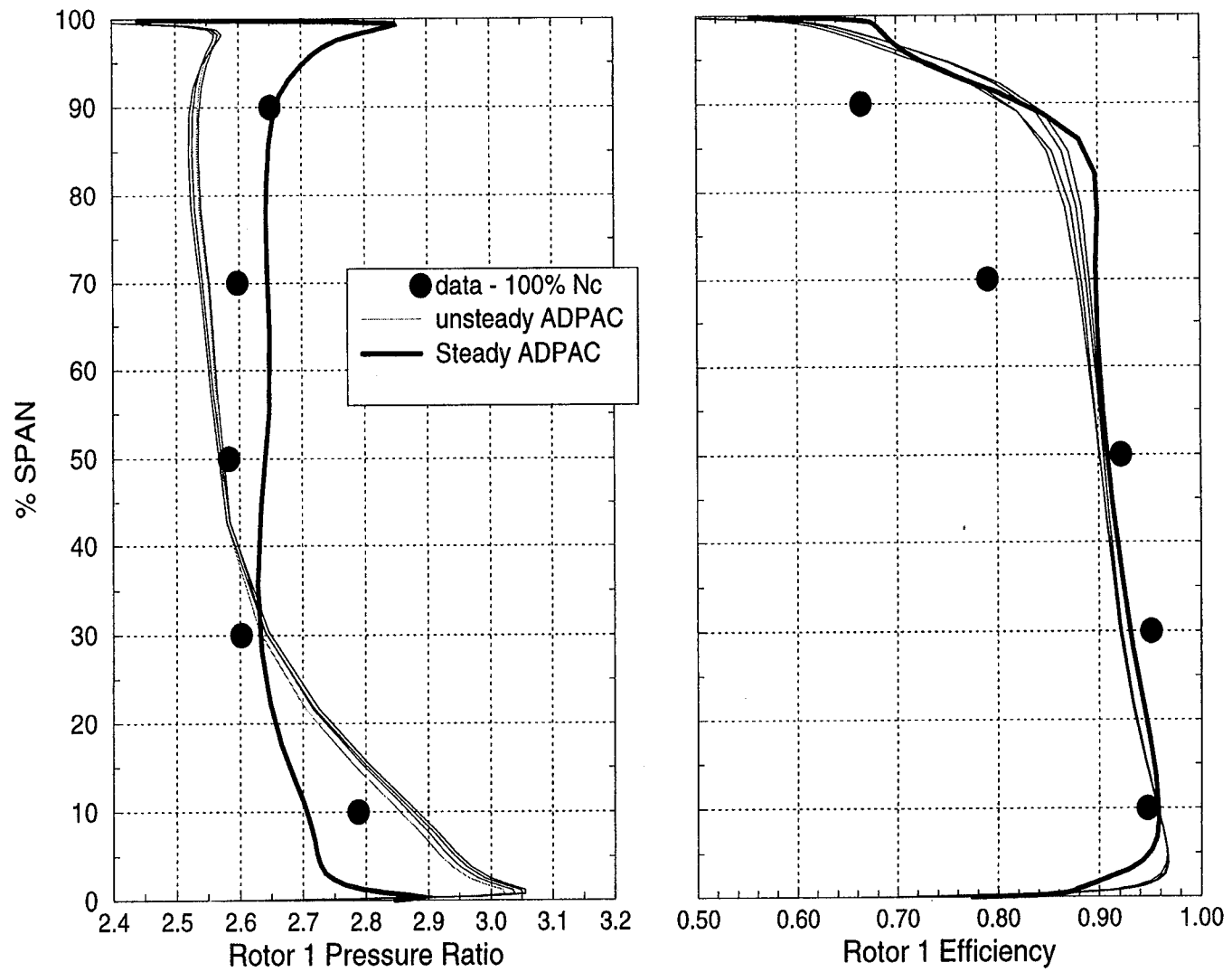
Figure 3-16. ADPAC predicted unsteady envelope of rotor 1 pressure ratio and efficiency.
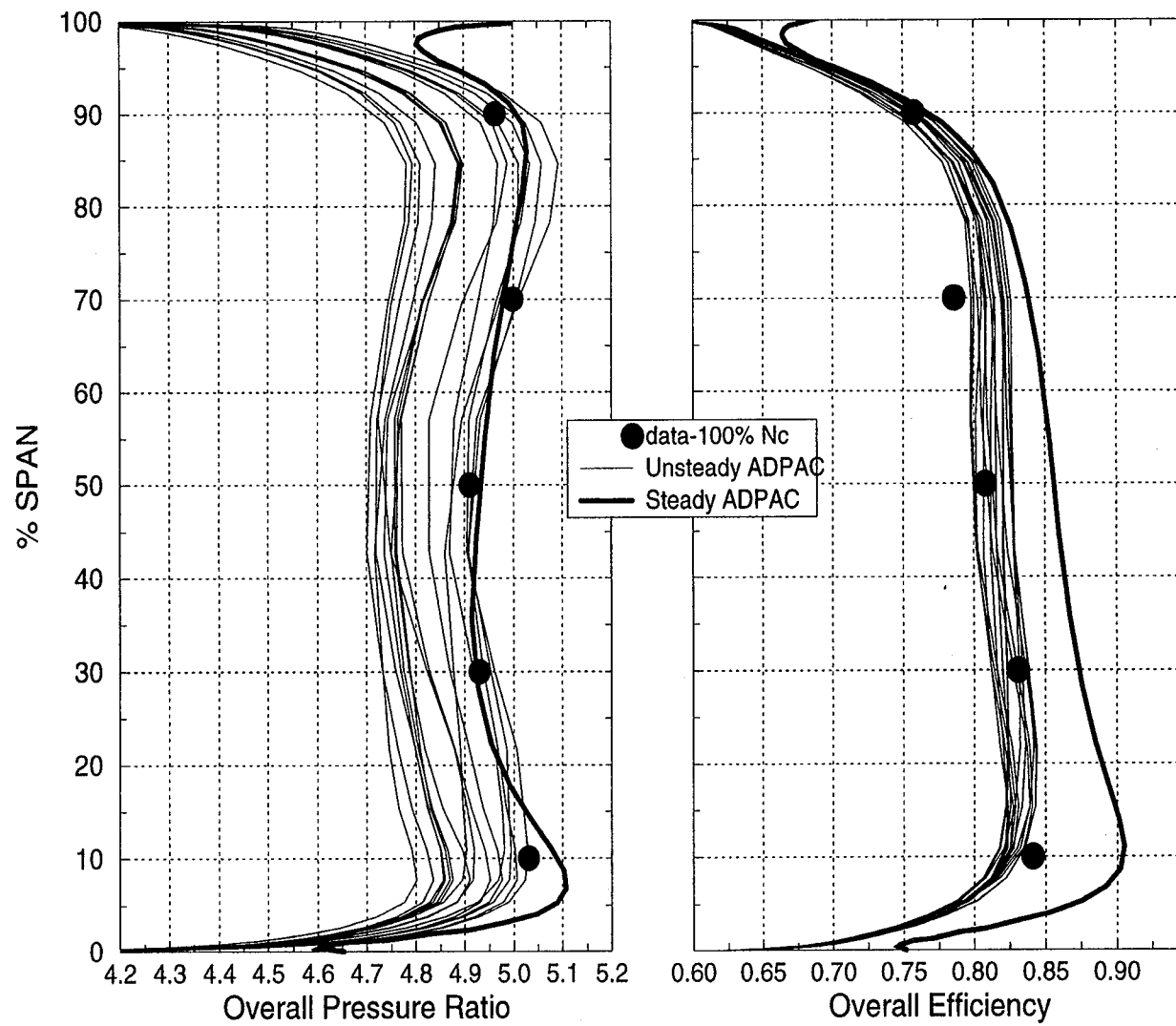
Figure 3-17. ADPAC predicted unsteady envelope of overall pressure ratio and efficiency.

41

The unsteady envelope of the first stage stator exit flow angle is plotted in Figure 3-18 and shows that the exit flow angle fluctuates as much as 5 degrees. This corresponds to an equivalent fluctuation in the downstream rotor incidence. Similar levels of unsteadiness were observed for the second stator and only 2 degrees of flow angle variations for the rotor exit. This unsteadiness influences compressor performance and should be considered during the design. However, even though an unsteady solution provides valuable flow field information, it is clearly too costly to make it practical for compressor design.
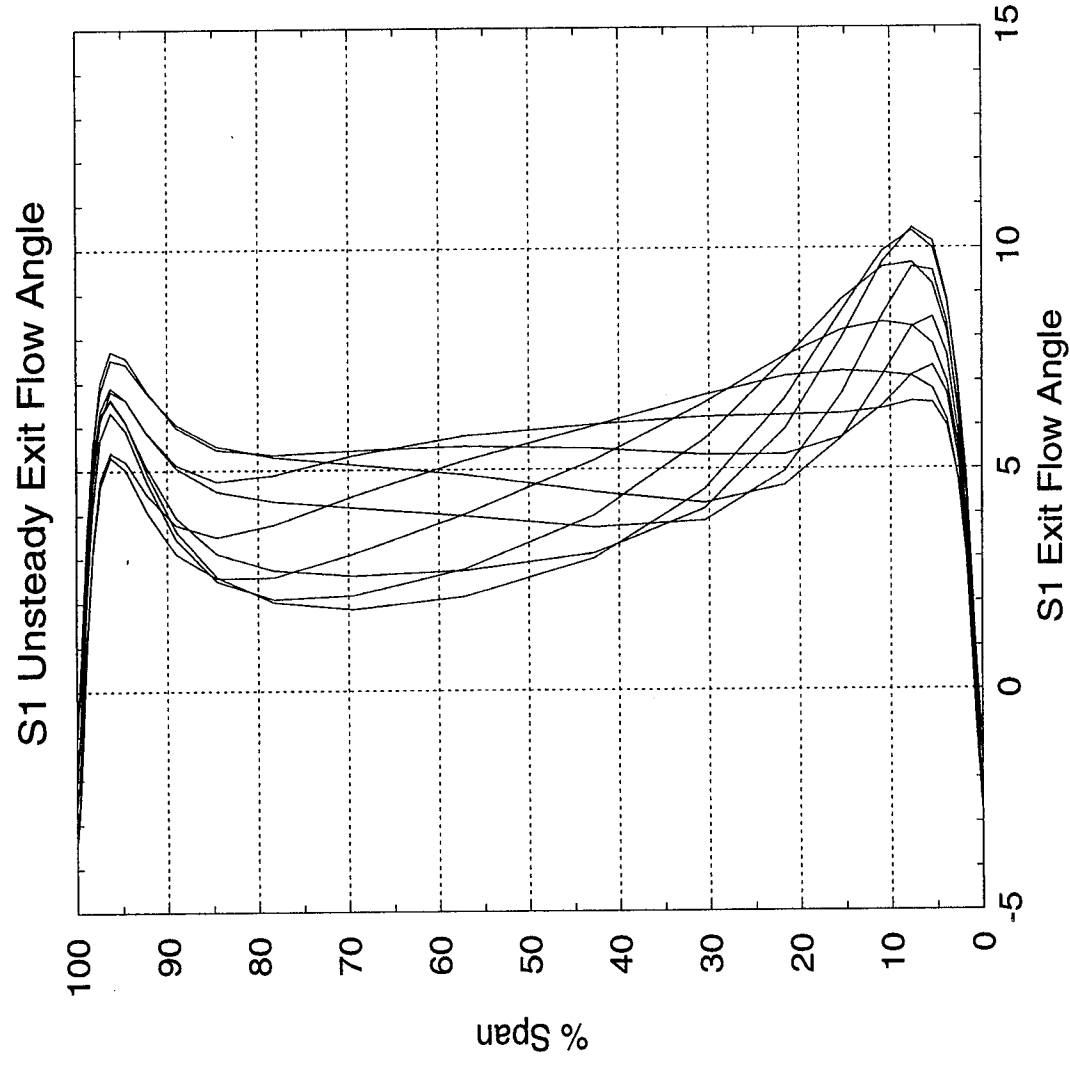
Figure 3-18. ADPAC predicted unsteady envelope of first stage stator exit flow angle.

43

3.2 *OCOM3D* Analysis

The ASTC compressor was also analyzed using the single blade row *OCOM3D* code by 'stacking' the solutions from each blade row. For the ASTC blade row calculations, the approach used was to calculate the flow for the first rotor blade row assuming uniform total pressure and total temperature profiles. The inlet guide vanes and their effect on the first rotor flow field were not simulated. For the first stator, the circumferential averaged exit conditions from the first rotor were used to specify the stator inlet total pressure, total temperature, and flow angles. This approach of stacking solutions by using the exit flow conditions from the upstream blade row to specify the inlet conditions for the adjacent downstream blade row was also used for the 2nd rotor and 2nd stator calculations. With this approach, the communication between the blade rows is all downstream and does not account for information which is necessarily passed upstream in this subsonic throughflow compressor. A drawback of this method is that there are many possible solutions for blade rows operating in their choke region. For this one-way multistage solution process many iterations are required to achieve the desired overall total pressure ratio. One iteration of this process employing the *OCOM3D* code was conducted on the ASTC at 102% corrected speed. The results of this analysis are presented in this Chapter along with comparisons to the *ADPAC* and *APNASA* results and test data.

3.2.1 Code Description

OCOM3D is a general multiple grid code for turbomachinery flow developed at Allison Engine Company (Ref 22). The flow solver is fully viscous and is based on the Beam and Warming implicit algorithm for solution of the Navier-Stokes equations. The analysis uses the blocked or embedded grids through the application of the CHIMERA grid embedding technique (Ref 23) developed at NASA Ames Research Center and Arnold Engineering Development Center (AEDC). Turbulence effects are modelled using the Thomas (Ref 24) formulation of the Baldwin-Lomax turbulence model.

With this analysis, relatively simple grids, each describing a component of the geometry or flow field region, are combined into a composite mesh. For individual blade rows, a body conforming O-grid is generated around the blade and H-grids attached are upstream and downstream to extend the computational domain. The attached H-grids are blocked with the O-grid. This means that the boundary points for the H-grids are coincident with inner field points in the O-grid, and the boundary points for the O-grid are coincident with the inner field points in the H-grids. Tip clearance flow is simulated on a fine H-grid embedded in the clearance region. The solutions on the blade passage O-grid and the embedded H-grid communicate through interpolation of boundary data in the overlap regions to produce a composite calculation.

3.2.2 Analysis Results

Rotor 1

The first rotor was modeled with a four block O-H mesh system that uses H-meshes for the inlet and exit regions, an O-grid around the airfoil, and an embedded H-grid for the tip clearance region. A tip section of the mesh is pictured in Figure 3-19 along with the grid dimensions. This mesh is much finer than was used for the ADPAC and APNASA models with over 4 times the grid points for a single blade row.
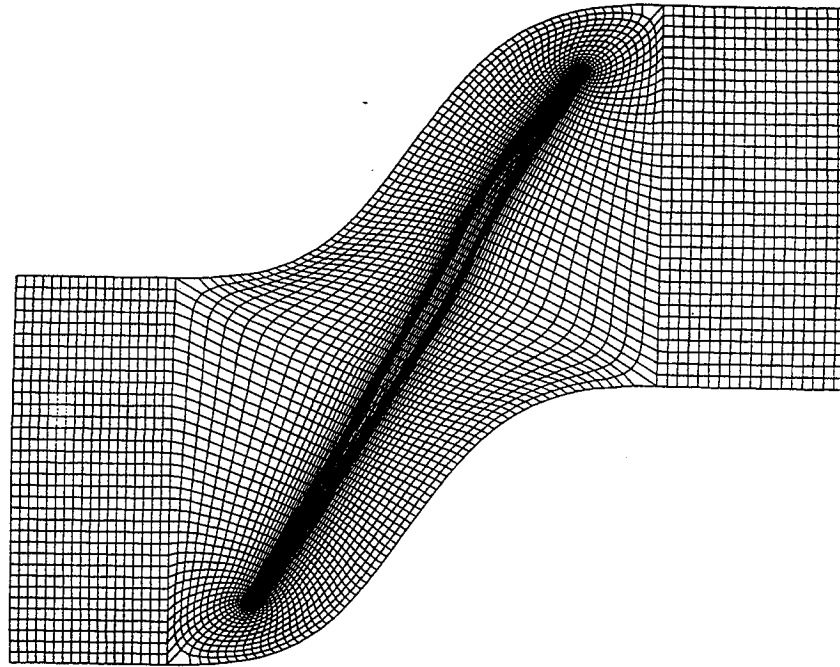
Block	Type	Dimension	Size
Inlet	H	20x35x47	32,900
Blade	O	191x31x47	278,287
Tip Clearance	H	151x25x7	26,425
Exit	H	20x35x47	32,900
Total			370,512

Figure 3-19. First stage rotor 4 block mesh system used by OCOM3D.

The overall results from this analysis at 102% design speed are compared with test data in Table 3-3 along with the *ADPAC* and *APNASA* results as shown in the table. The *OCOM3D* code does a better job of predicting the flow capacity of this rotor then the other codes. (The back pressure produced by the second stage prevented the measurement of first stage rotor choke flow in the test rig.) This better agreement with data may be related to the much finer mesh used by OCOM3D. On a mass-averaged basis, the *OCOM3D* predicted efficiency is 1.6% higher than measured values, however, the spanwise plot of efficiency shown in Figure 3-20 shows relative good agreement with the test data. Good agreement with the measured pressure ratio profile may also be seen in Figure 3-20. It is evident from this figure that the predicted efficiency from the APNASA code most closely matches the experimental data.

Table 3-3. OCOM3D results for rotor 1 compared to test data at 102% speed.

	Data	***OCOM3D***	***ADPAC***	***APNASA***
Flow rate, lbm/s	10.50	10.54	10.75	10.60
Pressure ratio	2.825	2.815	2.72	2.79
Efficiency,%	88.3	89.8	88.2	88.0
Choke Flow, lbm/s	-----	10.63	--	--

It should be noted that the test data plotted in Figure 3-20 includes the loss associated with the long inlet which includes 2 sets of struts and the IGV's (see Figure 2-3). The test values listed in Table 3-3 however, represents rotor only performance by assuming a 1.5% inlet loss determined by an inlet system calibration measurement (Ref 25).
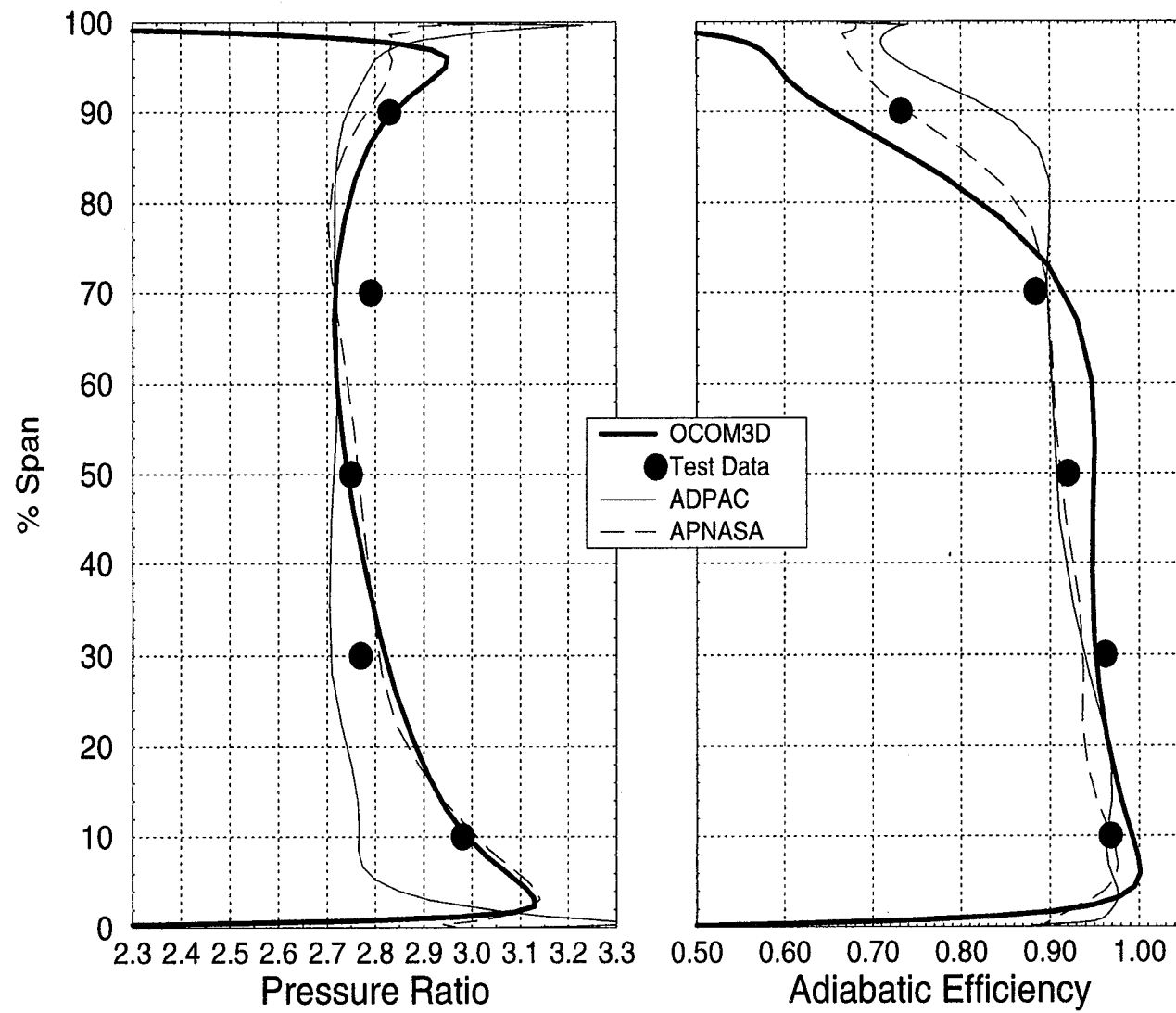
Figure 3-20. Predicted first stage rotor pressure ratio and efficiency profiles.

The predicted blade-to-blade relative Mach number contour plot at 91% span is shown in Figure 3-21. This figure shows the details of the predicted passage shock near the leading edge and the shock-boundary layer interaction on the suction surface. This figure also shows substantial boundary layer development on the pressure surface that is initiated by a weaker passage shock interacting with the pressure surface boundary layer. The dense mesh used for this solution allows for these details to be resolved.

Stator 1

The first stage vane was modeled with *OCOM3D* using the O-H mesh system illustrated in Figure 3-22. The endwall clearances associated with this variable vane, of approximately 0.010 inches, were not modeled in this analysis. The circumferential mass-averaged exit pressure, temperature and flow angle profiles from the first rotor solution were used as the inlet conditions for the analysis of this vane and are shown in Figure 3-23. The exit static pressure was set to obtain the same flow rate as was calculated in the first stage rotor solution.

The inlet corrected flow and total pressure loss values from the three analysis methods are listed in Table 3-4. This table shows a wide range in total loss predicted by the codes with *OCOM3D* and *ADPAC* predicting much lower loss than *APNASA*. The predicted radial profile of total pressure loss from *OCOM3D* is compared with *ADPAC* and *APNASA* predictions in Figure 3-24. A comparison to test data could not be made as no data were obtained at the trailing edge of the first stator.

Table 3-4. Predicted stator 1 flowrate and total pressure loss comparison.

	OCOM3D	ADPAC	APNASA
Corrected Flow, lbm/s	4.52	4.72	4.56
Total Press Loss, %	1.8	2.1	4.7
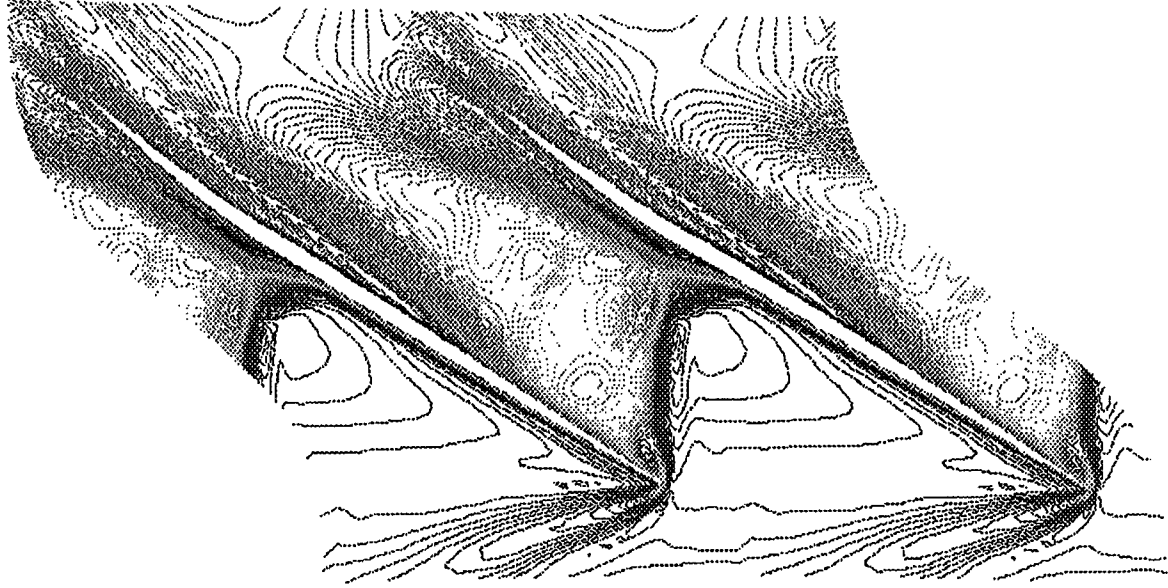
Figure 3–21. OCOM3D predicted relative Mach number contours at 91% span.
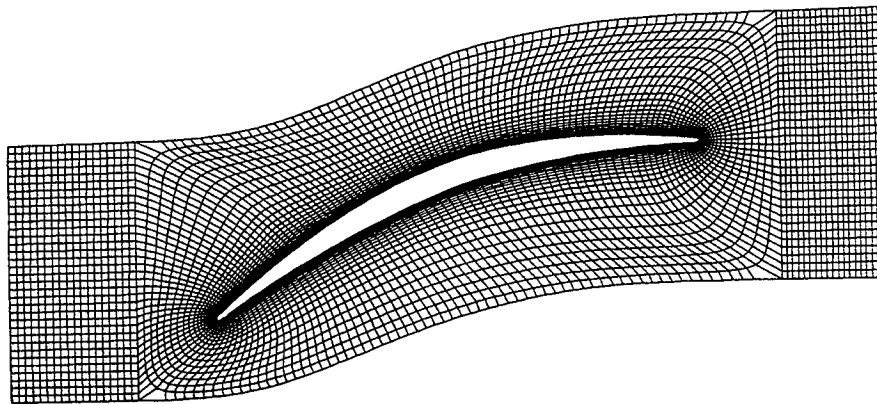
Figure 3-22. *Radial slice of first stage stator mesh used by OCOM3D.*

51
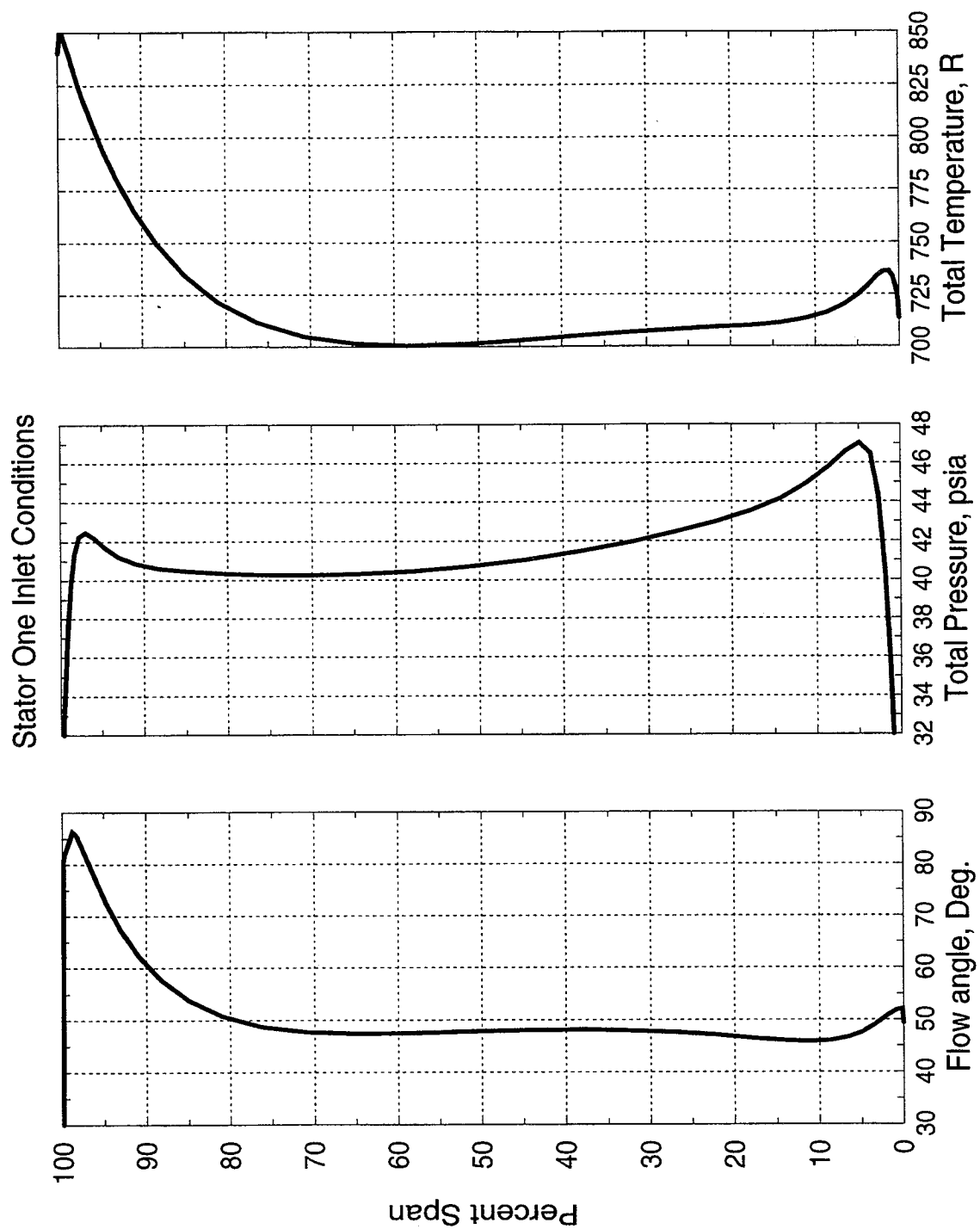
Figure 3-23. Inlet boundary conditions used for OCOM3D stator 1 analysis.
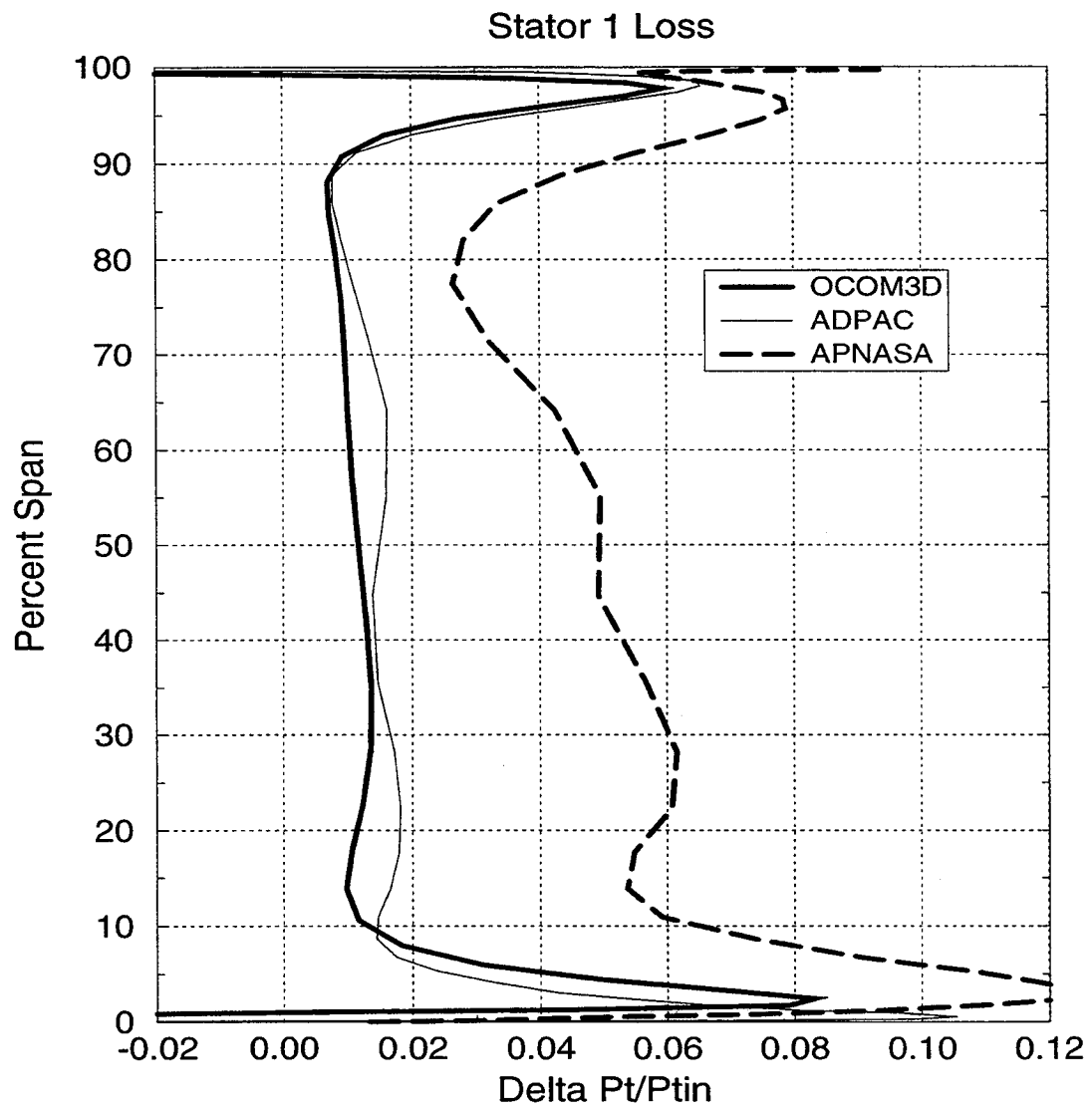
Figure 3-24. Comparison of predicted stator 1 total pressure loss.

The *OCOM3D* results show some interesting flow field behavior as illustrated by the suction surface particle trace of Figure 3-25. This figure shows the predominately radial flow near the surface demonstrating the highly three-dimensional nature of the flow field caused by strong radial pressure gradients and tangential bow. This Figure also shows a vortex near the leading edge at the tip and a sink or stagnation point at mid span near the trailing edge. The Mach number contour plots of Figure 3-26 show the boundary layer to be separated near the leading edge at 90% span (location of the vortex) and at 75% chord at mid span (location of the stagnation point). The suction surface boundary layer at 10% span is not separated in the normal sense of having backflow, however, the purely radial flow downstream of the shock produces large amounts of blockage similar to separated flow.

Rotor 2

For the analysis of the second rotor, a four block mesh system similar to that used in the first rotor was used. The first stator circumferential mass averaged exit conditions were used as inlet conditions for this rotor and are shown in Figure 3-27. As in the previous blade row, the intent was to set the exit static pressure at a value to obtain a flowrate of 10.54 lb/sec. This would be the same flow rate as was calculated in the previous blade row solutions. However, the rotor became unstarted at a flowrate of 10.59 lb/sec and a solution could not be obtained at a lower flow rate. The pressure ratio at this condition was 2.14 which is much higher than that predicted by the other models as shown in Table 3-5 and Figure 3-28. This table also shows that the inlet corrected flow is low, explaining the higher pressure ratio and stalling conditions for the *OCOM3D* solution. This situation was caused by the higher pressure ratio predicted for rotor 1 compared to *ADPAC* and *APNASA*. At this point, a new solution for rotor 1 and stator 1 should be obtained at a lower pressure ratio to raise the second stage corrected flow. However, for this exercise the process will continue using these results.
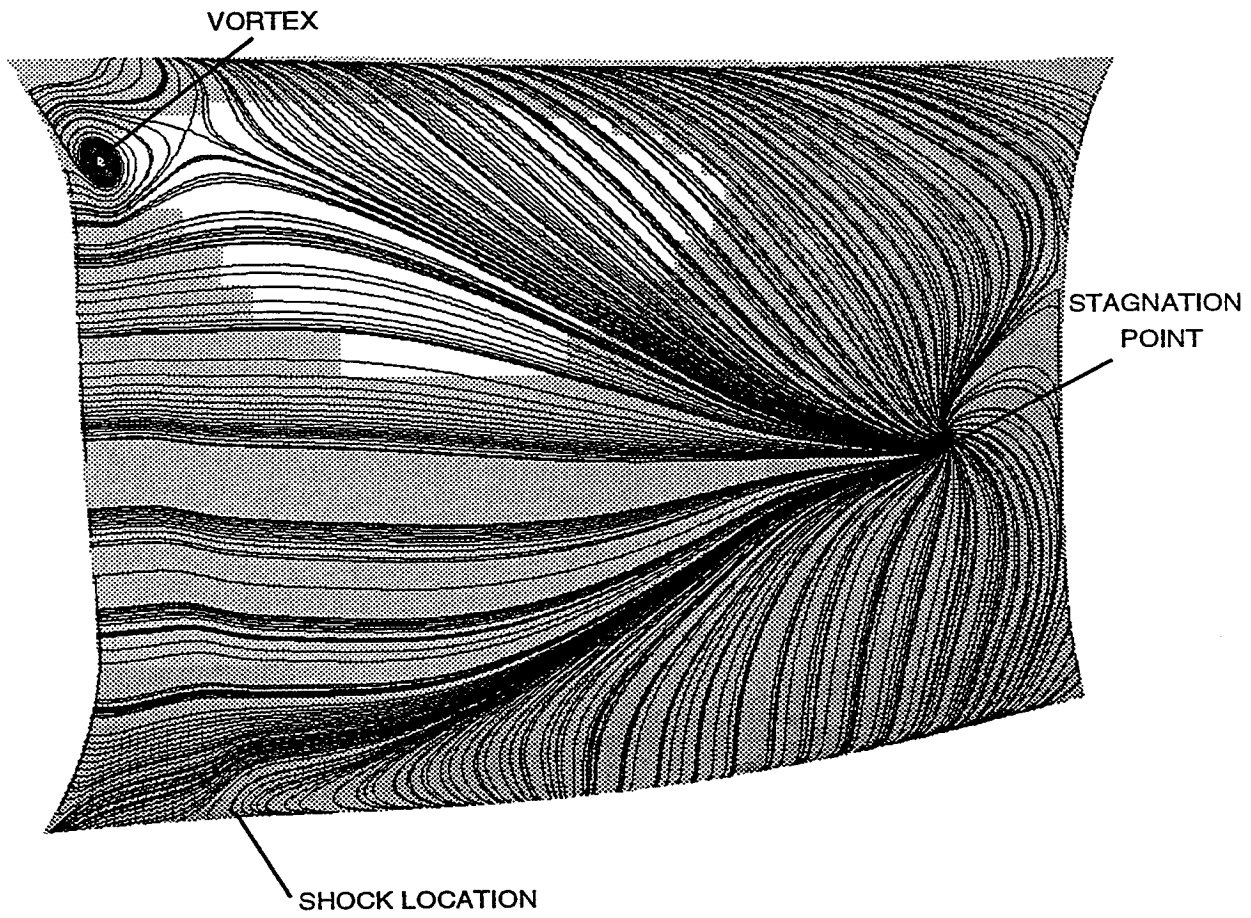
Figure 3–25. Stator 1 suction surface particle trace from OCOM3D.

10% SPAN **50% SPAN** **90% SPAN**
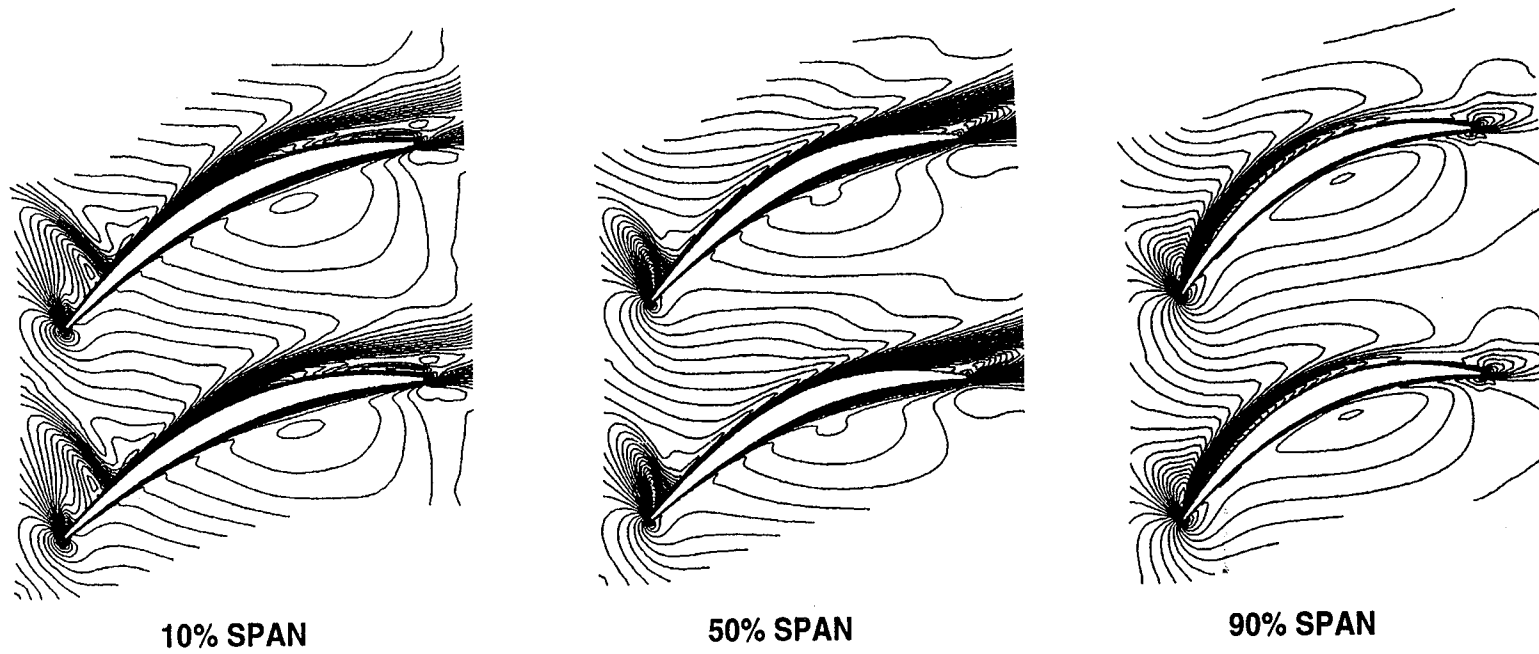
Figure 3–26. Stator one OCOM3D predicted Mach number contours.
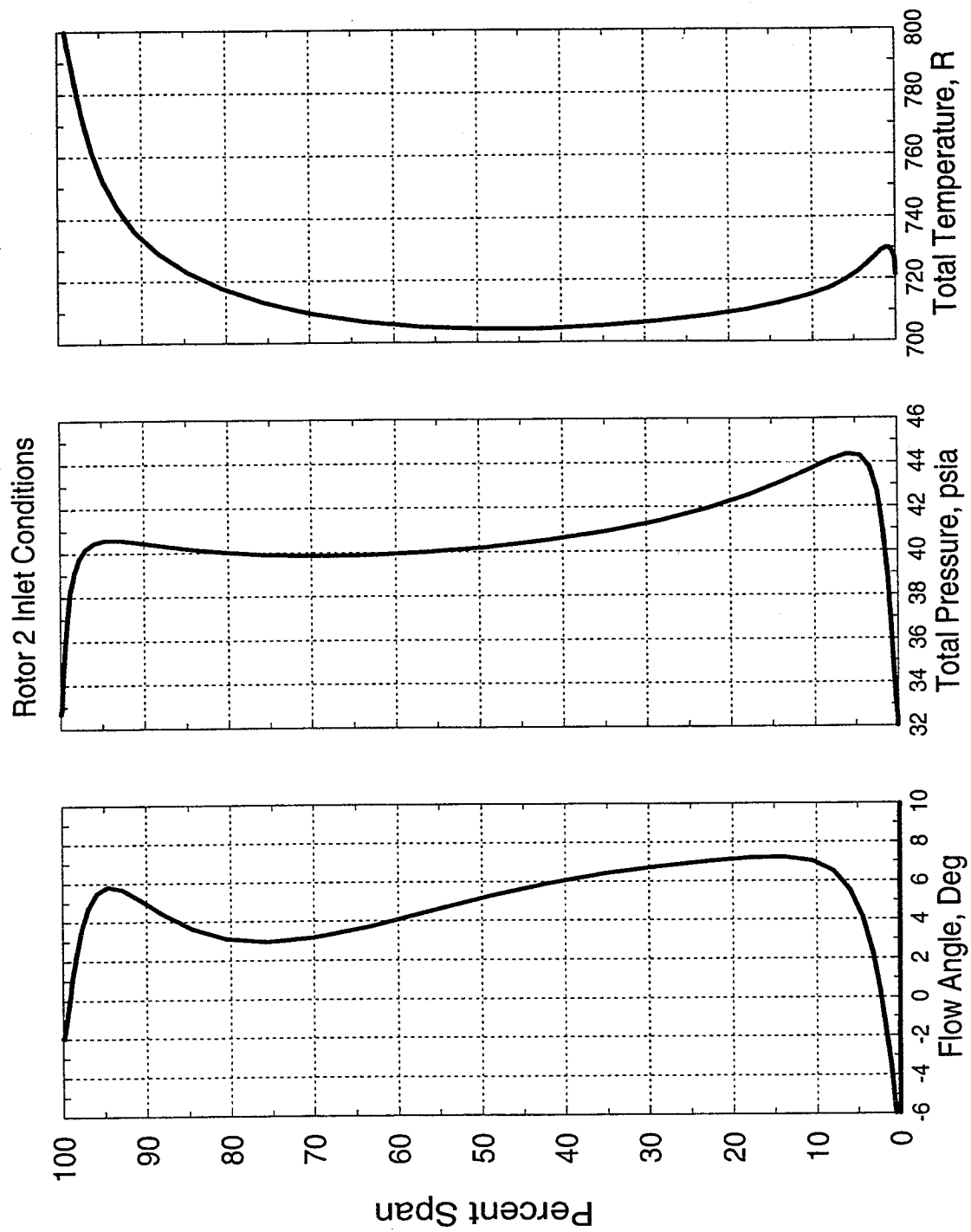
Figure 3-27. Inlet boundary conditions used for OCOM3D rotor 2 analysis.

57
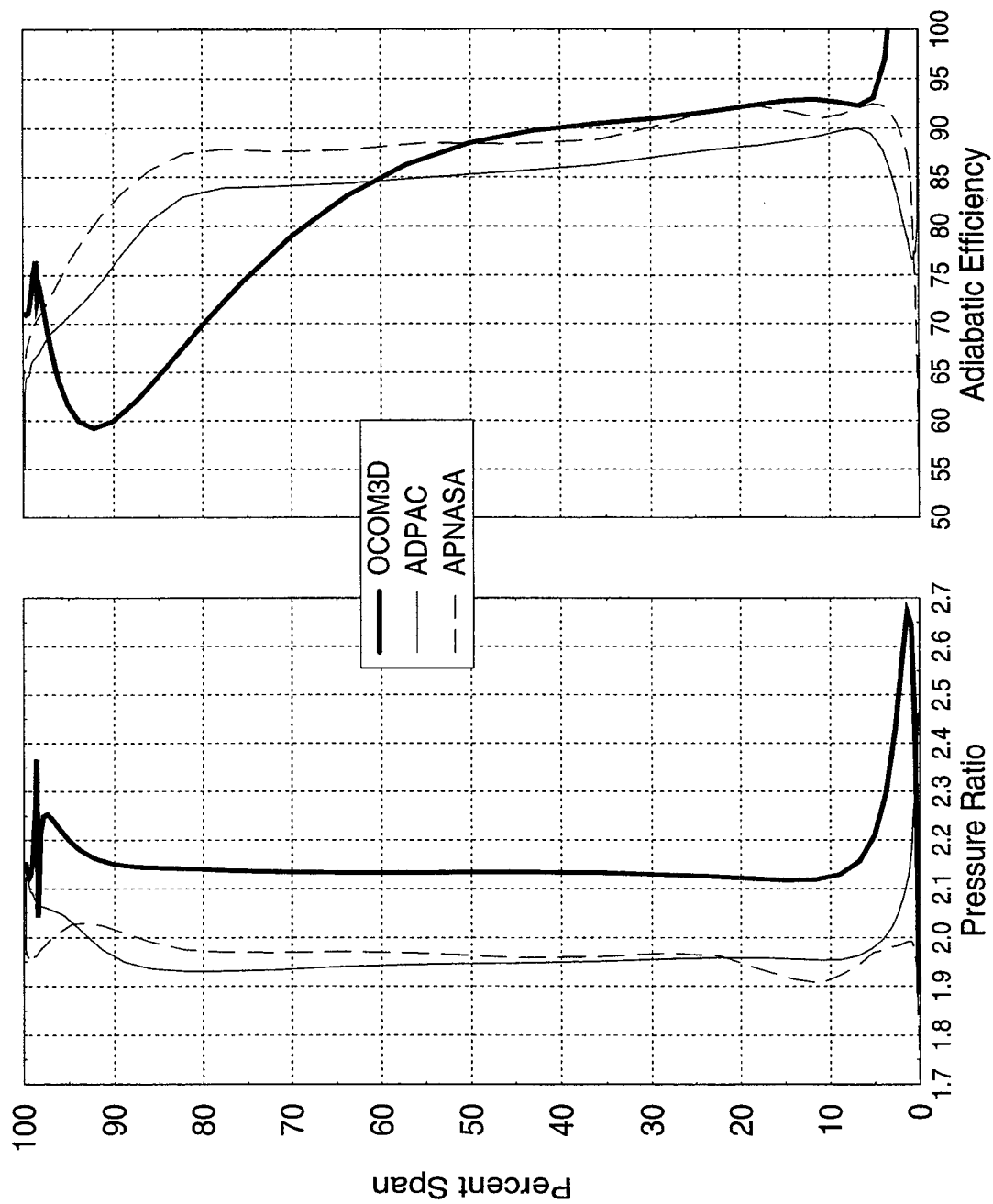
Figure 3-28. Comparison of predicted rotor 2 pressure ratio and efficiency profiles.

Table 3-5. OCOM3D results for rotor 2 compared to ADPAC and APNASA results.

	OCOM3D	**ADPAC**	**APNASA**
Flow rate, lbm/s	10.59	10.75	10.6
Corr. flow, lbm/s	4.61	4.82	4.88
Pressure ratio	2.14	1.947	1.976
Efficiency,%	83.3	83.2	88.8

Although the predicted average rotor efficiencies are nearly equal for the *ADPAC* and *OCOM3D* predictions, the radial efficiency profiles of Figure 3-28 are very different with *OCOM3D* predicting much lower efficiency above mid span due to the unstarted shock. The blade-to-blade relative Mach number contour plot at 90% span, presented in Figure 3-29, shows the bow shock to be detached from the leading indicating the rotor is unstarted or spilled. A large suction surface boundary separation is also evident in Figure 3-29 as a result of the shock interaction with the boundary layer.

Stator 2

The mesh used for the analysis of the second stator was identical in size to that used for stator 1. The predicted circumferential mass averaged exit pressure, temperature and flow angle distributions from the second rotor solution presented in Figure 3-30 were used as the inlet conditions. The exit static pressure was set to obtain nearly the same flow rate as was calculated in the first stage rotor solution.
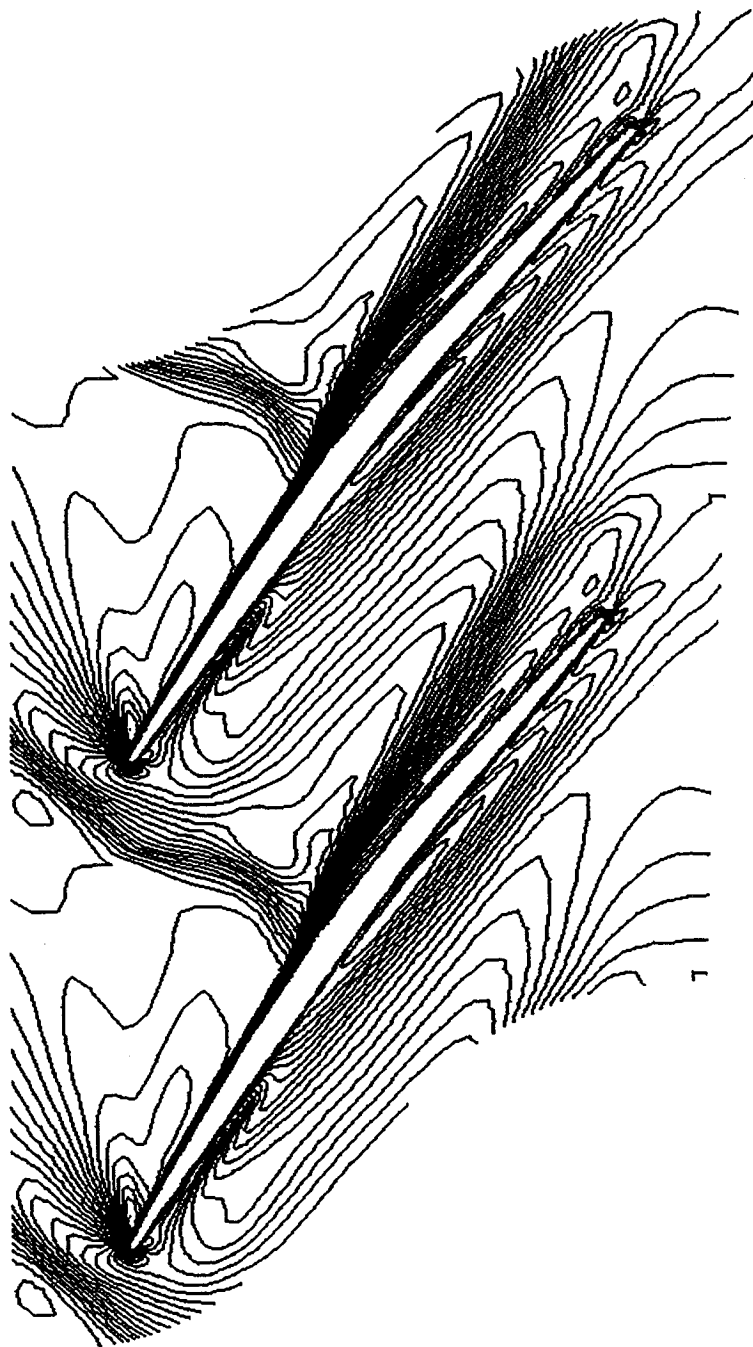
Figure 3–29. OCOM3D predicted rotor 2 relative Mach number contours at 91% span.
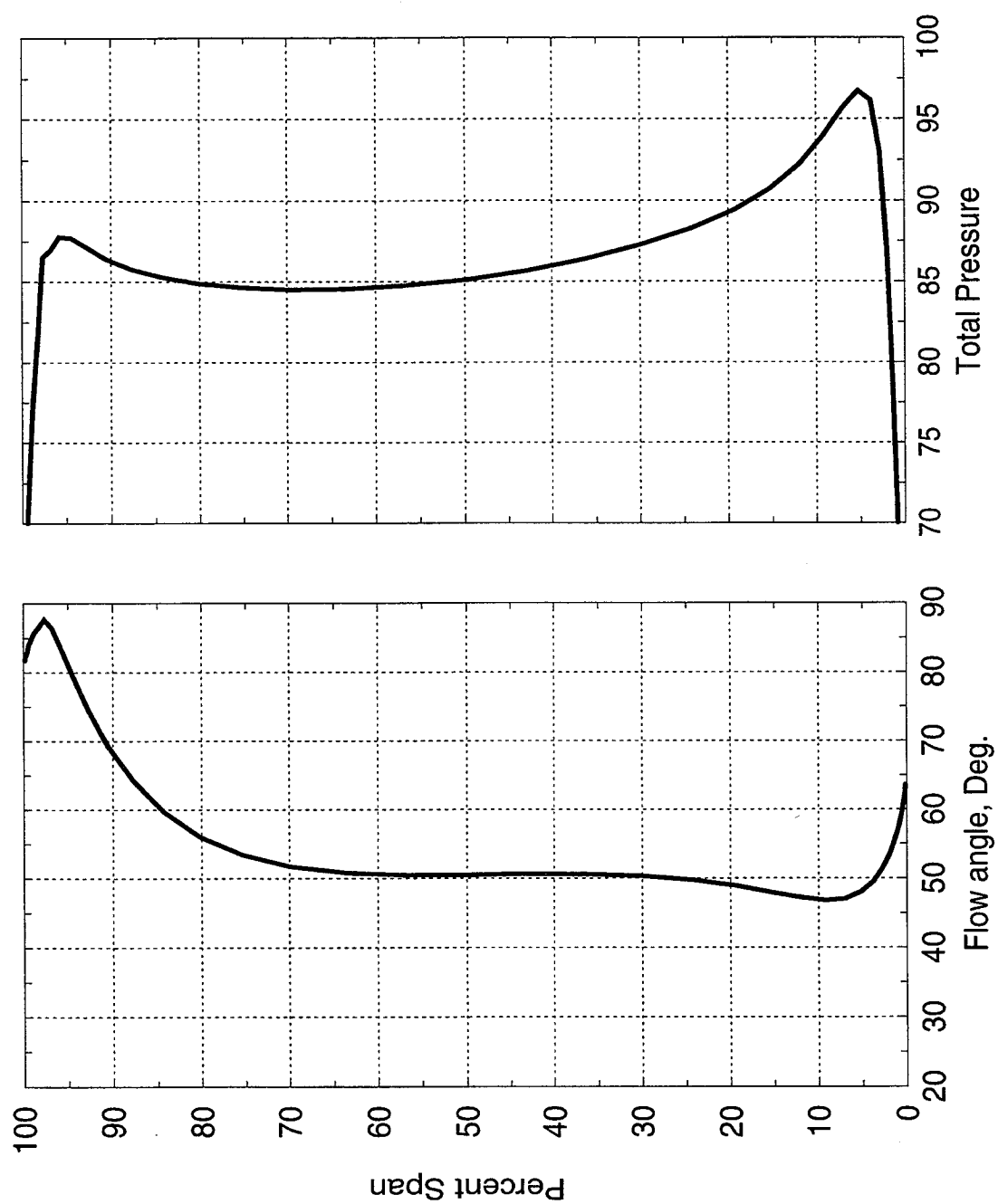
Figure 3-30. Inlet boundary conditions used for OCOM3D stator 2 analysis.

The resulting inlet corrected flows and total pressure losses predicted by the three analysis methods are listed in Table 3-6. This table shows a wide range in total loss predicted by the codes as was the case for stator 1. However, for stator 2 *OCOM3D* predicted high loss similar to that predicted by *APNASA*. The radial profile of total pressure loss is shown in Figure 3-31. The *OCOM3D* inlet corrected flow is low for the same reason discussed for rotor 2. The low corrected flow and the radial profiles out of rotor 2 also explain the high predicted total pressure loss.

Table 3-6. Predicted stator 2 flowrate and total pressure loss comparison.

	OCOM3D	ADPAC	APNASA
Flow rate, lbm/s	2.42	2.76	2.74
Total Press Loss, %	3.7	1.95	3.95

To show some of the complex secondary flow features captured by this code, a plot of suction surface particle traces is shown in Figure 3-32. This figure shows the predominately radial flow near the surface demonstrating the highly three-dimensional nature of the flow field caused by pressure gradients and tangential bow. This figure also shows the boundary layer has separated near the leading edge at the hub. The Mach number contour plots of Figure 3-33 show the boundary layer to be separated over most of the suction surface chord at 10% and 50% spans. The suction surface boundary layer at 90% span is separated over the front portion of the blade and then reattaches at 50% chord.
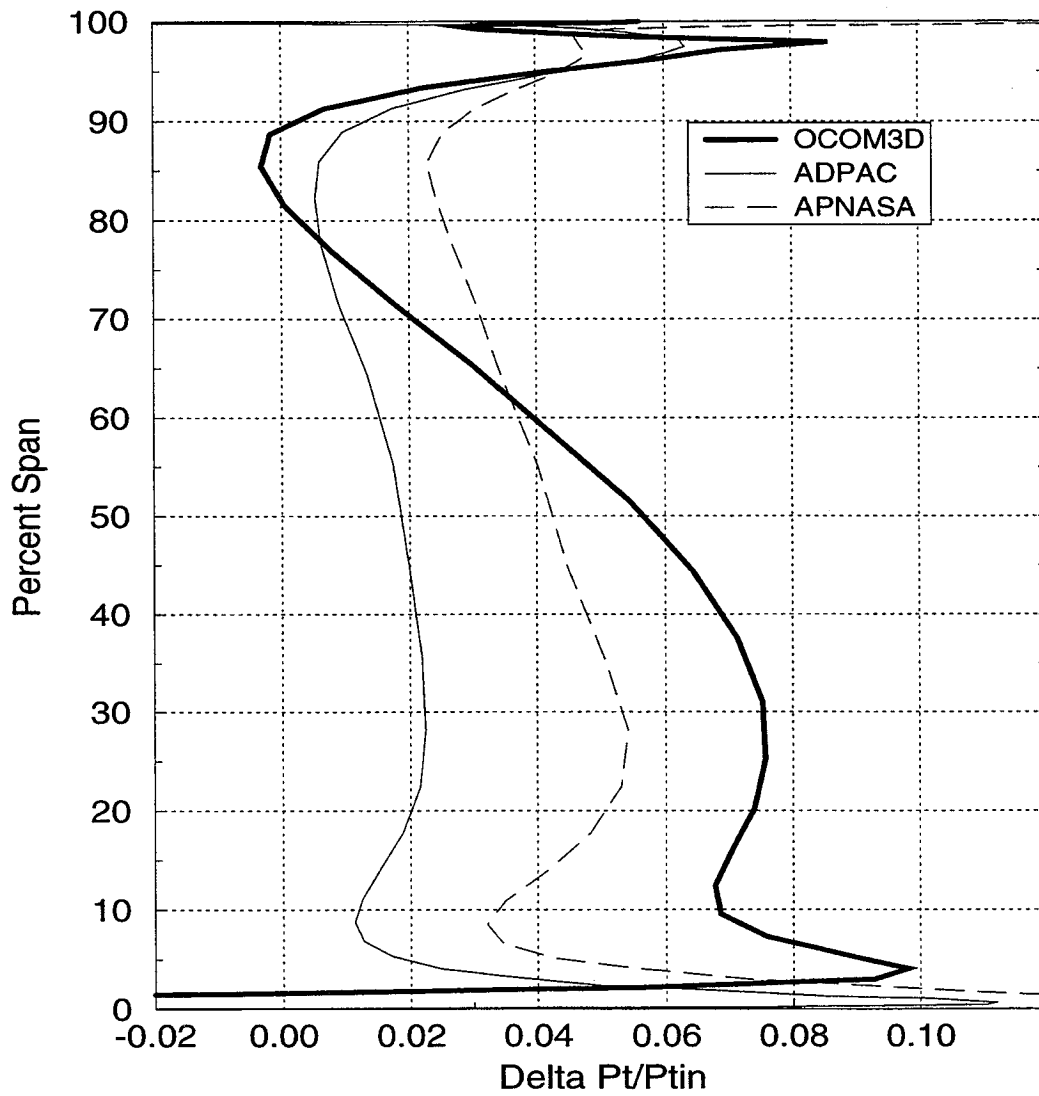
Figure 3-31. Comparison of predicted stator 2 total pressure loss.
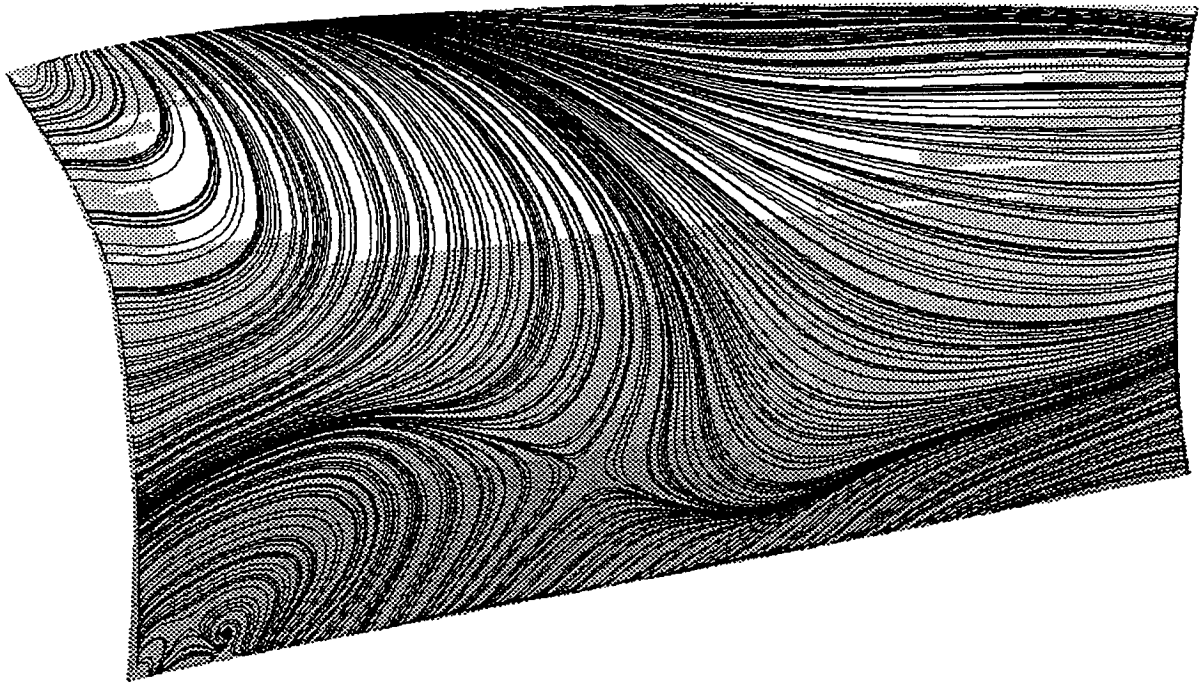
Figure 3–32. Stator 2 suction surface particle trace from OCOM3D.

10% SPAN   **50% SPAN**   **90% SPAN**
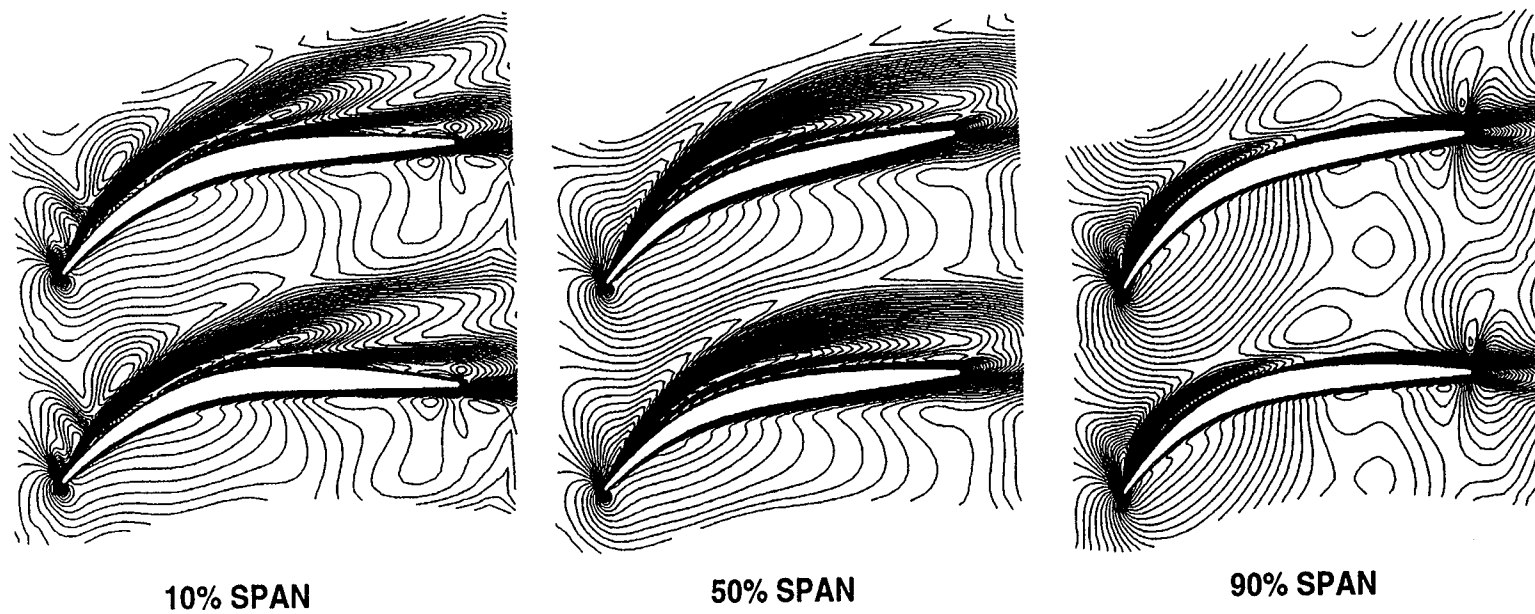
Figure 3–33. Stator two OCOM3D predicted Mach number contours.

3.3 Summary of Results

The stage and cumulative performance results for the three steady-state flow models are compared with test data in Table 3-7. Based on this information and the radial profiles presented in this chapter and the previous chapter, the conclusion can be made that the *APNASA* average passage code does a better job at predicting the performance and flowfield details of this highly loaded two stage compressor.

Table 3-7. Mass-average stage performance predictions at 102% speed.

	Data		ADPAC		APNASA		OCOM3D	
	Rc	Eff.	Rc	Eff.	Rc	Eff.	Rc	Eff.
Stage								
IGV			0.977	-----	0.982	-----	0.985	---
Rotor 1	2.82 ±0.06	88.2 ±0.8	2.73	90.6	2.79	88.0	2.82	90.5
Stage 1			2.67	88.3	2.66	83.6	2.77	89.4
Rotor 2			1.95	83.6	1.98	88.9	2.16	83.3
Stage 2			1.92	81.2	1.90	80.9	2.08	78.8
Cumulative								
IGV			0.977	------	0.982	-----	0.985*	-----
Rotor 1	2.78 ±0.06	86.7 ±0.8	2.66	88.2	2.74	86.4	2.78	89.1
Stage 1			2.60	85.9	2.61	82.0	2.73	87.2
Rotor 2			5.08	83.4	5.16	83.2	5.89	84.3
Stage 2	5.03 ±0.01	80.5 ±0.5	4.99	82.3	4.96	79.6	5.66	81.8

* Inlet loss from test results.

4.0 FORWARD SWEPT ROTOR ASSESSMENT

It was revealed in chapter 2 that the ASTC first stage rotor would not swallow the passage shock at 100% speed as designed. It had been determined that this was caused by the low flow capacity of the second stage thereby back pressuring the first stage. This problem could be remedied by increasing the flow capacity of the second stage and/or redesigning the first rotor to tolerate the higher back pressure. The objective of the chapter is to assess the feasibility of improving the shock starting characteristic of the ASTC first stage rotor with blade sweep through numerical analysis and then experimentally verify these findings.

4.1 Aerodynamic Design and Analysis

Fan and compressor designers have long been attempting to reduce shock loss by sweeping the rotor blade aft to produce a more oblique shock. Previous investigations found that back sweep has an adverse affect on stall margin. Results from 3-D Navier-Stokes models for back sweep reveal that the passage shock tends to remain near the same location within the annulus as the rotor is swept back as illustrated in Figure 4-1. This places the rotor leading edge closer to the shock causing the rotor to unstart sooner (and start later) leading to less stall margin. The results of these investigations led to the concept of sweeping the airfoil forward to move the leading edge away from the passage shock to increase stall margin.

The baseline first stage rotor of the ASTC was redesigned and restacked to introduce forward sweep. The only aerodynamic design constraints were to use the same flowpath and rpm as the baseline design. The rotor exit conditions were also consistent with the baseline design to match with the existing first stage vane. The forward swept rotor had to meet structural integrity requirements to safely run the test. Since the intent of this program was to improve the performance and shock starting characteristics of the baseline first stage rotor several design parameters are different for the two designs eliminating a true back-to-back comparison for swept and unswept rotors.
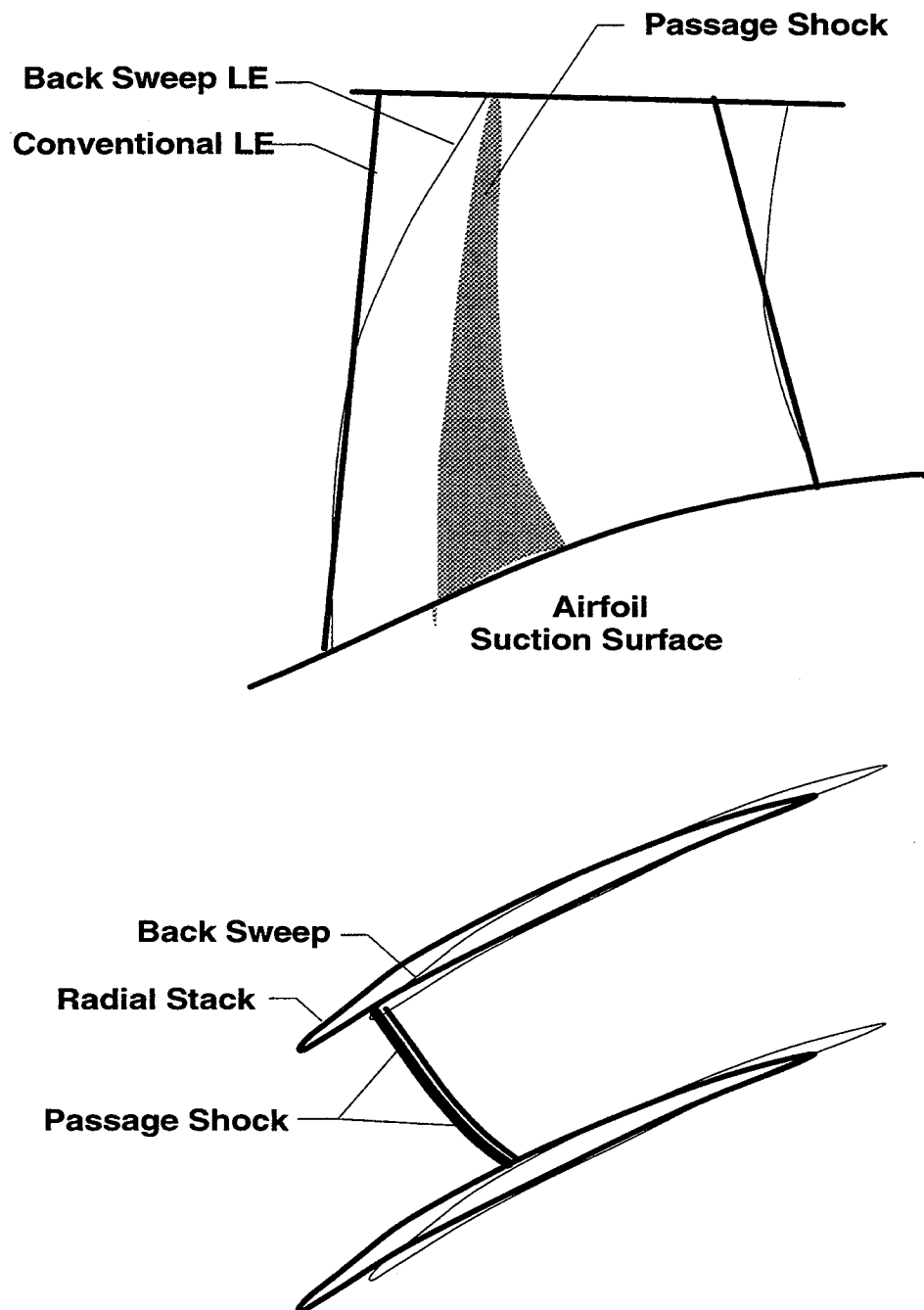
Figure 4-1. Schematic showing effect of back sweep on shock location.

The design of the forward swept rotor was accomplished using the Allison Axial Compressor Design System briefly described in Chapter 2. The three-dimensional viscous code *ADPAC* (see Chapter 3) was used as the primary analysis tool to determine the performance of each design configuration. The predicted radial profiles of a few main design parameters are plotted in Figure 4-2 and Figure 4-3 where they are compared to the baseline design profiles. These figures show how similar the two designs are with the exception of the redesigned rotor having 12.5% higher solidity and higher tip choke margin. The final salient design parameters for the redesigned swept rotor are listed in Table 4-1. The rotor inlet corrected flow is higher than the compressor flow presented earlier due to the absence of the inlet guide vane loss.

Table 4-1. Comparison of salient design parameters of the redesigned and baseline rotors.

Parameter	Redesign	Baseline
Corr. Flow rate, lbm/s	10.63	10.63
Pressure Ratio	2.69	2.69
Corr. Tip Speed, ft/s	1676	1676
Inlet Spec. Flow, lbm/s-ft^2	42.5	42.5
No. Airfoils	18	16
Mean Solidity	1.993	1.767
Aspect Ratio	0.672	0.680

The forward sweep was accomplished by using nonlinear leans in both the axial and tangential directions. The amount of sweep introduced was limited by structural design criteria discussed in the following section. As a result, a parametric study on sweep was conducted to find the optimum sweep to maximize stall margin and still meet the structural requirements. To limit the number of variables, the axial lean of the airfoil was fixed and the non-linear tangential leans were varied. The leading edge axial sweep angle profile used for the redesigned blade is compared to the baseline design in Figure 4-4. Meridional views of the two rotors are compared in Figure 4-5 illustrating the amount of forward lean in the new design. A wide range of tangential leans were investigated to determine their impact on rotor performance and steady-state stress levels. Several of the tangential lean angle radial distributions are plotted in
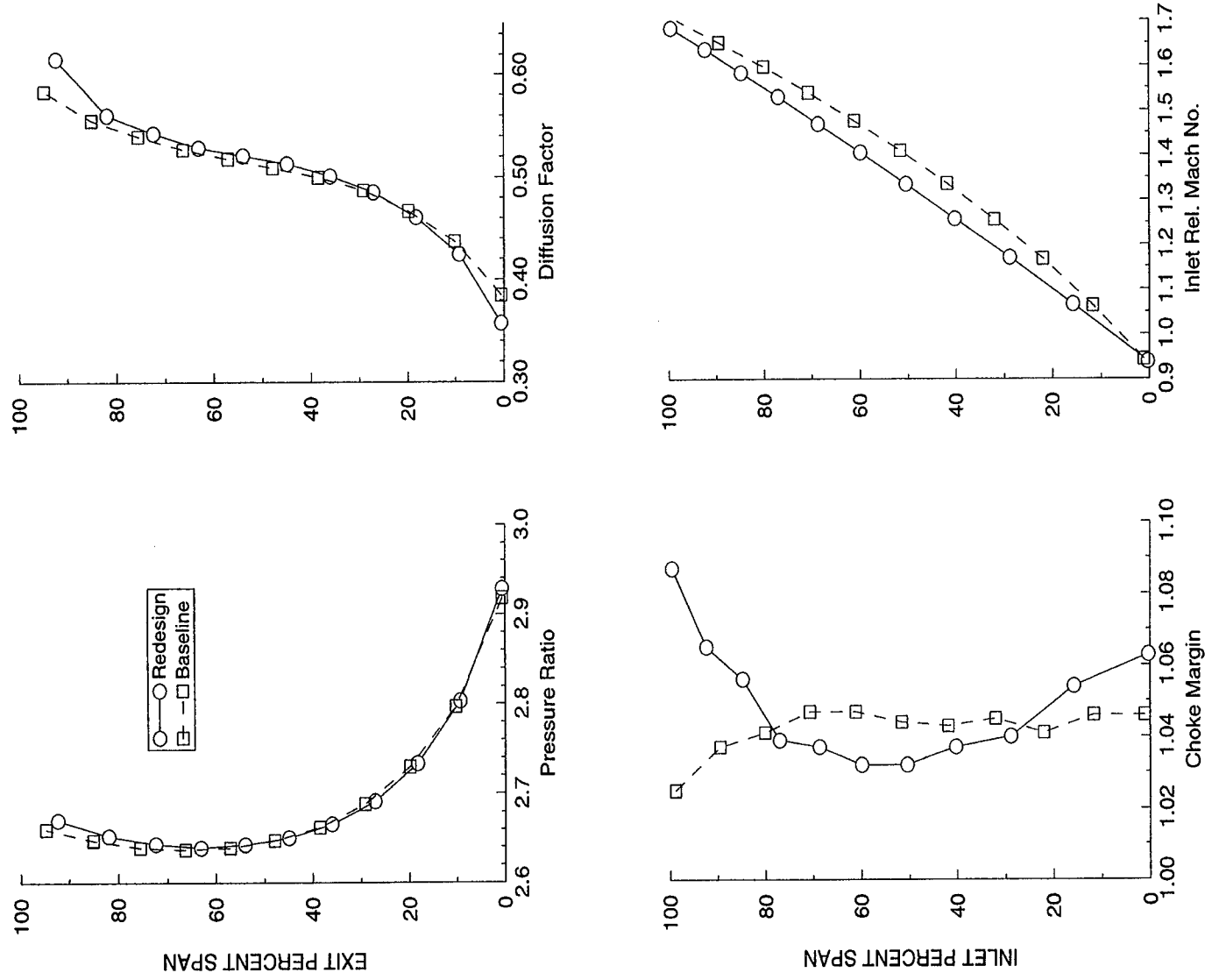
Figure 4-2 Comparison of design parameters for the forward swept and baseline rotors.

70

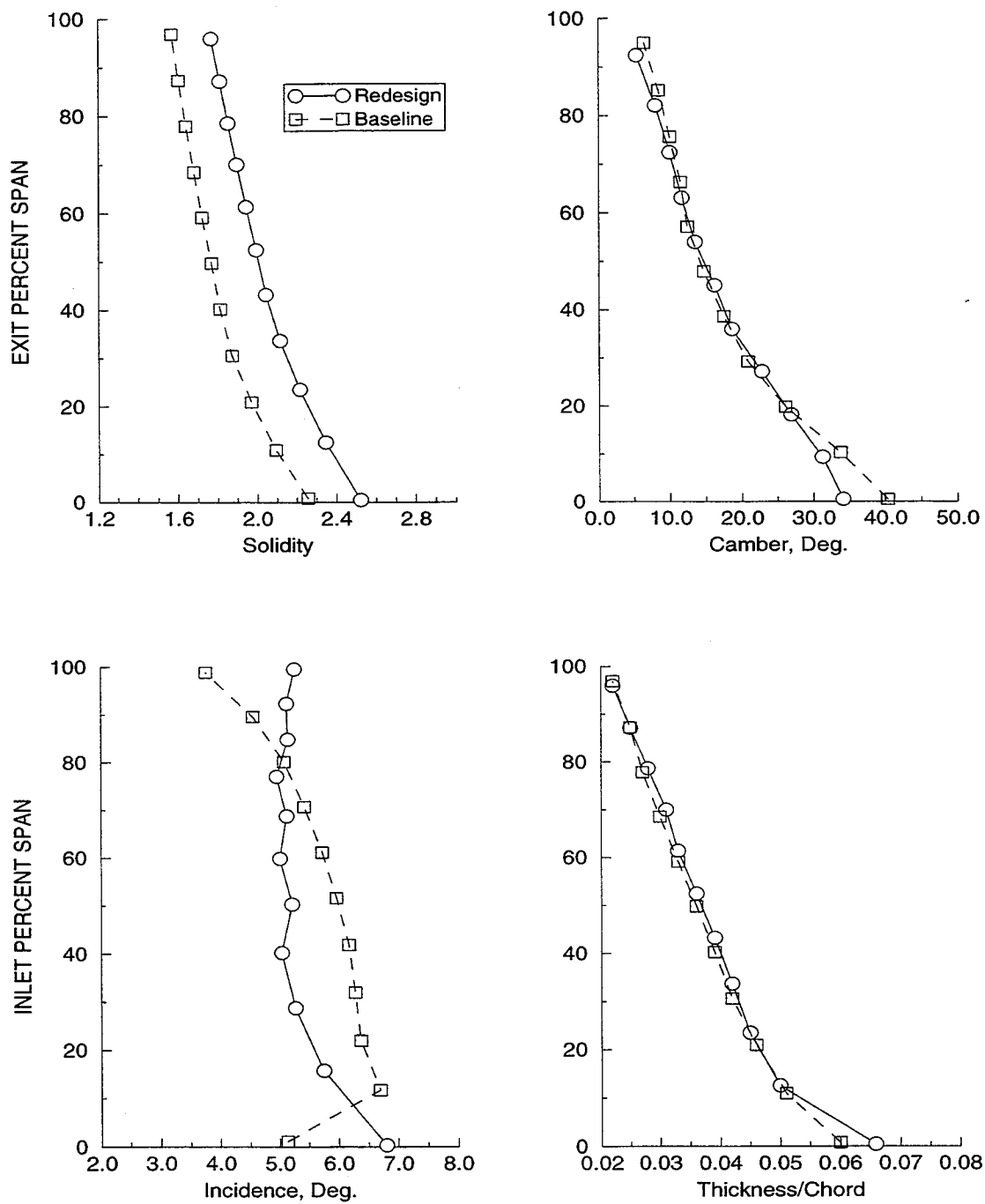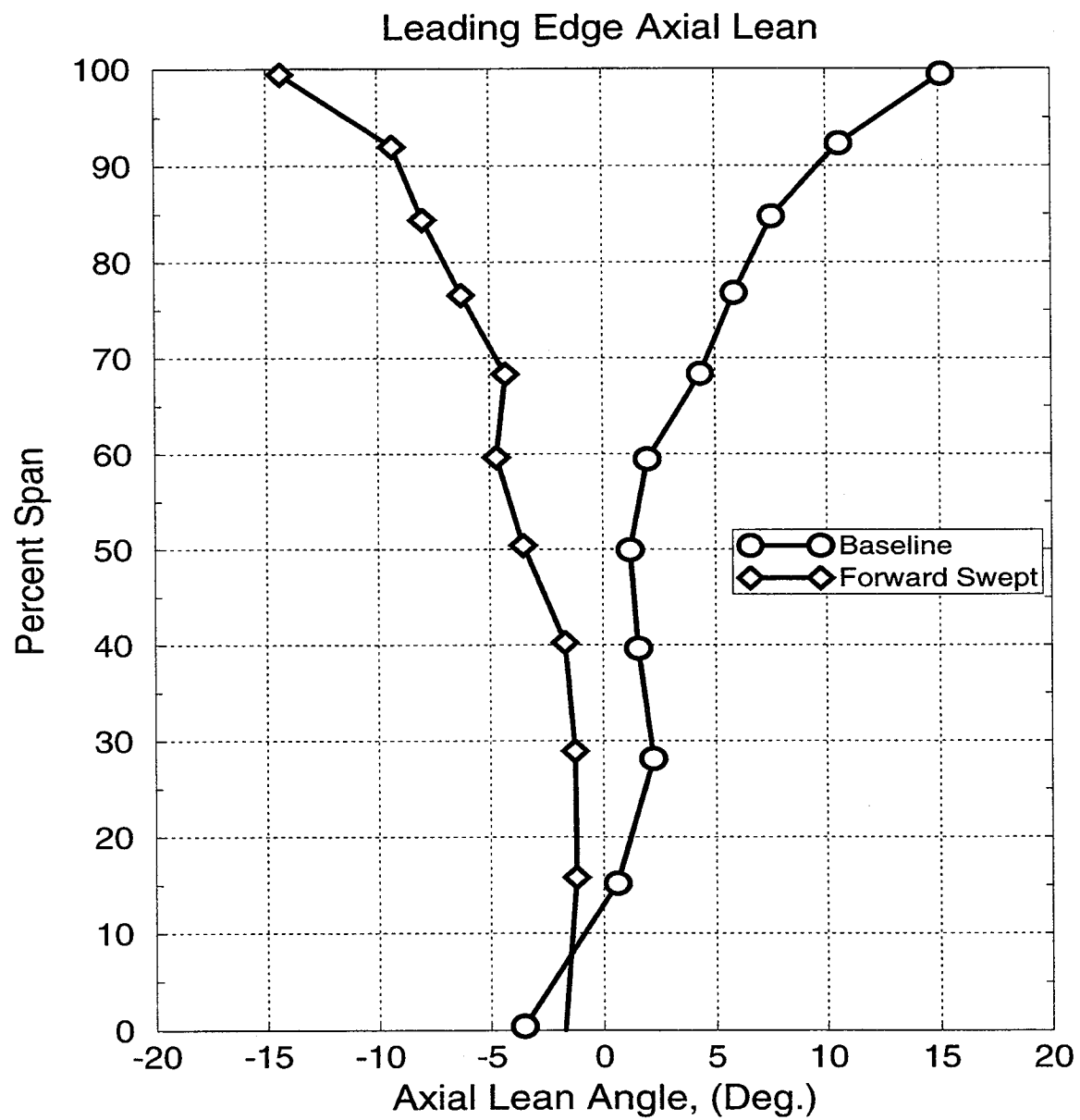*Figure 4-3 Comparison of design geometry parameters for the forward swept and baseline rotors.*
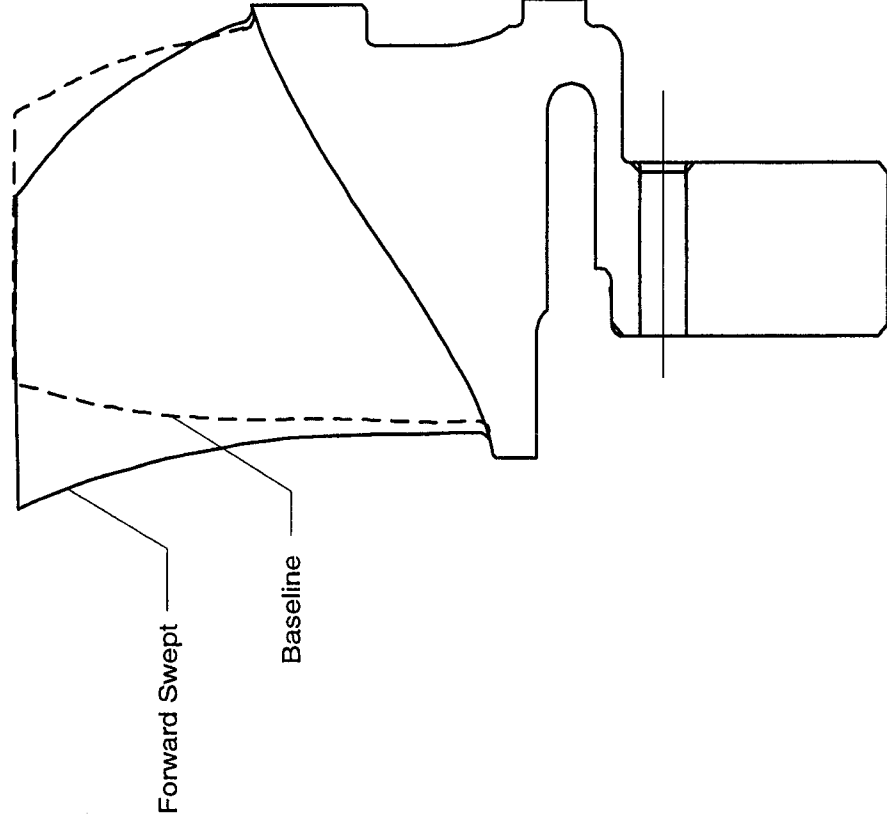
71

Figure 4-4 Rotor leading edge axial sweep angle profile.

Forward Swept

Baseline

Figure 4-5. *Meridional view comparing the forward swept rotor to the baseline rotor.*

73

Figure 4-6 where negative lean is in the opposite direction of rotation. The final selected tangential lean along with the baseline linear tangential lean is also presented in Figure 4-6. The illustration in Figure 4-7 shows the final 3D shape of the forward swept rotor design.

To determine the impact on performance of the many blade tangential leans described in Figure 4-6, *ADPAC* was used to predict the 100% design speed characteristic to stall for each lean. The results for a few of the designs are shown in Figure 4-8. It is evident from this figure that the tangential lean has a significant influence on the shape of the speedline, the maximum pressure ratio capability and the peak efficiency. In general, increased negative tangential lean produces flatter (more flow range) speedlines than positive lean. The final design of the forward swept rotor shows it to have 6% stall margin while the baseline rotor has no stall margin from the design pressure ratio value of 2.69. It is also evident from this figure that the forward swept design has approximately 0.5% less peak efficiency potential. The forward swept design also has significantly more flow range compared to the baseline design. The *ADPAC* predicted spanwise distribution of pressure ratio and efficiency for the two designs are presented in Figure 4-9. This figure shows the redesigned rotor to have a slightly more hub-strong pressure ratio gradient than the baseline. It is also evident that the baseline rotor has slightly higher efficiency over most of the span, likely caused by the baseline's lower solidity.

The improved stall margin is partially a result of the passage shock being located further from the leading edge at design pressure ratio for the forward swept design as illustrated in the near tip contour plots of Figure 4-10. The increased stall margin and flow range is also attributed to the redesigned blade unstarting from hub to tip rather than tip to hub for the baseline design. This is illustrated in Figure 4-11 which shows static pressure contours on the pressure surface for incremental increases in back pressure for the two designs. For the baseline design the stronger tip shock reaches the leading edge before the weaker lower span shock causing the blade row to unstart and stall. As the back pressure is increased for the forward swept rotor the shock reaches the leading edge at the lower spans first. The shock at the lower spans is not strong enough to unstart the rest of the blade allowing it to go to higher pressure ratios.

It is typical for conventionally designed blades for the suction surface boundary layer to have a strong radial flow direction downstream of the passage shock location as illustrated in the particle trace of Figure 4-12. This boundary layer

Stack Axis Lean
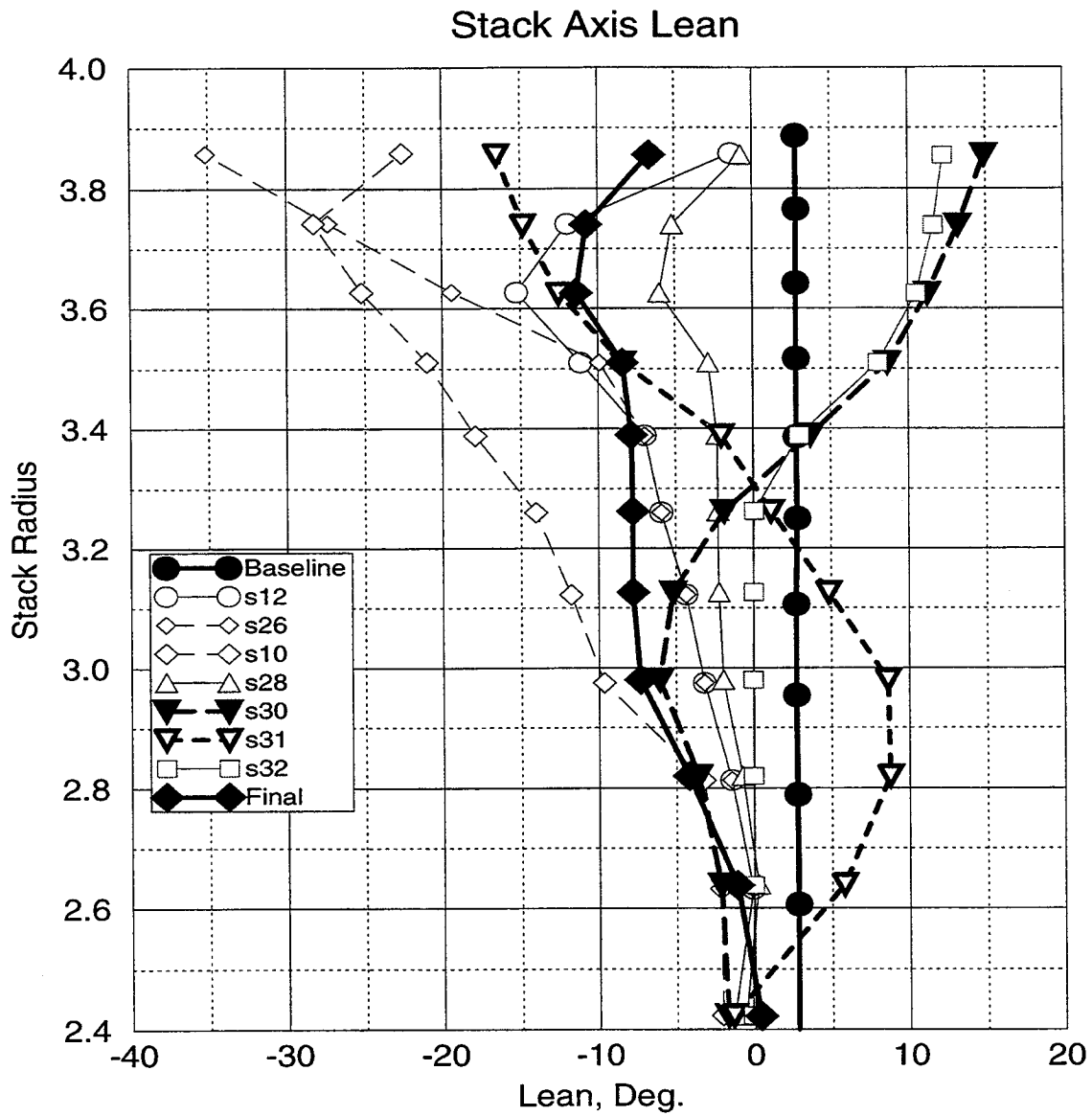
Figure 4-6 Tangential lean angles of several design iterations.

Figure 4-7. Final geometry of the forwrad swept rotor design.
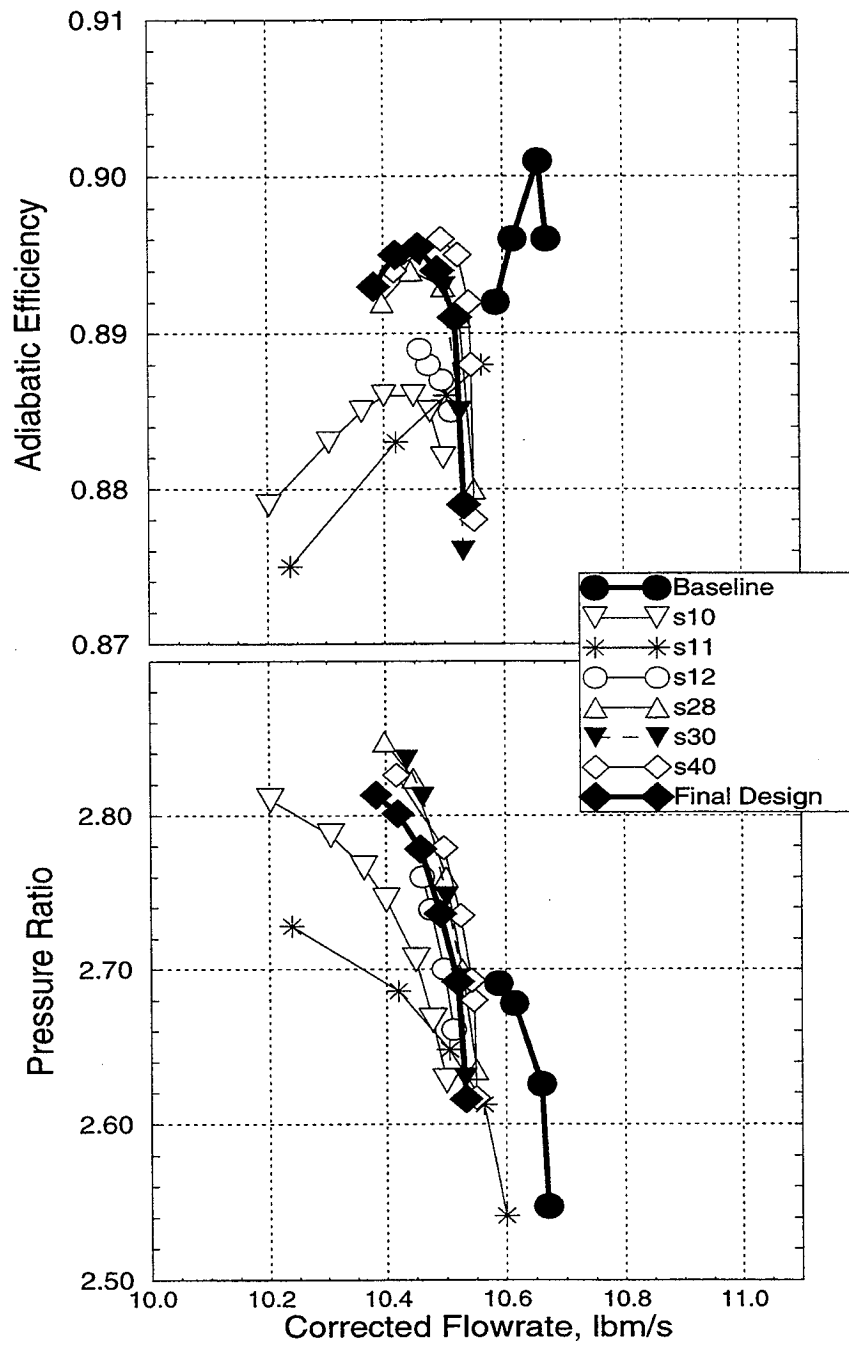
Figure 4-8 ADPAC predicted design speedline performance of several design iterations.
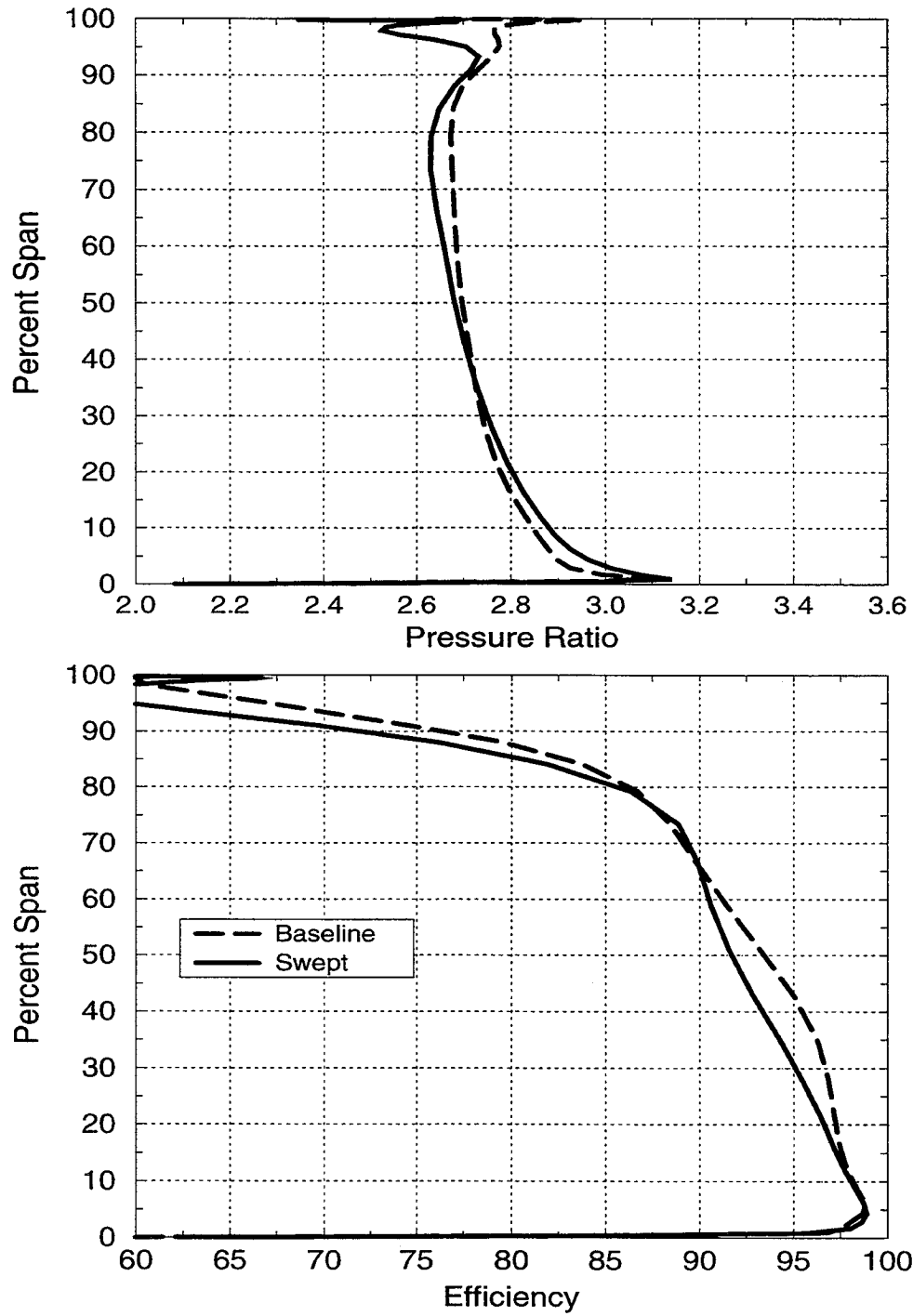
Figure 4-9 ADPAC predicted rotor pressure ratio and efficiency profiles.

Static Pressure Contours

Baseline Blade

Forward Swept Blade
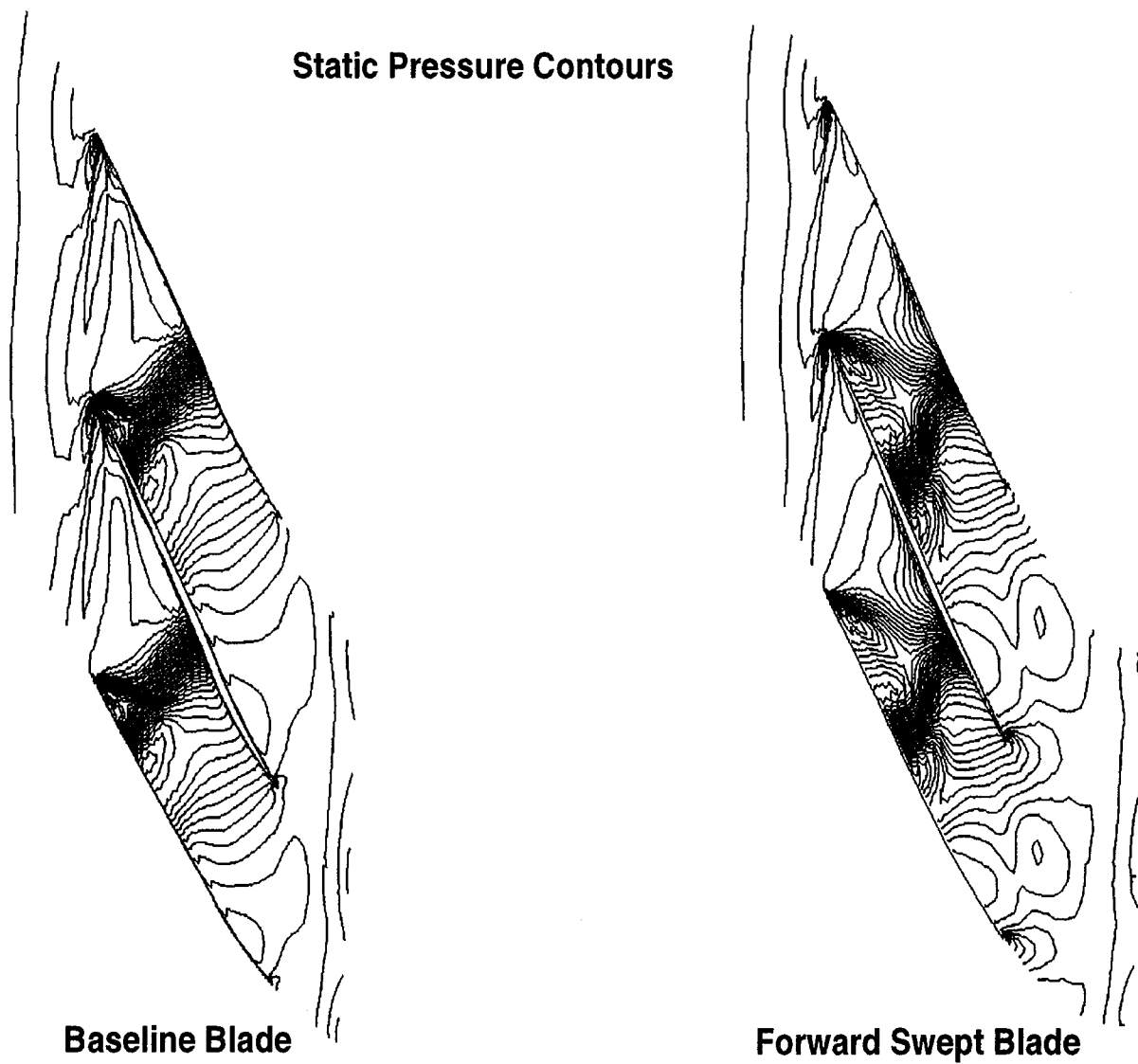
Figure 4–10. Comparison of ADPAC predicted static pressure contours near the tip of the baseline and forward swept rotors at the design pressure ratio.

Baseline Rotor Pressure Surface

Pr = 2.64   Pr = 2.68   Pr = 2.73
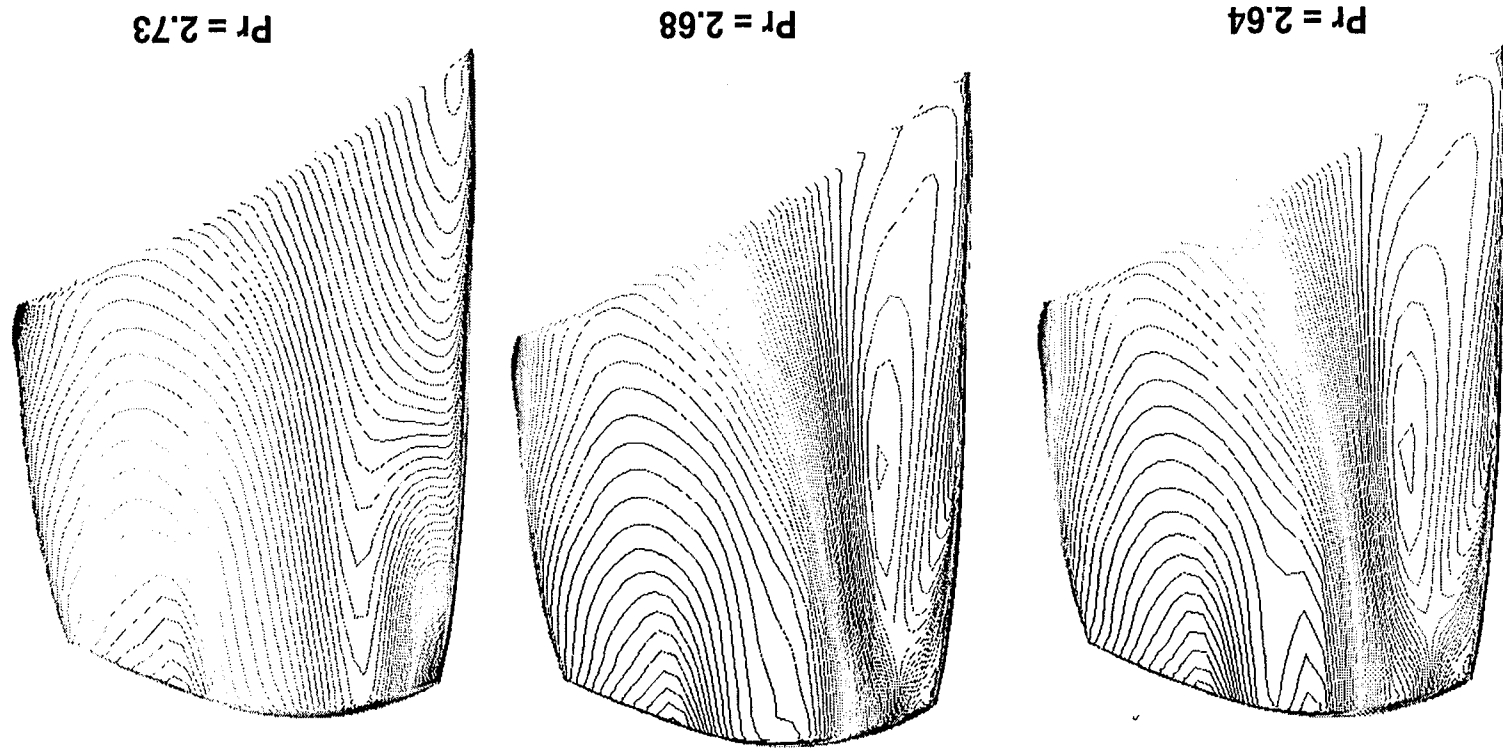
Figure 4-11a. Baseline rotor pressure surface predicted static pressure contours
at increasing pressure ratios.

80

Forward Swept Rotor
Pressure Surface
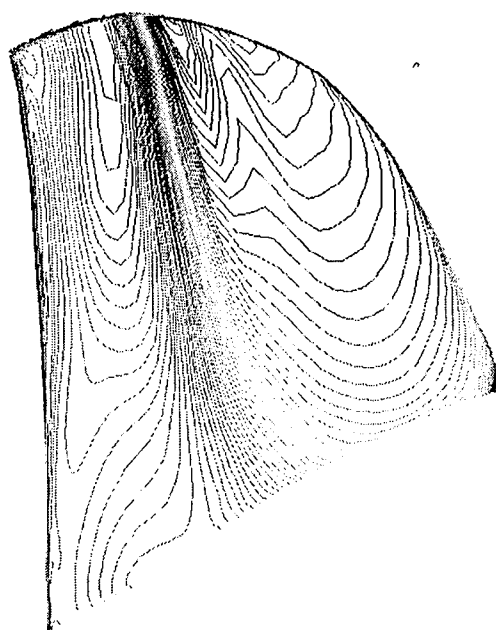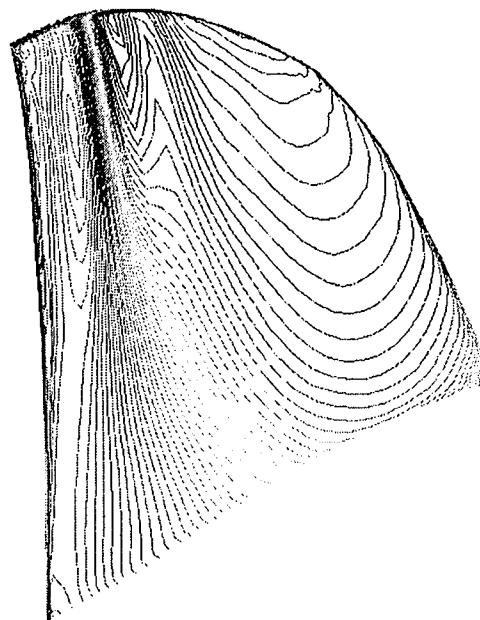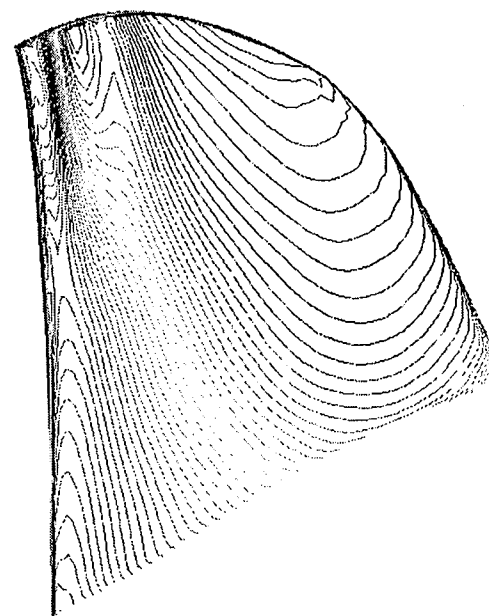
Pr = 2.62   Pr = 2.70   Pr = 2.83

Figure 4–11b. Forward swept rotor pressure surface predicted static pressure contours at increasing pressure ratios.

81

SUCTION SURFACE PARTICLE TRACE

Separated B.L.

BASELINE ROTOR

FORWARD SWEPT ROTOR
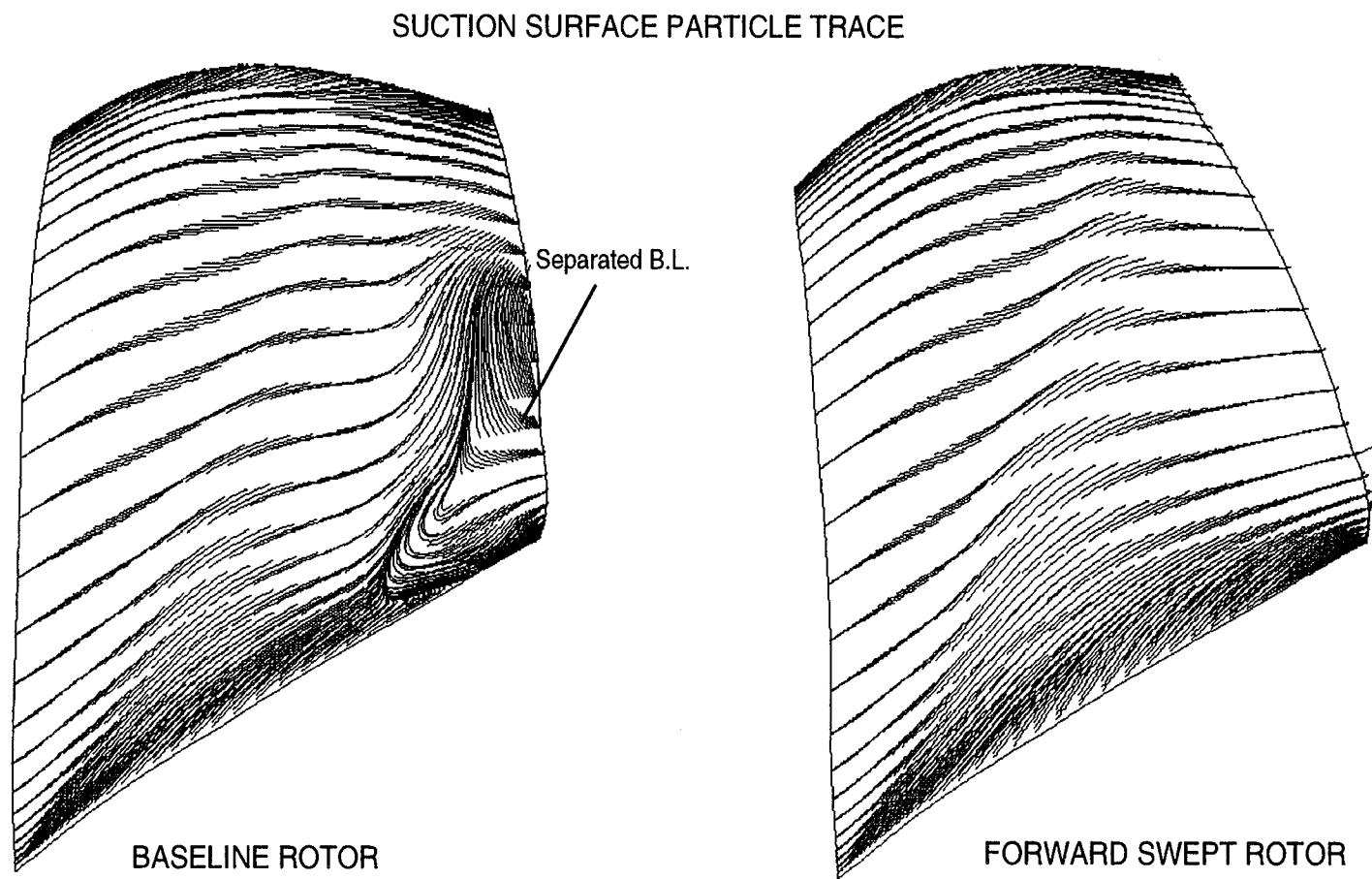
Figure 4–12. ADPAC predicted suction surface particle trace for baseline and forward swept rotors.

flow tends to collect near the tip creating blockage that back pressures the rotor tip streamlines. This flow pattern shown in Figure 4-12 for the baseline design is not observed for a forward swept design. For the forward swept design two things occur, the radial boundary layer flow runs off the trailing edge before it has an opportunity to travel very far and the shock strength at lower spans appears to be weakened by the forward sweep due to the more oblique shock. These characteristics also contribute to the higher stall margin achieved by the forward swept design.

4.2 Structural Analysis

The forward swept rotor was designed to meet structural integrity requirements consistent with safe rig operation and does not meet engine criteria for full life, LCF, birdstrike, etc. The design life requirement was 1000 hours and 1000 cycles consistent with the rest of the rig hardware. For HCF life, the allowable steady state stress levels were determined by the modified Goodman diagram of Figure 4-13 assuming a vibratory stress level of ± 10ksi. The $Ti_{6\text{-}2\text{-}4\text{-}6}$ material properties were obtained from test specimens cut from a forging from the same lot as the forging used to fabricate this rotor. A summary of the allowable stress levels is listed in Table 4-2. The design conditions for this analysis assumes standard day inlet with a steady state rpm of 49,000.

Several design iterations were required to find a tangential lean that would satisfy both the aerodynamics and steady stress requirements. The final results from the finite element analysis are provided as contour plots of uniaxial equivalent stress in Figure 4-14 for both surfaces of the airfoil. These plots and the summary in Table 4-2 show that the airfoil meets all allowable stress criteria. It should be noted that the stress levels for the forward swept rotor are much higher than the peak stress of 70 ksi for the baseline design.
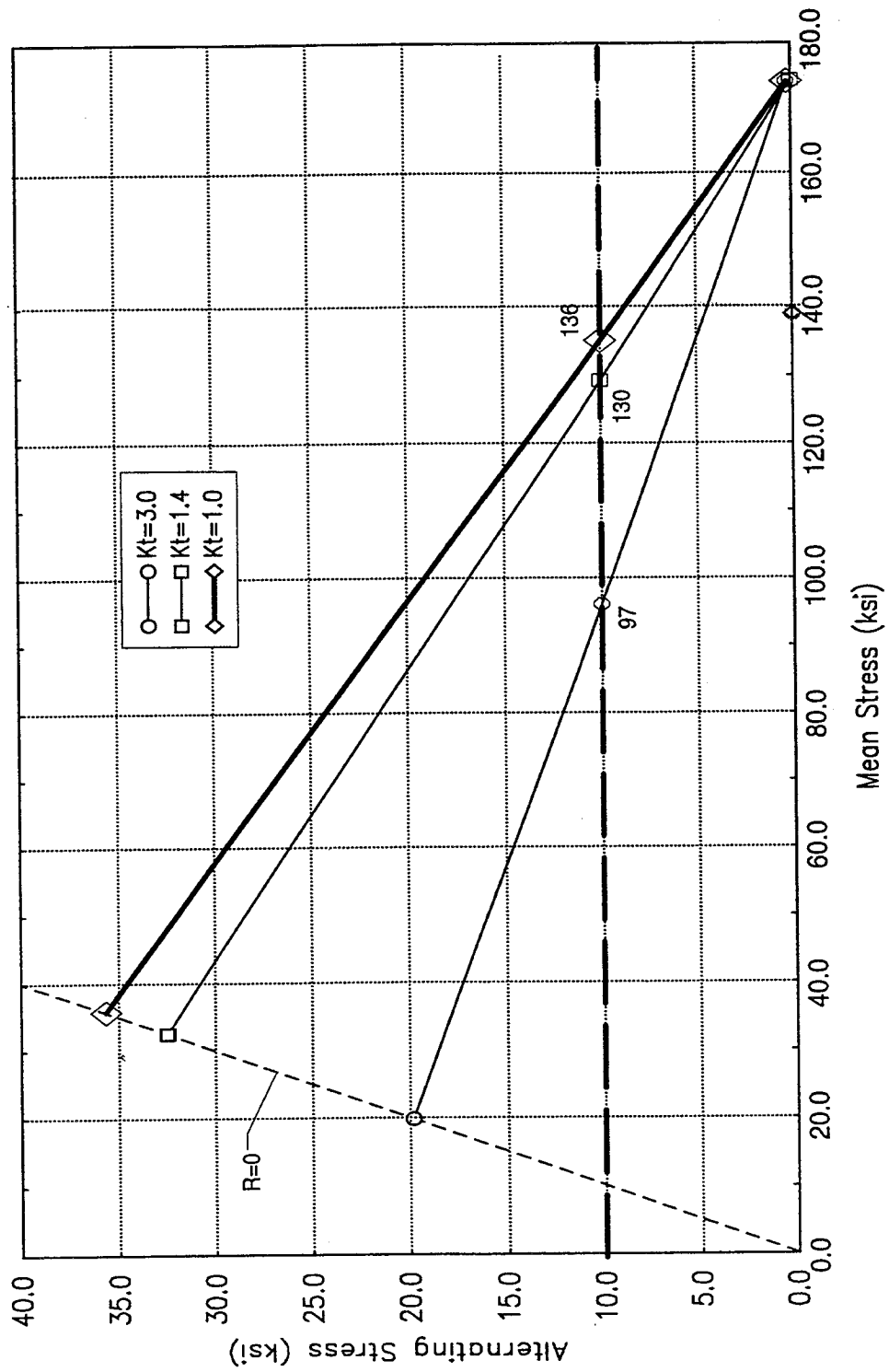
Figure 4-13. Modified Goodman diagram for Ti 6-2-4-6 at 230° F.

84

Suction Side

Pressure Side
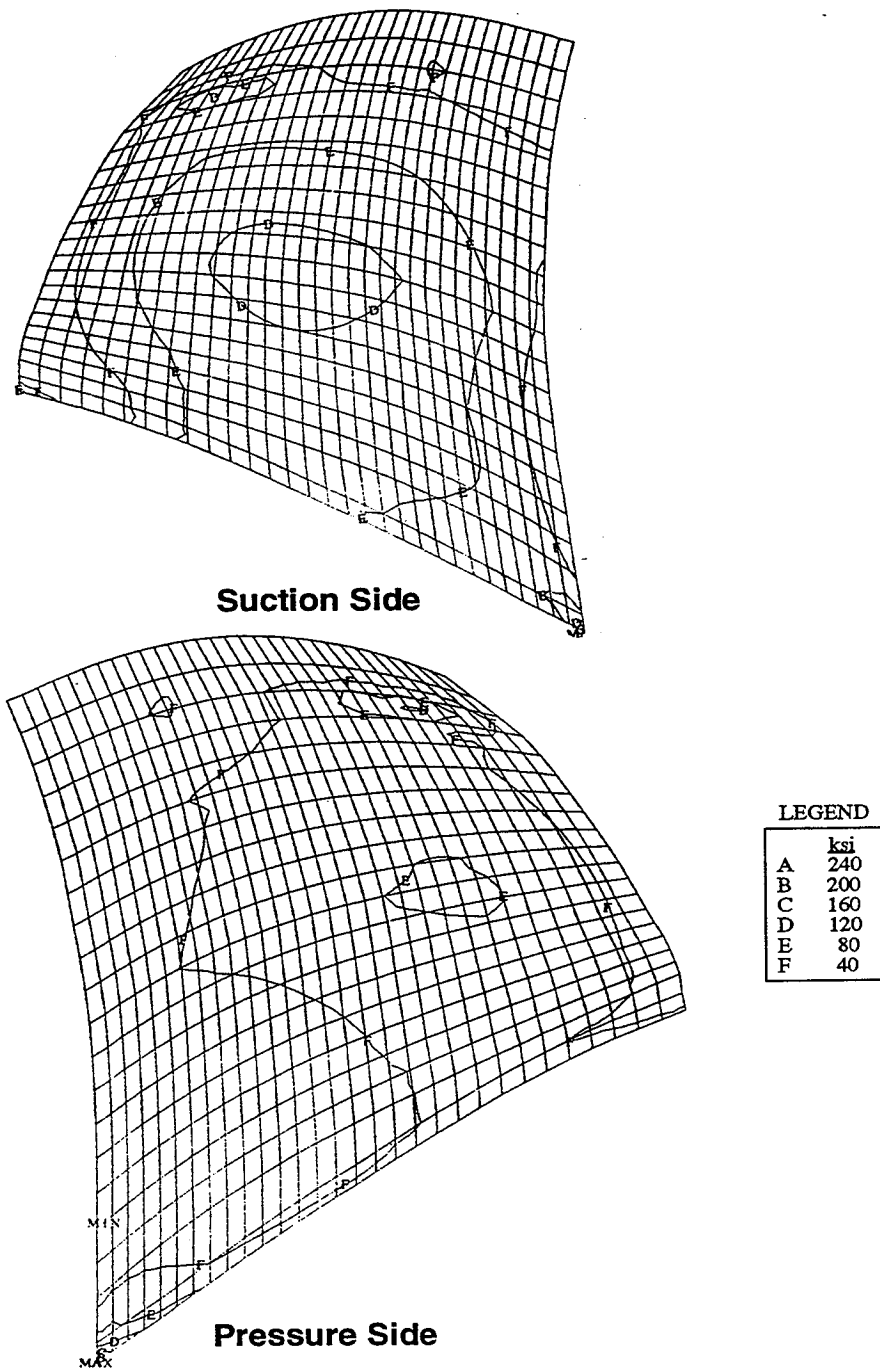
Figure 4-14. Calculated uniaxial equivalent stress for the forward swept rotor.

Table 4-2. Allowable steady stress levels to satisfy HCF criteria.

Location	Kt	Allowable Stress, ksi	Max Calculated Stress, ksi
Blade Surface	1.0	136	134
Filet Radius	1.4	130	114
Blade Edges	3.0	97	90

The structural analysis also showed that the static to hot running deflections for forward swept design are significantly different than the baseline design. The three- dimensional sweep of the redesigned blade causes it to deflect in a complex manner different from the baseline rotor as illustrated by the blade tip radial deflections shown in Figure 4-15. For the forward swept design the leading edge deflects 0.016 inches more than mid-chord and 0.006 inches more than the trailing edge requiring the blade tips to be machined to a contour in order to maintain tip clearance less than 0.005 inches along the entire chord.

These results indicate that this design is near the maximum forward sweep allowed and still have a structurally acceptable design to meet compressor rig test requirements. It should be mentioned that this design is not structurally acceptable for flight hardware and would require a significant reduction in forward sweep or much stronger material to meet flight worthy criteria.

4.3 Single Stage Test results

The forward swept rotor was installed in the single stage rig discussed in section 2.2.4 and tested in the NASA Lewis Research Center small compressor test facility. The cross-section of the test rig is illustrated in Figure 4-16. Note that the inlet guide vanes were removed to prevent interference with the forward swept rotor. The aerodynamic instrumentation was the same as that used in the baseline test described in Section 2.2.2.

Figure 4-15. Forward swept blade tip deflections .

Figure 4-16. Cross-section of single stage rig with forward swept rotor installed.

88

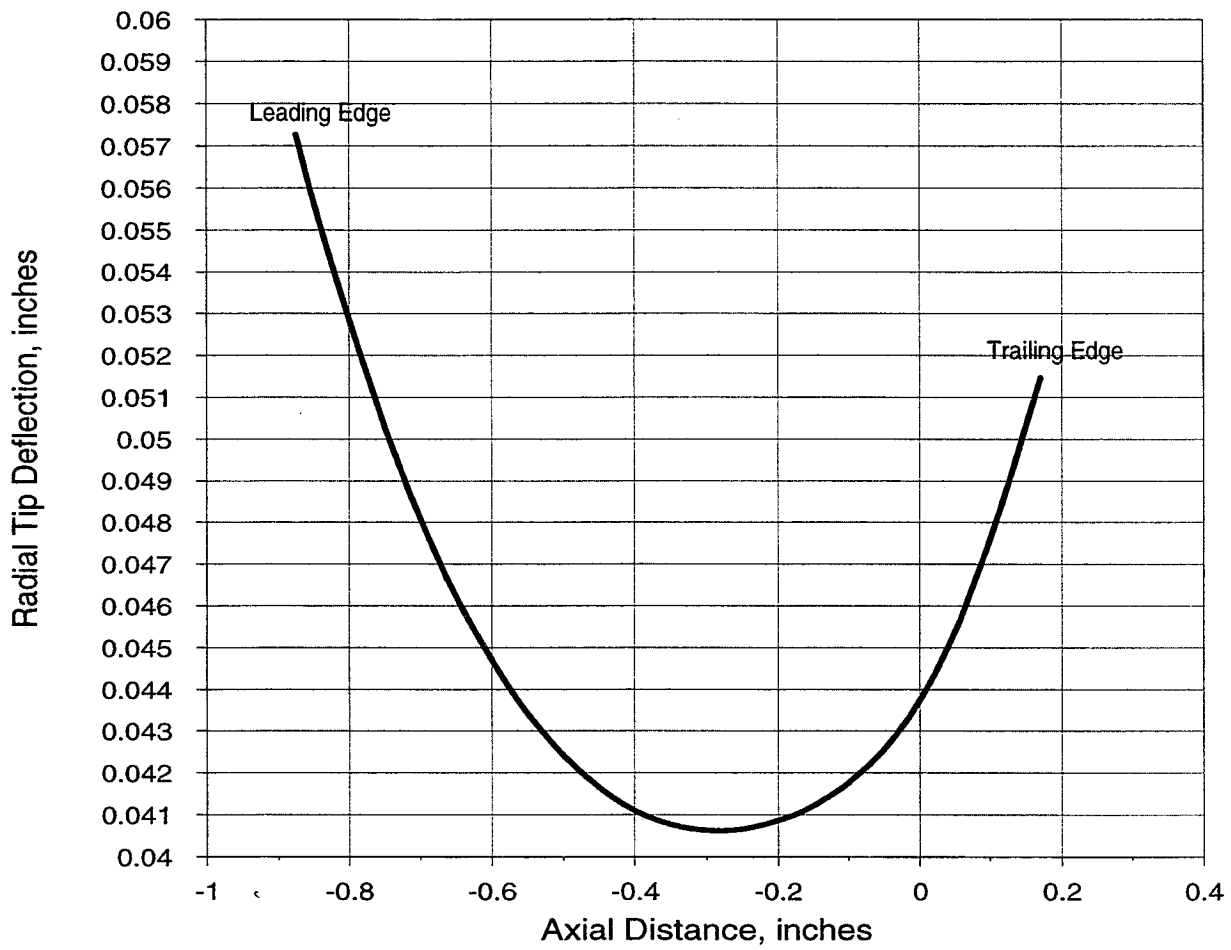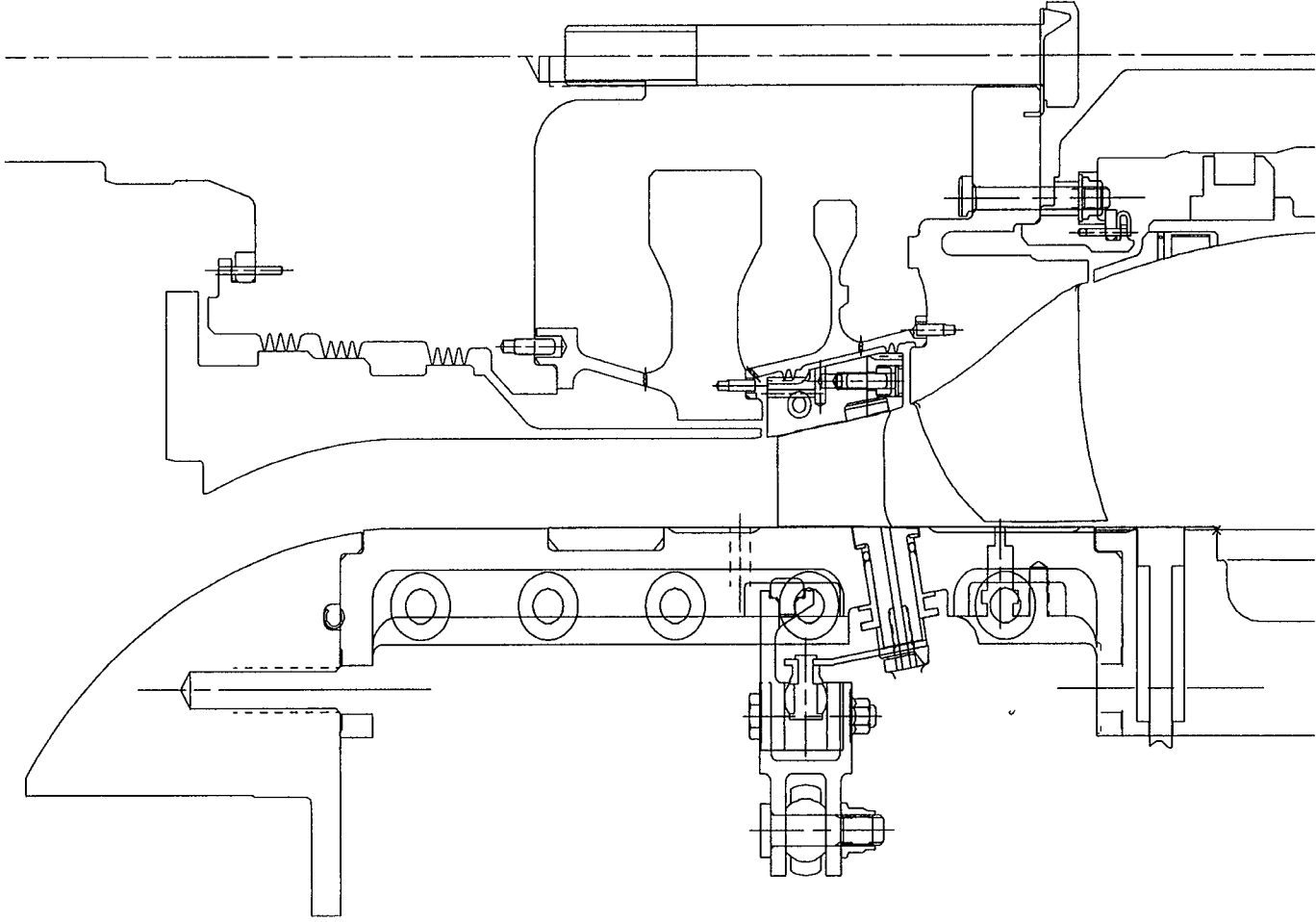The stage was mapped from open throttle to stall at speeds ranging from 70% to 100% in 5% increments. The primary objective of this test was to determine the forward swept rotor performance and to compare it to the baseline rotor performance. The stator performance was measured with a traversing wake rake and will not be discussed in detail.

The rotor only test map comparing both designs is presented in Figure 4-17 which reveals the substantial performance improvement for the forward swept rotor. Figure 4-17a shows both designs had a 100% design speed choke flow of 10.77 lbm/sec compared to the design intent of 10.63 lbm/sec. This figure also shows the forward swept design has much more constant speed stall margin than the baseline design as predicted by *ADPAC*. The forward swept design had nearly 20% stall margin from design pressure ratio compared to 9.2% for the baseline rotor. The increased stall margin is due to both increased pressure rise capability and the additional flow range. This increased flow range is a result of the shock spilling sequence of the forward swept rotor as discussed in Section 4.1.

The measured rotor adiabatic efficiency map of Figure 4-17b shows the forward swept rotor to have substantially higher efficiency (3-4%) below 98% speed and the same peak efficiency at 100% speed. This figure clearly shows the difference in shock starting characteristics between the two designs. It is evident that the baseline rotor does not become fully started until 98% speed where the efficiency jumps 3.5% from 95% to 98% speed. The forward swept rotor on the other hand, has less than a 1.0% efficiency increase between 85% and 90% speed indicating an earlier and more gentle starting characteristic. A summary of the 100% speed measured performance for both rotor designs is compared to ADPAC predictions in Table 4-3. The measured peak adiabatic efficiency is 89.2% for both rotors occurring at 95% speed for the forward swept rotor and 98.6% speed for the baseline design.

Table 4-3. Rotor only measured performance summary at 100% speed and design pressure ratio.

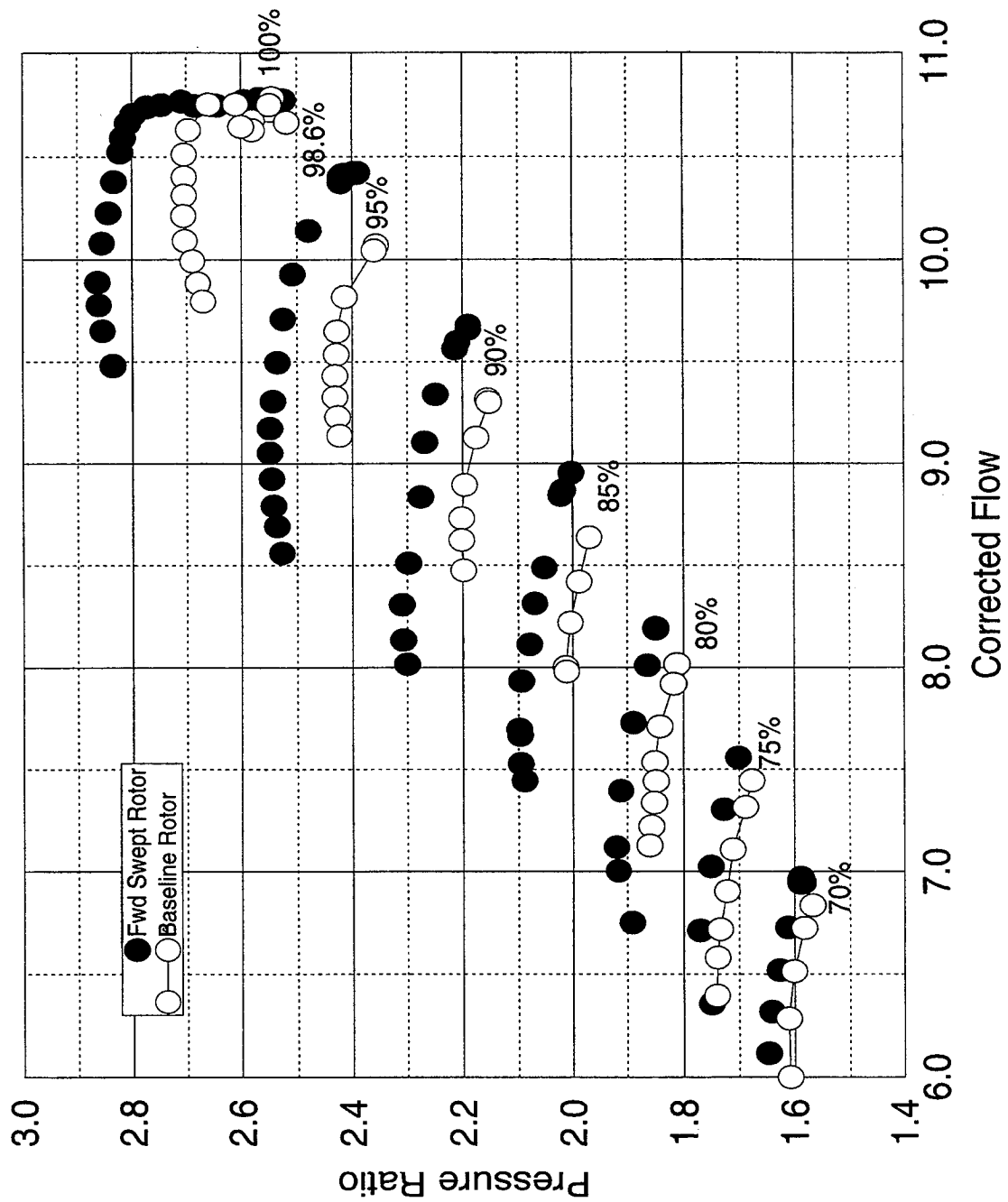| | Forward Swept | | Baseline | |
	ADPAC	Test	*ADPAC*	Test
Flow Rate, lbm/s	10.52	10.77	10.59	10.77
Pressure Ratio	2.69	2.69	2.69	2.69
Adia. Efficiency, %	89.1	87.5	89.2	87.0
Stall Margin, %		19.5		9.2

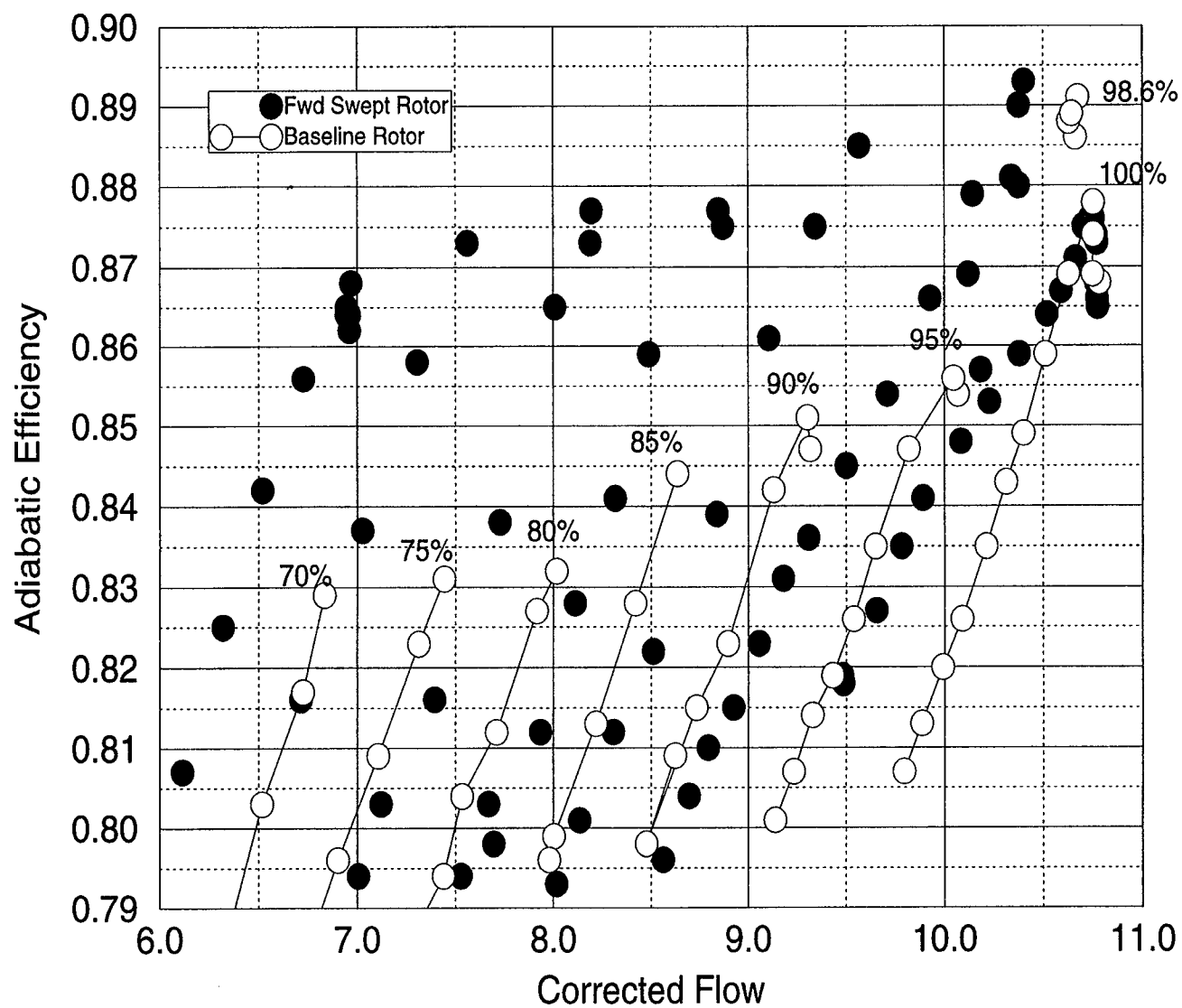Figure 4-17a. Measured rotor map for baseline and forward swept rotors.

Figure 4-17b. Measured rotor efficiency map for baseline and forward swept rotors.

The measured and *ADPAC* predicted radial profiles of pressure ratio are compared in Figure 4-18. This figure shows that the predictions are in good agreement with the measured data for both designs and that *ADPAC* predicted the slight increase in hub strong gradient for the forward swept design. The efficiency profile comparison in Figure 4-18 is also in good agreement and indicates the lower measured efficiency occurs primarily outside the 10% and 70% span locations.

Figure 4-19 shows the measured total pressure ratio profiles at 100% speed for the two rotor designs while throttling from a low operating line to near stall. The improved pressure rise capability of the forward swept design is evident in Figure 4-19a as it shows much higher pressure ratios are achieved at all spans as it approaches stall. The baseline design on the other hand, begins to stall at a pressure ratio slightly higher than the design value as illustrated in Figure 19b. It is interesting to note that both designs have a near stall pressure ratio that is less than their maximum values with the baseline stalling below the design pressure ratio.

In summary, the redesigned forward swept blade had substantially improved performance over the baseline design with double the design speed stall margin and up to 4% higher off-design efficiency. The high stress induced by the sweep is a major drawback with forward sweep that must be overcome before this technology can be transitioned to a product.
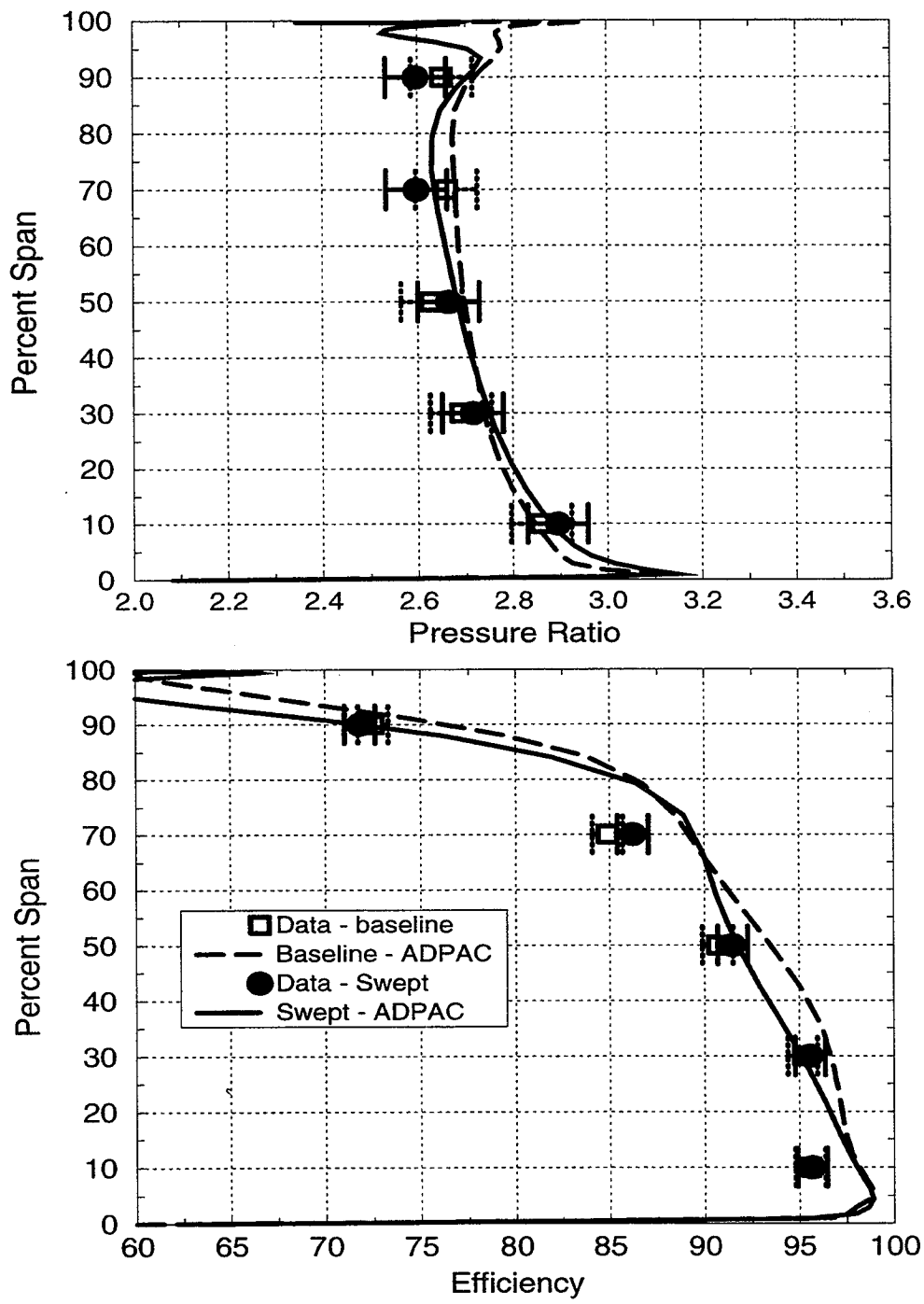
Figure 4-18 ADPAC predicted pressure ratio and efficiency compared to data.
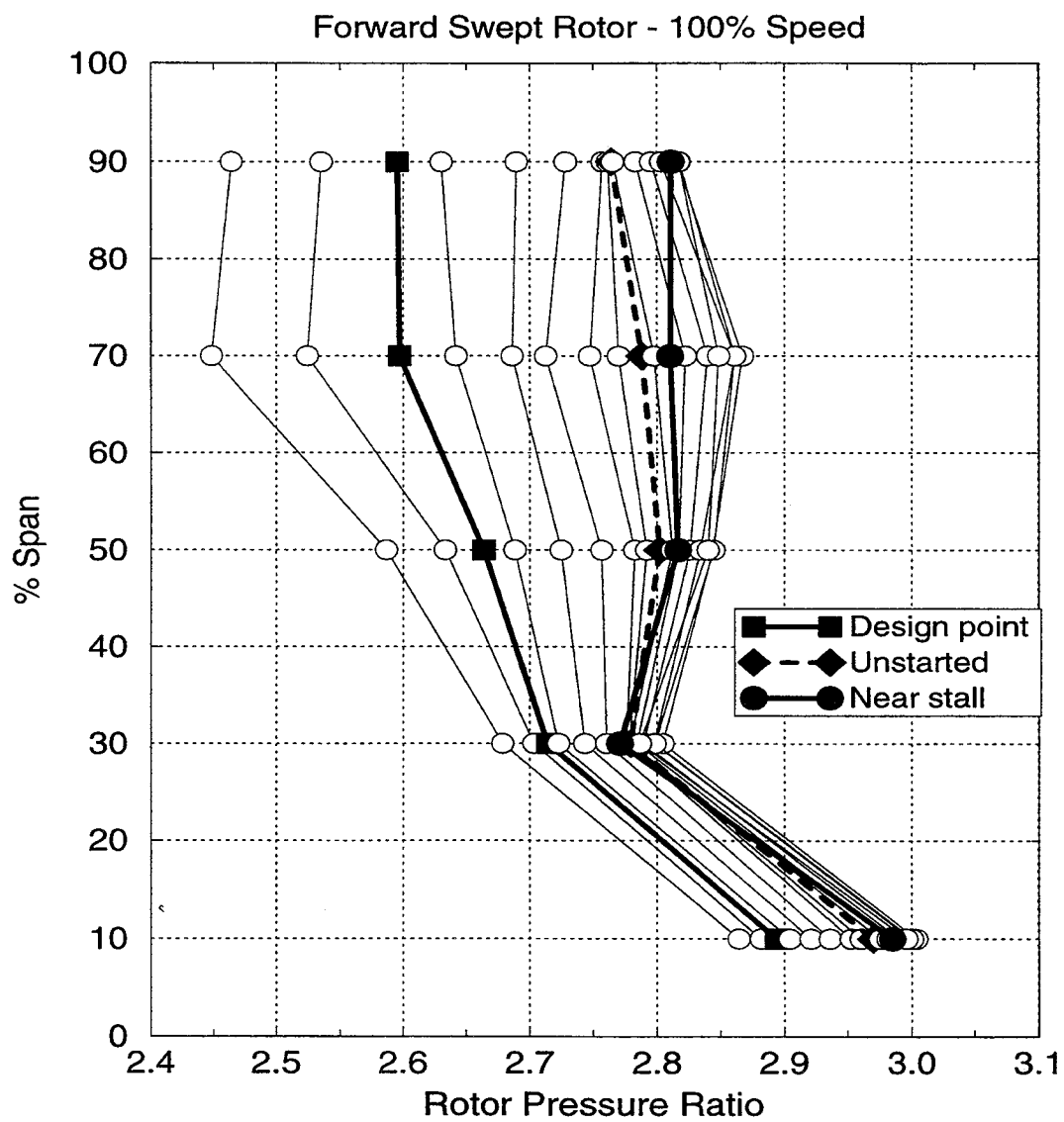
Figure 4-19a Forward swept rotor measured total pressure ratio profiles from open throttle to stall.
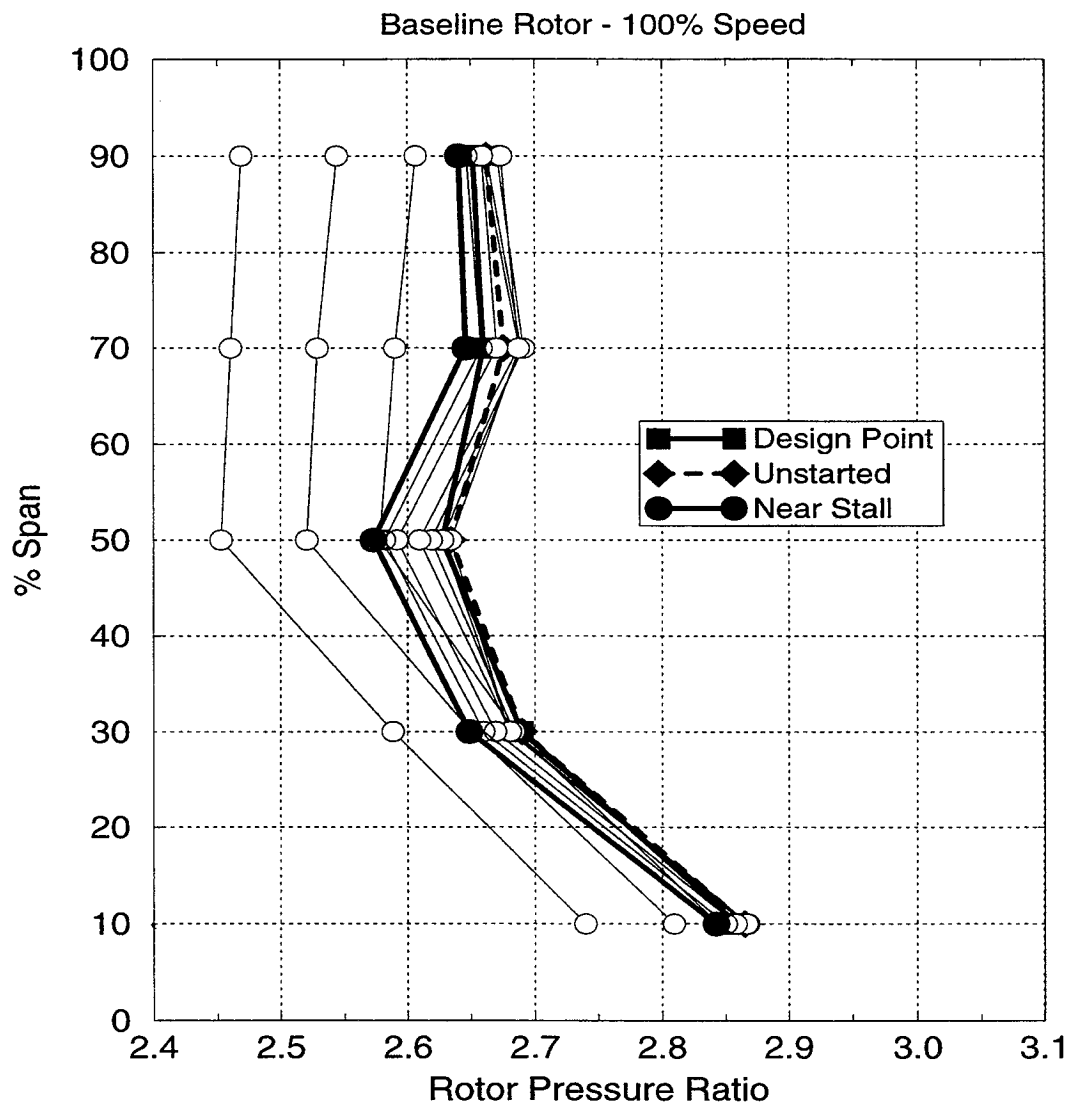
*Figure 4-19b Baseline rotor measured total pressure ratio profiles
from open throttle to stall.*

95

This Page Intentionally Left Blank

5.0 TANDEM VANE ASSESSMENT

Experimental data and numerical analysis results for the ASTC baseline compressor indicate that high loss is produced in the second stator row and that the stator may be partially stalled over a significant portion of the operating range. The poor performance of this vane contributes substantially to the lower than design efficiency of this compressor as reported in Chapter 2.0. This chapter investigates a tandem vane configuration as a concept to reduce losses and increase the vane row operating range. This concept has been studied and attempted previously with limited success, however, new 3D viscous analysis tools provide a better understanding of the complex flowfield allowing for potential design improvements of this concept.

5.1 Design and Analysis Methodology

The strong adverse pressure gradient in a highly loaded compressor vane can lead to strong separations and high losses. With the tandem vane concept the flow pattern in a high Mach number, high turning passage, the passage is split into two rows to reduce the diffusion to within acceptable limits. The tandem vane provides high solidity locally without introducing extra blockage in the inlet region. This concept is similar in nature to splitter vanes in centrifugal compressors.

Parametric trade studies of the tandem vane concept were conducted to determine the best configuration for both low design point loss and increased stall range. To reduce the number of design variables, a few design constraints were enforced. The first constraint was that the tandem vane configuration must have the same total axial length as the baseline vane so it may be installed into the existing rig. The second constraint fixed the chord of the first vane and the axial position of the tandem vane leading edge. These values were estimated from an earlier preliminary analysis and are not necessarily optimum values. A typical tandem vane configuration is presented in Figure 5-1 illustrating the design constraints and definitions.

The *ADPAC* code (Chapter 3) was used to analyze each design to determine its relative performance compared to the baseline design. The primary performance measurement used was total pressure loss at the design condition. Each tandem vane analysis was performed using the same two-block mesh defined in Figure 5-2.
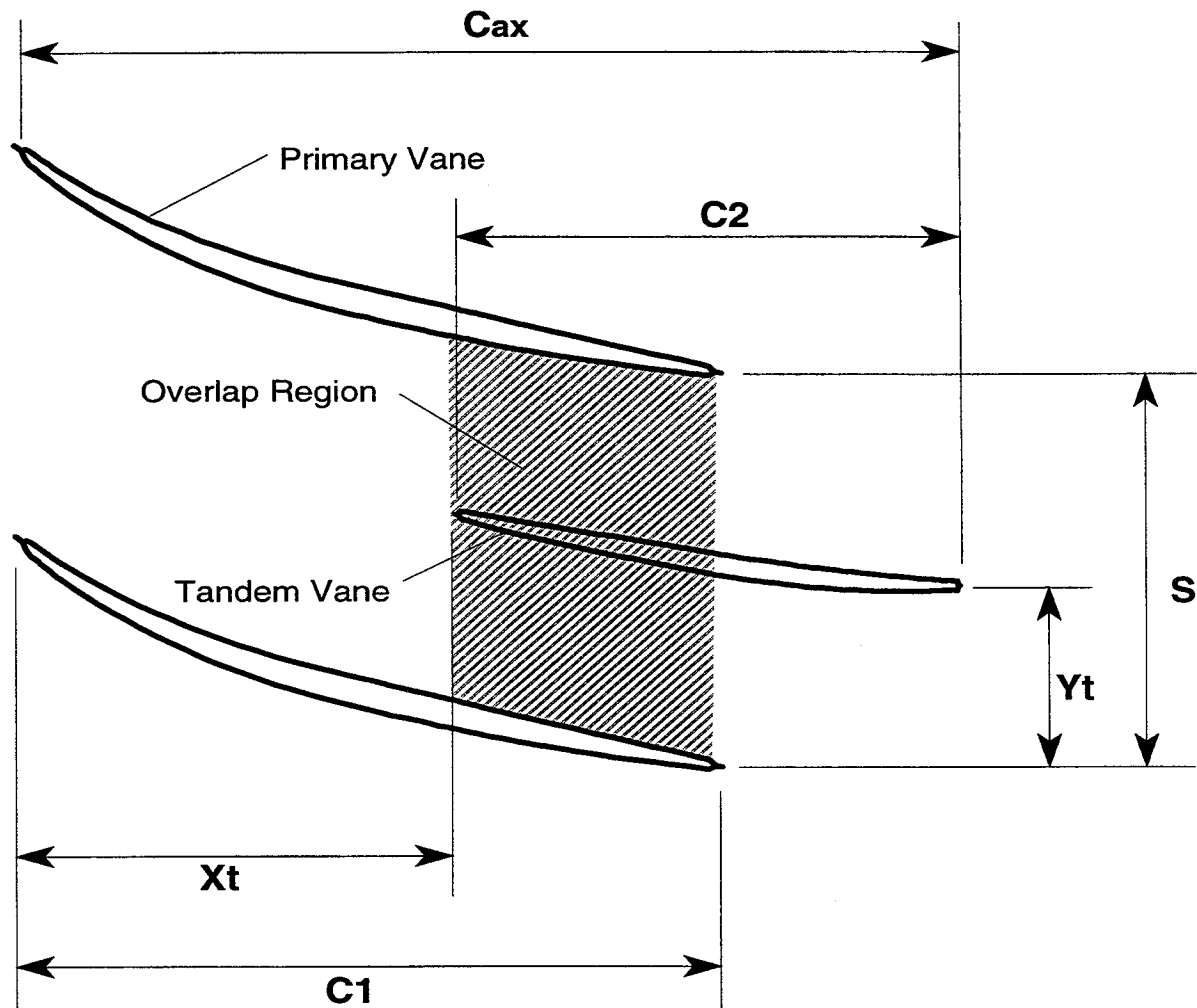
Tandem Vane Pitch Location, $Sp = \dfrac{Yt}{S}$

Tandem Vane Leading Location, $Tx = \dfrac{Xt}{C1}$ $= 0.626$ for all designs

Cax = Baseline design axial chord

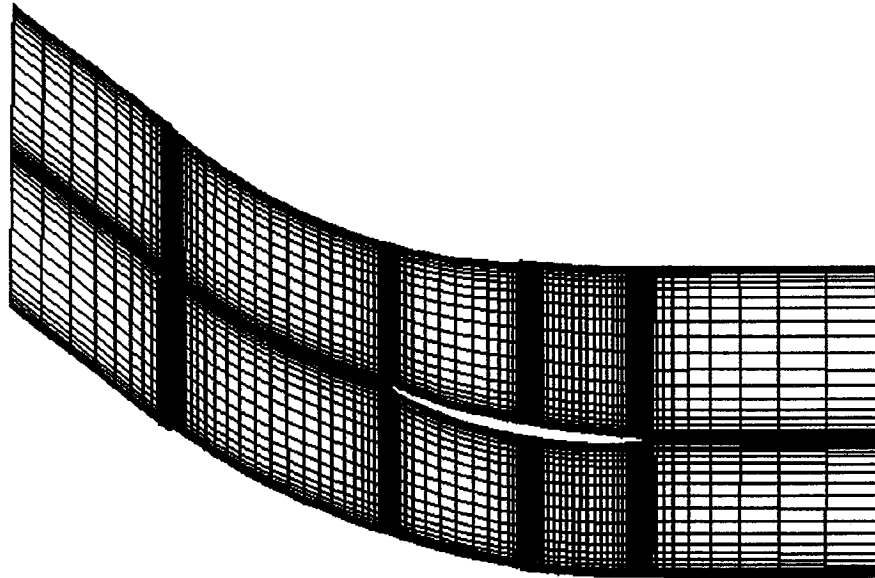Figure 5-1. Tandem vane configuration definitions.

Figure 5–2. Typical tandem vane ADPAC two block mesh.

To minimize grid related differences, the baseline vane was also analyzed using a similar two-block mesh.

The inlet profiles to the tandem vane were obtained from a data match study conducted with data from the rig test corresponding to the compressor design point. The vane inlet profiles used as boundary conditions in *ADPAC* for total pressure, total temperature and flow angle are presented in Figure 5-3.

5.2 Parametric Trade Studies

The design parameters chosen for this investigation included the tandem vane pitchwise location, solidity and chordwise loading distribution. The results of these studies are provided in the following sections.

5.2.1 Tandem Vane Pitchwise Location

A parametric study on the influence of tangential spacing on the performance of the tandem vane configuration was conducted. This study consisted of four tandem vane designs with the pitchwise spacing, S_p, ranging from 0.40 to 0.70 as defined in Figure 5-1. Higher values of S_p position the tandem vane closer to the primary vane suction surface. All of these designs are illustrated in Figure 5-4. All tandem configurations have the same meanline solidity and axial chord as the baseline vane. The *ADPAC* predicted mass flow rate and total pressure loss is compared to the conventional design in Table 5-1.

Table 5-1. Tandem vane tangential spacing parametric study results.

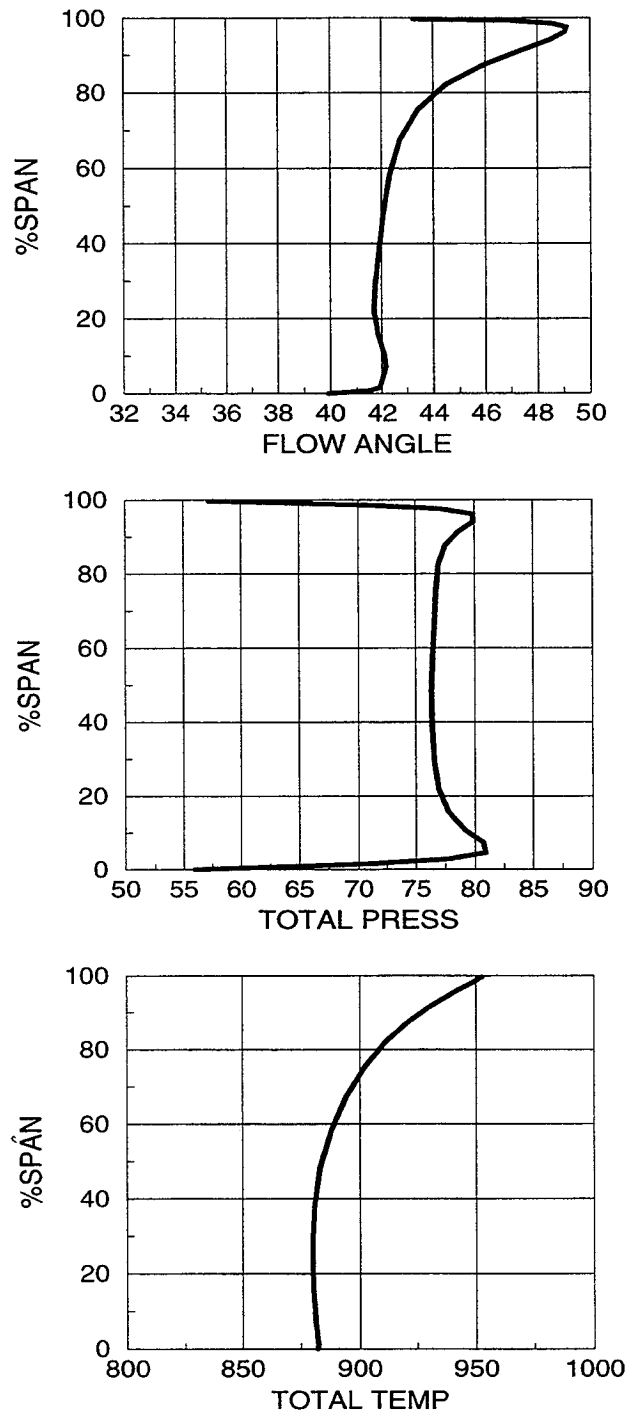| Design	S_p	Flow rate lbm/sec	$\Delta P_t/P_{tin}$
Baseline	NA	11.02	0.0199
T02	0.51	10.77	0.0253
T03	0.40	10.77	0.0254
T04	0.60	10.73	0.0262
T05	0.70	10.68	0.0268

Figure 5-3. Inlet profiles used in ADPAC analysis.
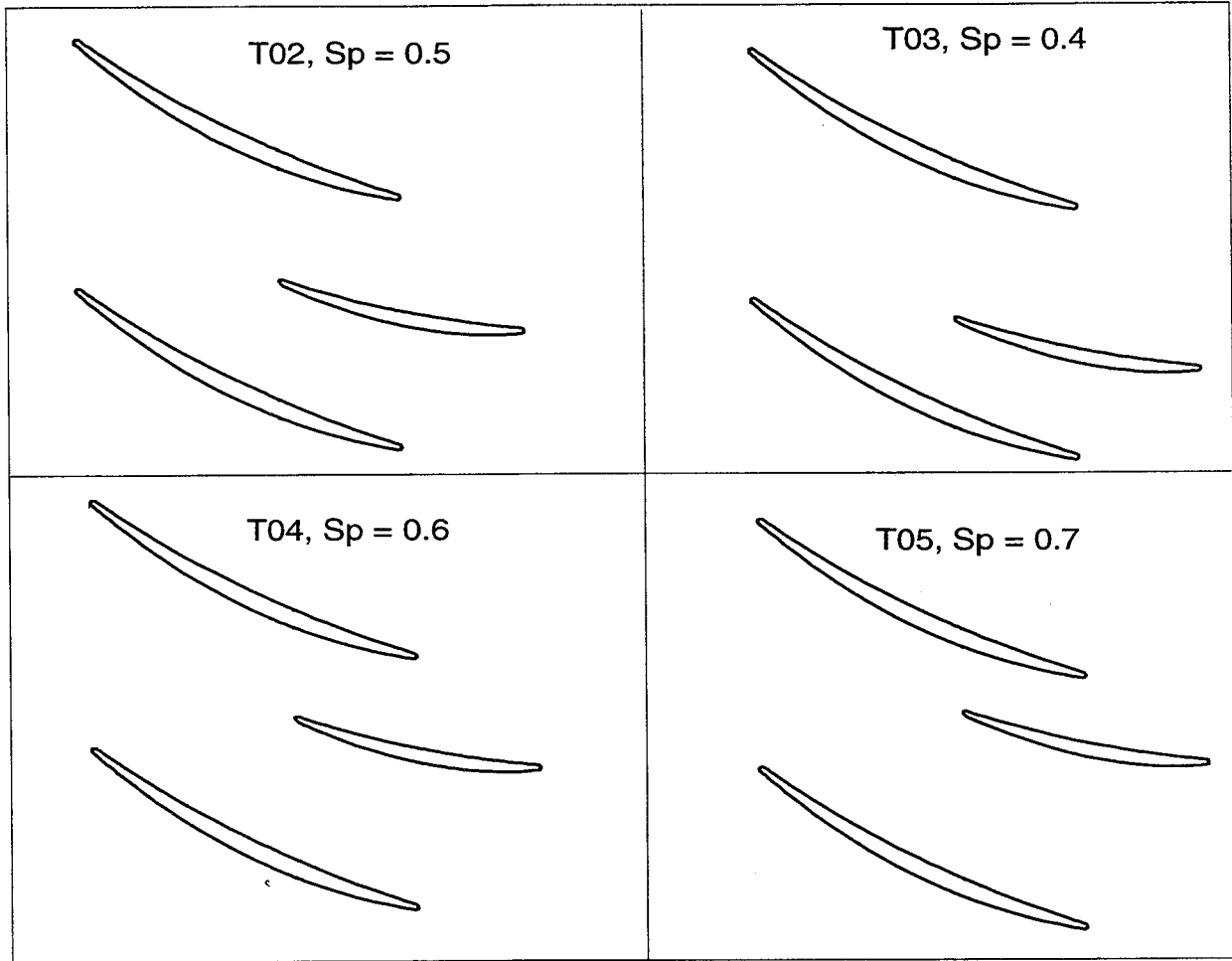
101

PITCHWISE LOCATION STUDY

Figure 5-4. Tandem vane geometries used for pitchwise location study.

The spanwise profiles of total pressure loss for all designs are shown in Figure 5-5 and the chordwise distribution of loss through the vanes are illustrated in Figure 5-6. These figures along with Table 5-1 indicate that the tangential placement of the tandem vane has very little impact on the vane row performance with all tandem vane designs having approximately 0.5% higher total pressure loss than the baseline vane. The mid-pitch design (T02) has only a slight advantage over the other tandem designs and will be used in the following trade studies. The chordwise distributions of loss in Figure 5-6 show the tandem designs to have lower loss in the inlet region due to lower solidity and that most of the additional loss is produced at the inlet to the tandem vane or second vane.

5.2.2 Solidity

The effect of solidity on vane loss was investigated by designing several tandem configurations with effective solidities ranging from 1.39 to 2.85. Where effective solidity is defined as:

$$\sigma_{eff} = \frac{C_1 + C_2}{S}$$

and,

C_1 = chord of primary vane
C_2 = chord of tandem vane
S = pitch of primary vane

The various solidities were achieved by changing the number of blades and holding the chord of each airfoil constant. The *ADPAC* predicted mass flow rate and total pressure loss is provided in Table 5-2 for each design. These results indicate that solidity also had a small impact on the mass-averaged total pressure loss with values ranging from 2.49% to 2.59%. However, in the case of the lowest solidity design (T08), the higher blade loading creates large airfoil surface boundary layers as seen in Figure 5-7 compared to a higher solidity design creating blockage and reducing it's flow capacity. It is interesting to note that an area-averaged total pressure loss greatly reduces the difference in loss between the baseline and tandem designs. This indicates that the baseline design is actually producing more blockage with less loss than the tandem design.
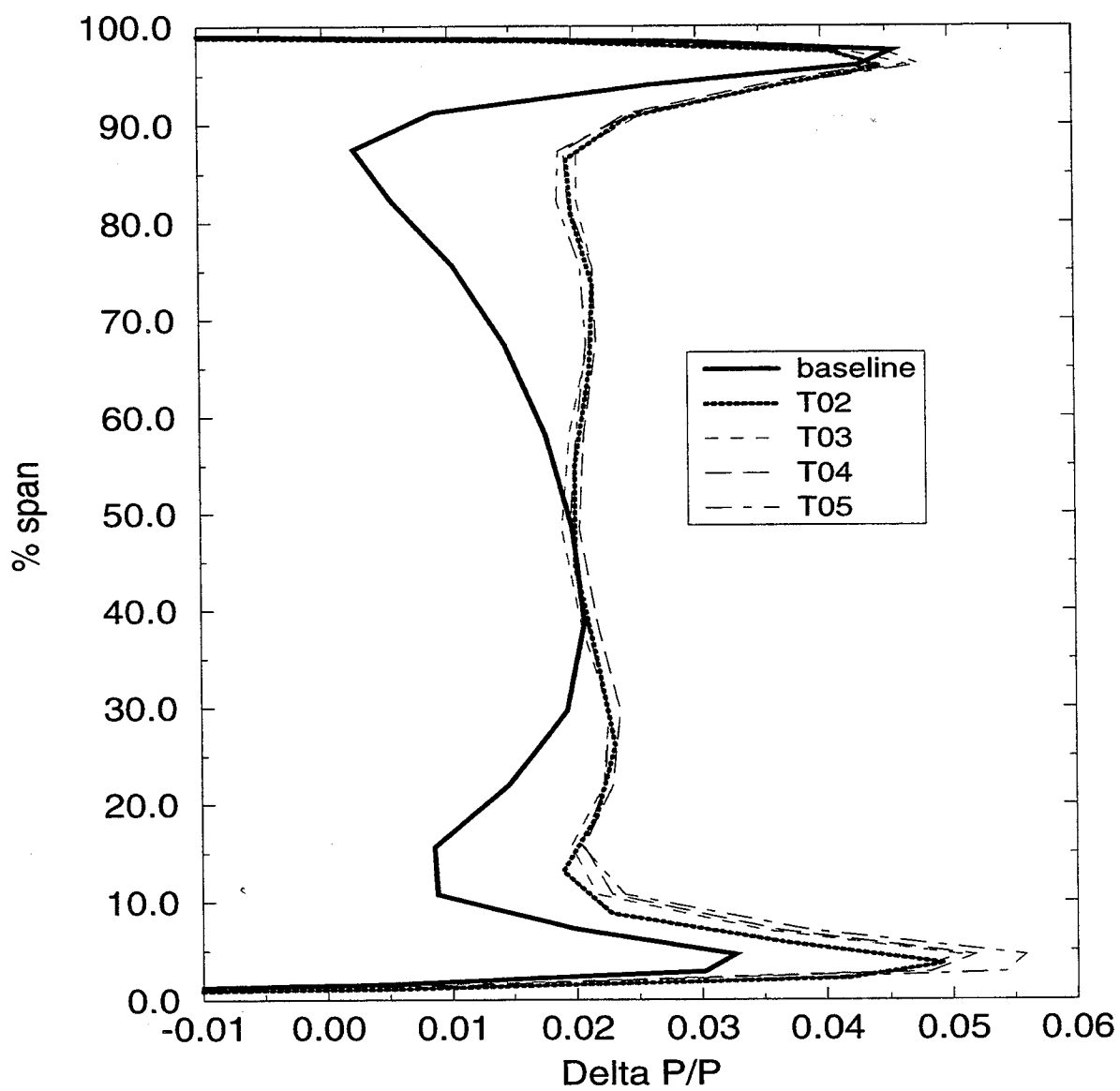
103

Figure 5-5. Predicted total pressure loss profile from pitchwise trade study.
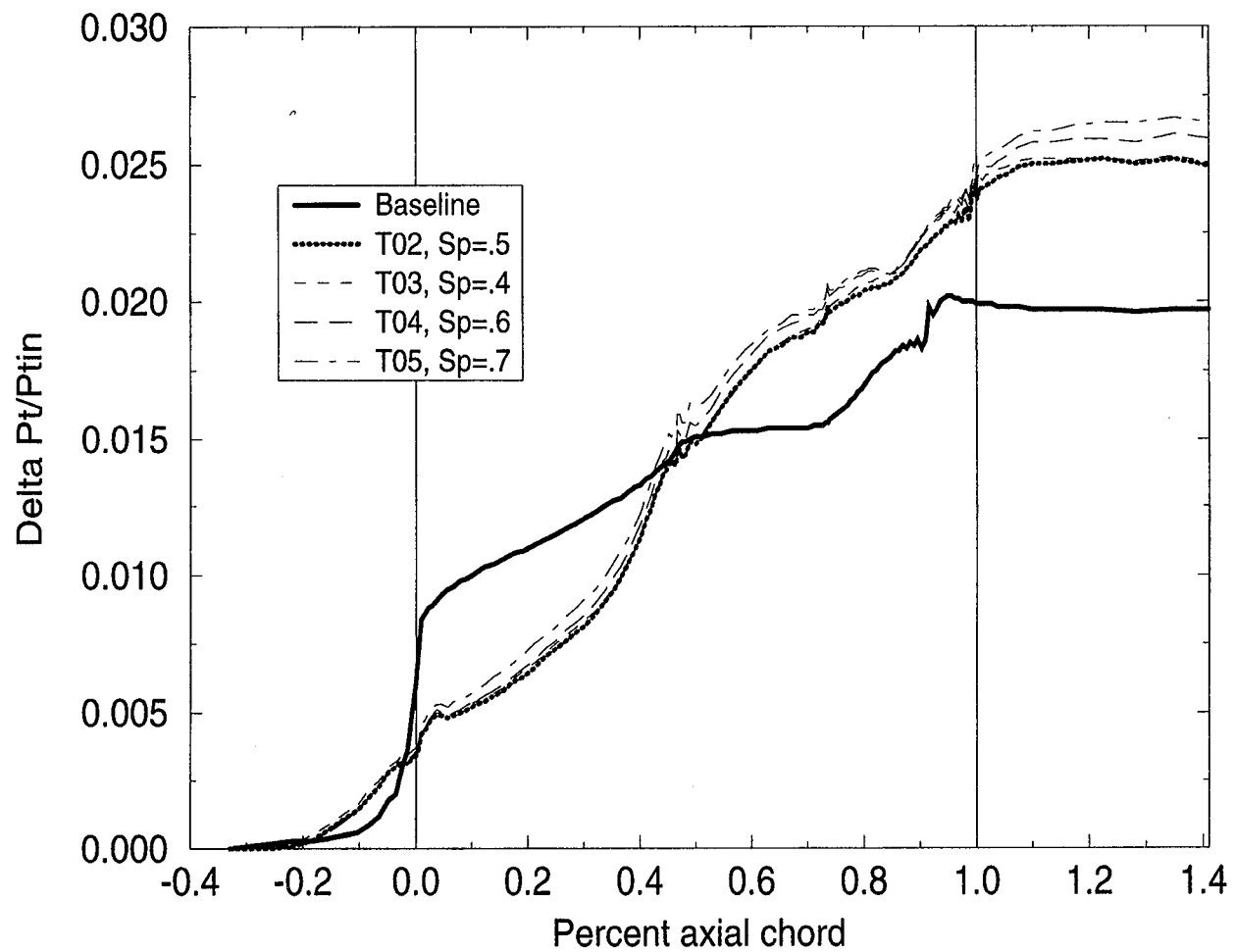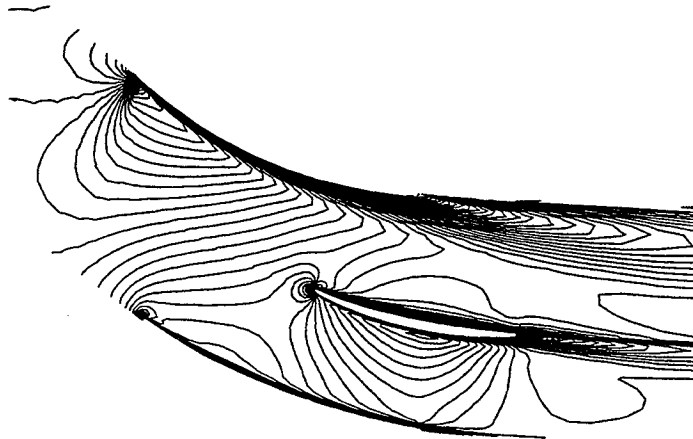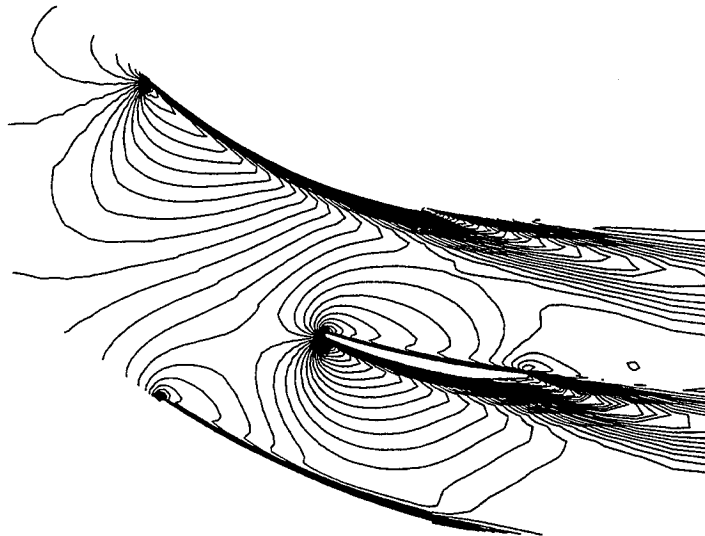
Figure 5-6. Predicted mass-averaged total pressure loss through the vane row.

Design T07, solidity = 1.85

Design T08, solidity = 1.39

Figure 5-7. Predicted Mach number contours for a high and low solidity design.

Table 5-2. Tandem vane solidity parametric study results.

Design	No. Vanes	Meanline Solidity	Wac lbm/sec	$\Delta P_t/P_{tin}$ mass ave.	area ave.
Baseline	60	2.19	11.02	0.0199	0.0272
T02	49	2.27	10.77	0.0249	0.0287
T06	44	2.04	10.76	0.0246	0.0285
T07	40	1.85	10.74	0.0246	0.0286
T08	30	1.39	10.59	0.0259	0.0307
T09	50	2.85	10.77	0.0257	0.0294

The tandem vane solidity has some impact on the turning ability of the vane row. Figure 5-8 shows that the higher solidity designs have lower exit flow angles by as much as 4 degrees. Each of the tandem designs had the same inlet flow angles and exit metal angle so a higher exit flow angle means less turning and higher deviation. This figure also shows that the baseline design has better turning capability than the tandem design with equivalent solidity (T02). This is a result of the locally low solidity at the trailing edge region of the tandem configuration as illustrated in Figure 5-1. This may be corrected by doing more of the turning in the high solidity overlap region.

5.2.3 Chordwise Loading Distribution

The next parametric study involved the investigation into the influence of the primary vane camber distribution on tandem configuration losses. Three tandem vane configurations were designed with different camber distributions that provided forward, aft, and evenly distributed primary vane loading levels. In addition, each design had higher turning in the primary vane than previous tandem designs as suggested in the previous section. The leading edge and trailing edge camber levels at 50% span for each design along with the predicted mass-averaged total pressure loss and mid-span exit flow angle are provided in Table 5-3. These results indicate that loading distribution had little impact on mass-averaged total pressure loss with the evenly loaded design having the lowest loss at 2.49% and the aft loaded design the highest with 2.77%. However, these higher loaded primary
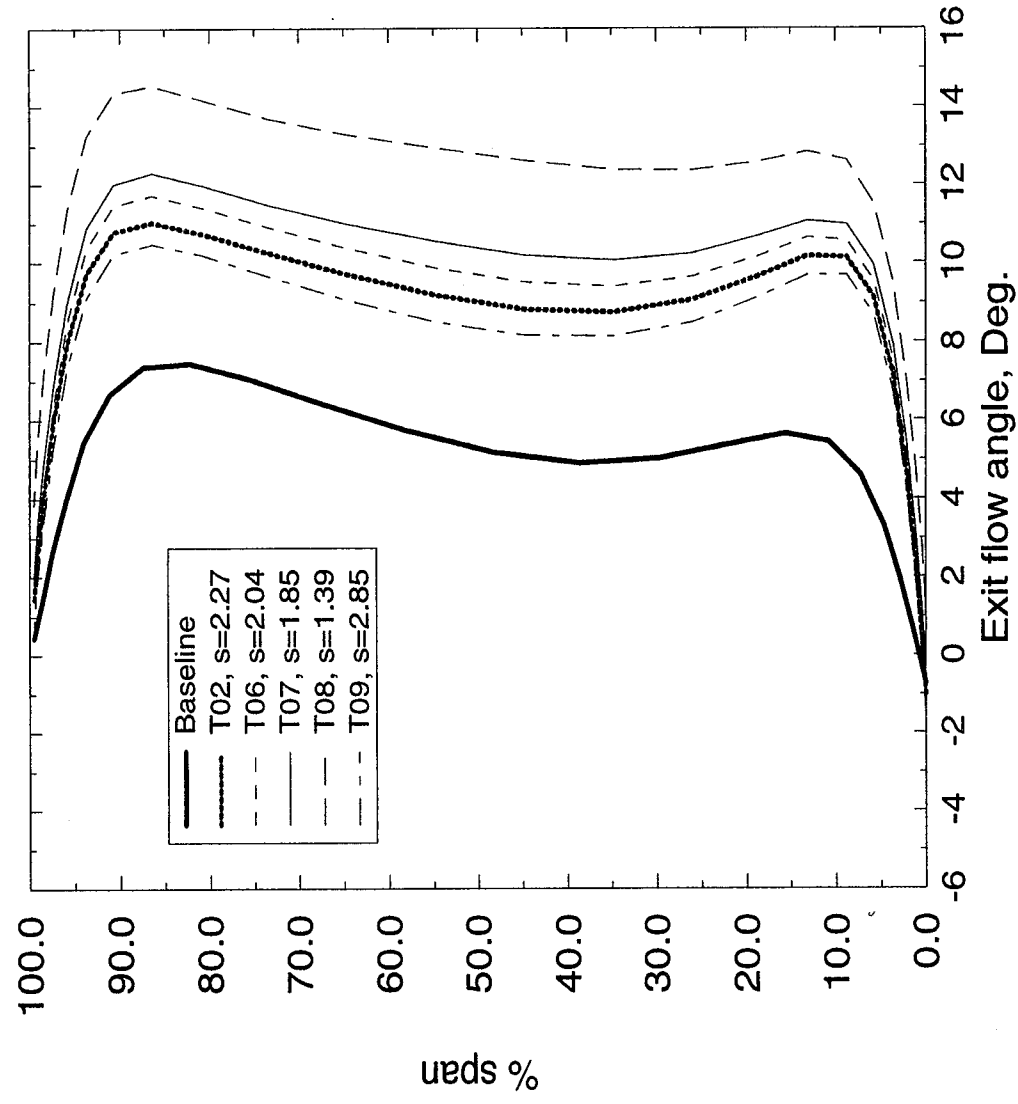
Figure 5-8. Predicted exit flow angle for various solidities.

vane designs had a positive effect on the total turning of the tandem vane configurations with exit flow angles equal to or less than the baseline design as presented in Table 5-3 and Figure 5-9. The chordwise loading distribution did have an influence on the amount of turning each design achieved as illustrated in Figure 5-9. The front loaded design (T17) had the highest level of turning and the evenly loaded design had the lowest level equal to that for the baseline vane. The differences in the exit flow angles is the result of differences in the vane surface boundary layer growth for each design. The front loaded design had a smaller boundary layer growth on the tandem vane causing it to have lower deviation angles and more turning.

Table 5-3. Tandem vane camber distribution results.

Design	Front Camber	Rear Camber	$\Delta P_t/P_{tin}$ mass ave.	Exit Flow Angle
Baseline	29.7	9.0	0.0199	6.0
T16	11.3	29.6	0.0277	4.3
T17	28.7	8.8	0.0261	3.0
T18	17.2	17.2	0.0249	6.0

The loading distribution effect on the blade surface pressure gradient is apparent from Figure 5-10. This Figure indicates that these designs are operating with high incidence on the tandem vane which is contributing to the higher loss in this region as illustrated in Figure 5-6. The tandem vane of configuration T18 was redesigned with higher inlet metal angles to reduce this incidence and the loss associated with it. The mid-span predicted blade loading plot for this design is provided in Figure 5-11 which shows the improved pressure distribution around the tandem vane. This resulted in a reduction in total pressure loss to 2.27% from 2.49%. The total pressure loss profiles for the new design (T20) and the T18 design are compared with the baseline design profiles in Figure 5-12.
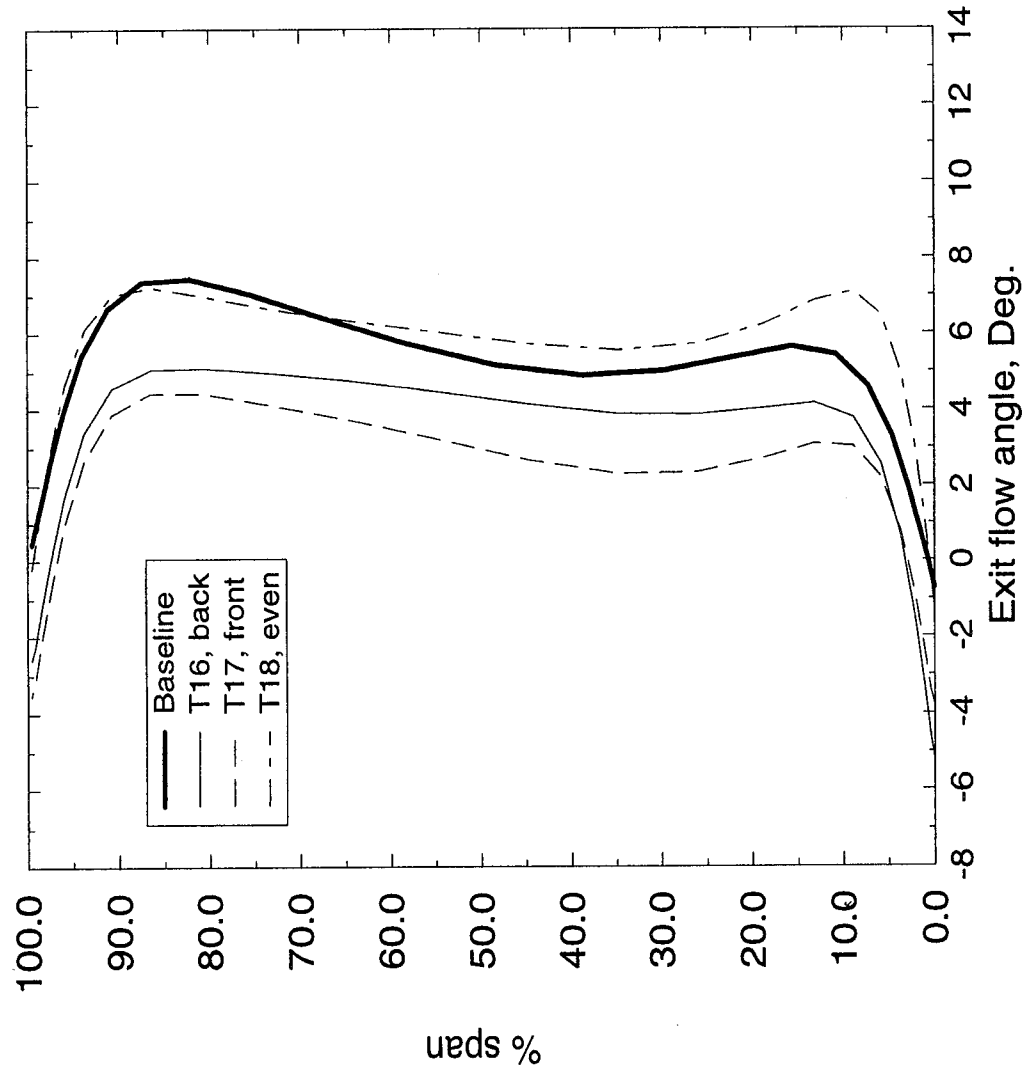
Figure 5-9. Predicted exit flow angle of various loading distribution designs.
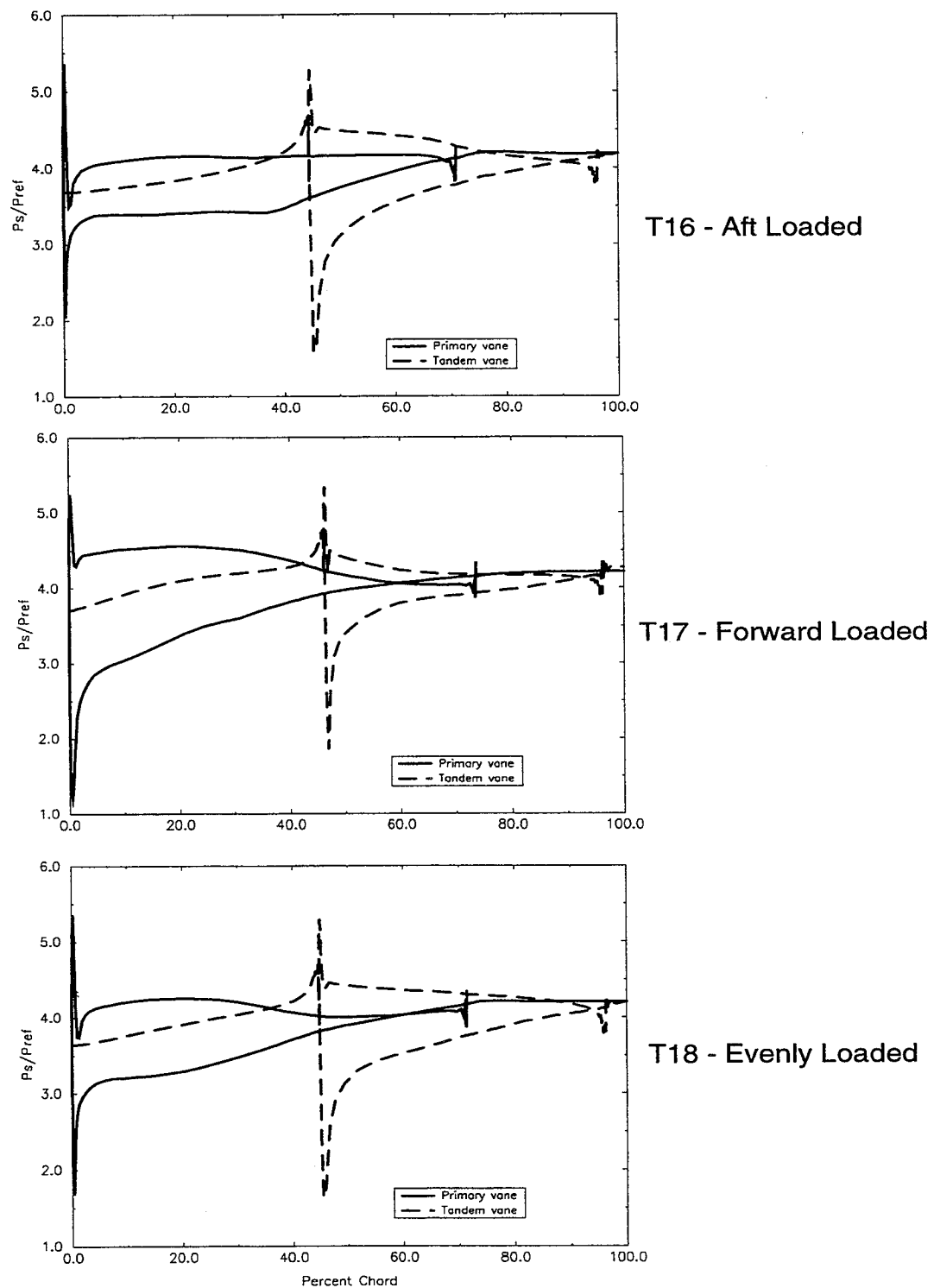
Figure 5-10. Effect of primary vane camber on vane surface pressure gradient.
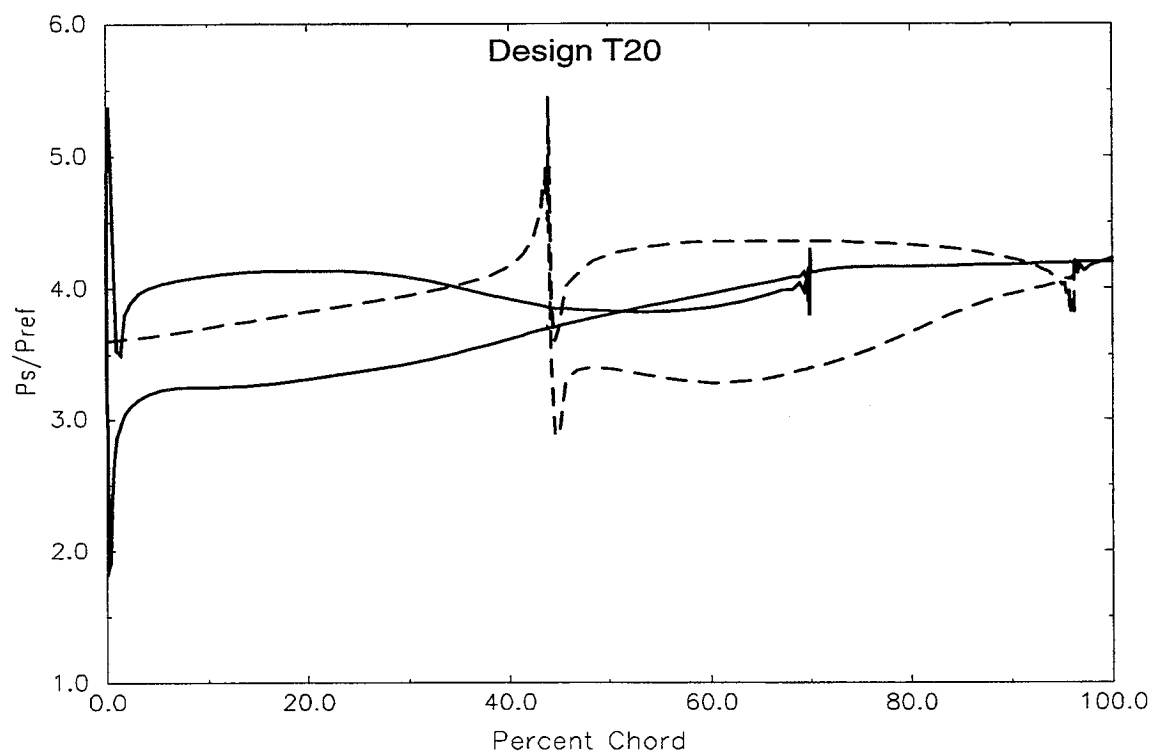
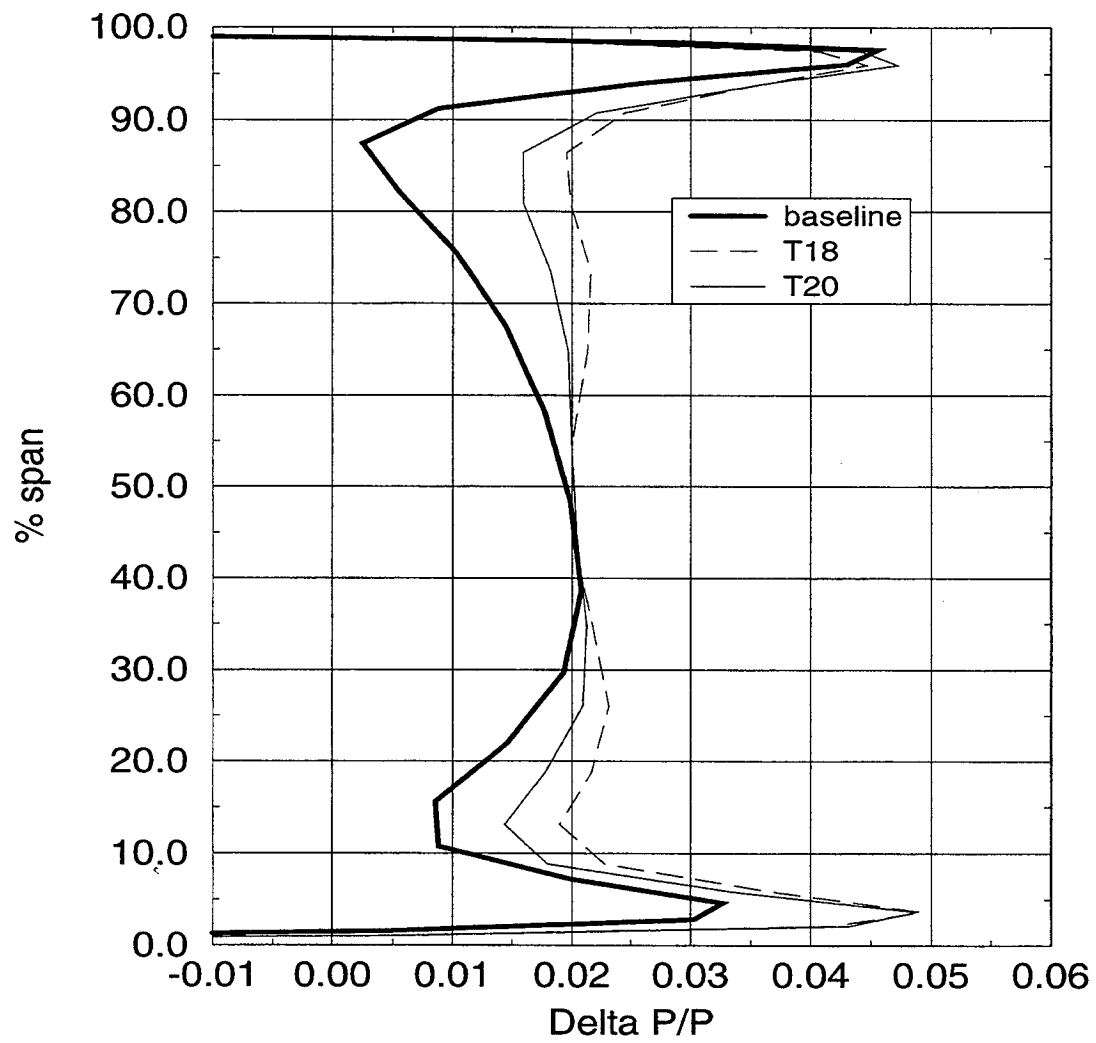*Figure 5-11. Blade loading of vane design T20 with lower tandem vane incidence.*

Figure 5-12. Spanwise profile of predicted total pressure loss.

5.3 Optimized Tandem Vane Configuration

The best designs from each trade study were combined to form the best overall tandem vane configuration. This included a 50% pitchwise location tandem vane (T02), an effective solidity of 1.85 (T07) and an even loading distribution (T18) with low tandem vane incidence (T20). This design, designated T21 and illustrated in Figure 5-13, had a mass-averaged total pressure loss of 2.19%, only slightly higher than the baseline vane. The radial profiles of total pressure loss are compared in Figure 5-14 showing the higher loss of the tandem vane design occurs in the 50% to 90% span range.

5.3.1 Off- Design Performance

The off-design performance figures for the baseline and T21 tandem vane configuration were determined using *ADPAC*. Each configuration was analyzed at several incidence values ranging from -14° to +8° delta from design. The exit static pressure supplied as a boundary condition in *ADPAC* was held constant for all cases. The total pressure loss as a function of incidence is presented in Figure 5-15 and shows that the tandem vane configuration has a lower minimum loss value than the conventional design. The tandem vane design also has a flatter loss bucket indicating a wider operating range of low loss performance compared to the baseline. These results indicate that a tandem vane configuration could be designed at a lower incidence level than a conventional vane design. This would allow the compressor to run at to a higher operating line before the vane stalls producing large amounts of loss. The off-design flow rate characteristics of the tandem vane configuration also supports this capability as shown in Figure 5-16. The tandem design is able to maintain a high flowrate at very low incidence levels compared to the baseline design which begins to drop flow rate as incidence goes more negative.

This study has shown that there is a potential benefit of a properly designed tandem vane configuration in improving the off-design performance of highly loaded compressors and suggests that this concept should be explored further.
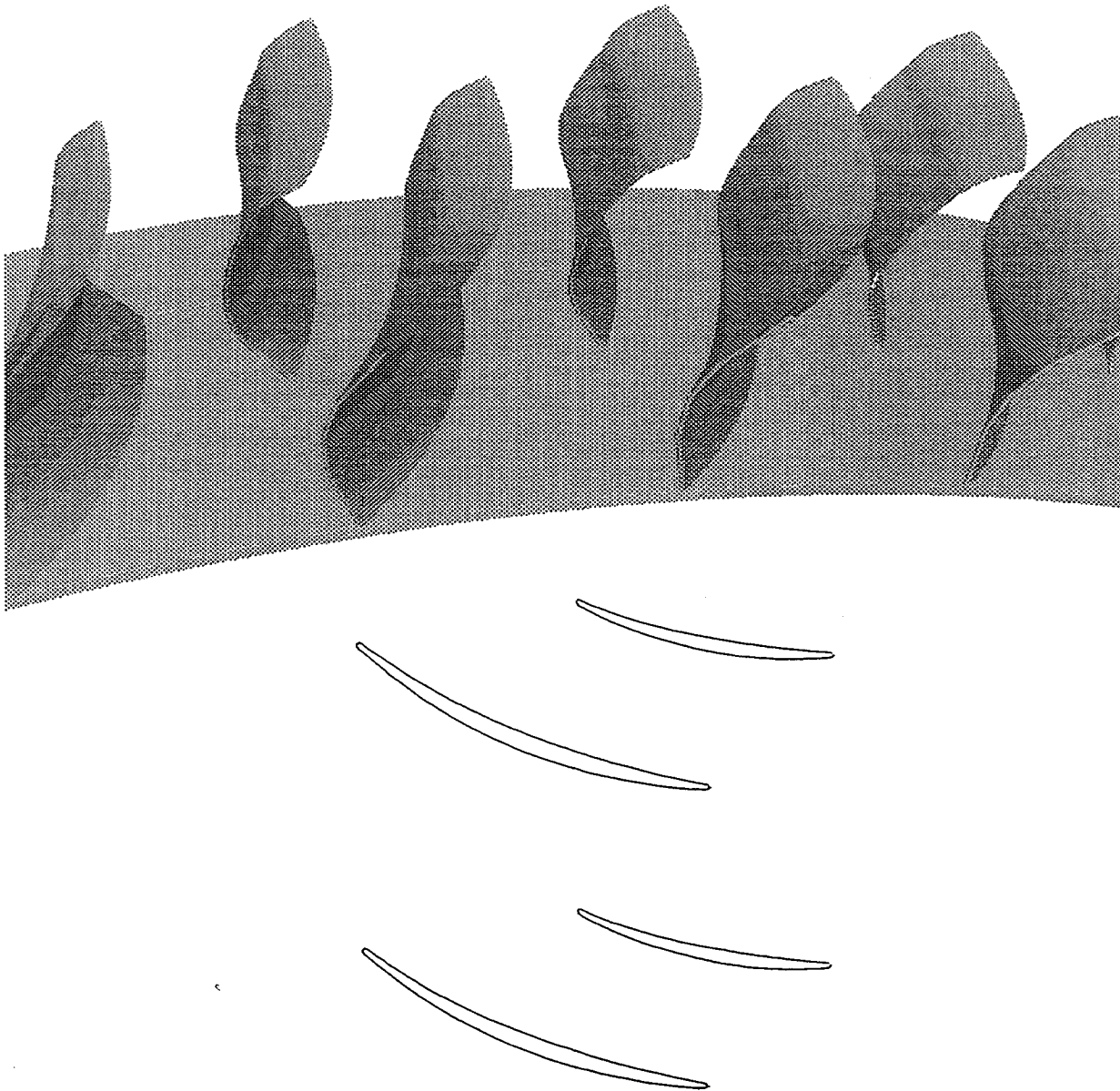
Figure 5–13. Final tandem vane design T21.

115
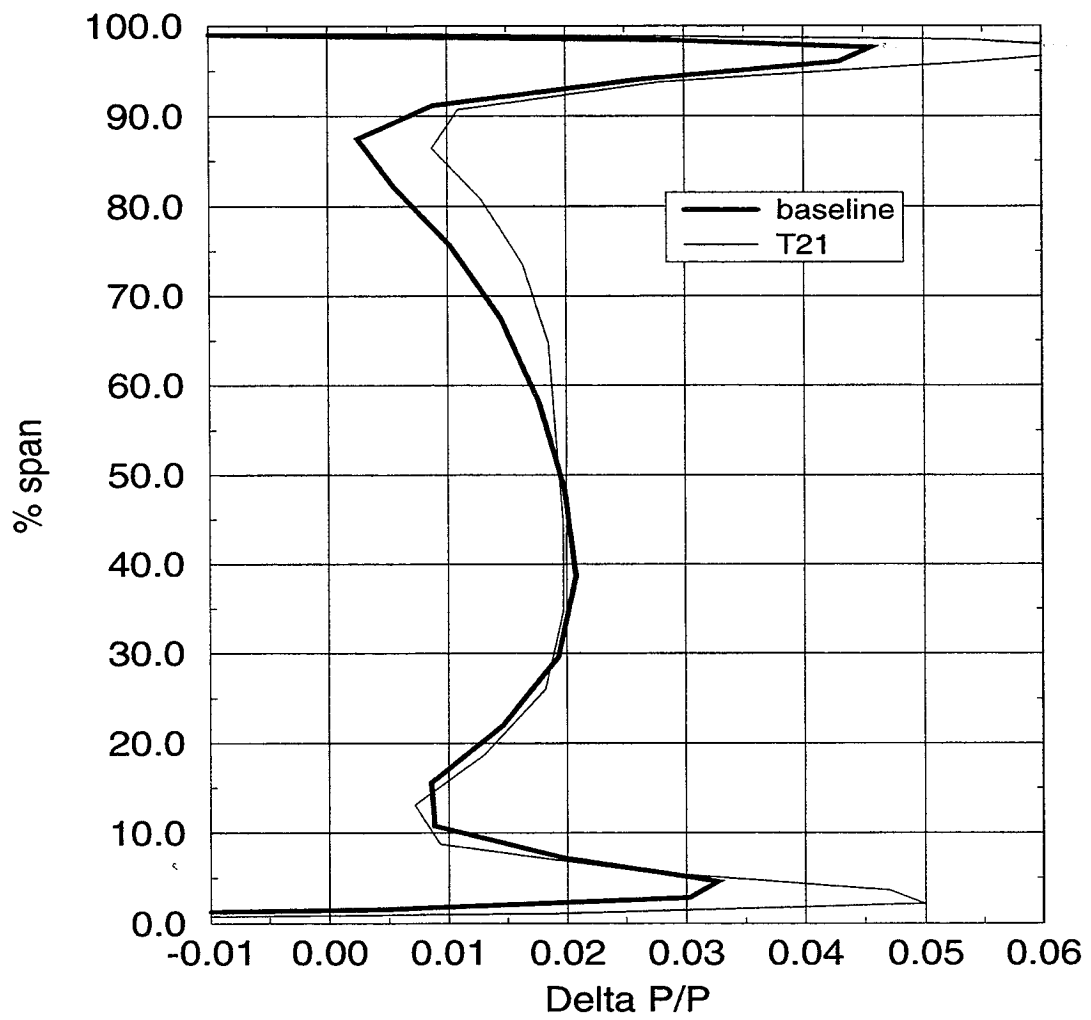
*Figure 5-14. Spanwise profile of predicted total pressure loss
for the optimum tandem design.*
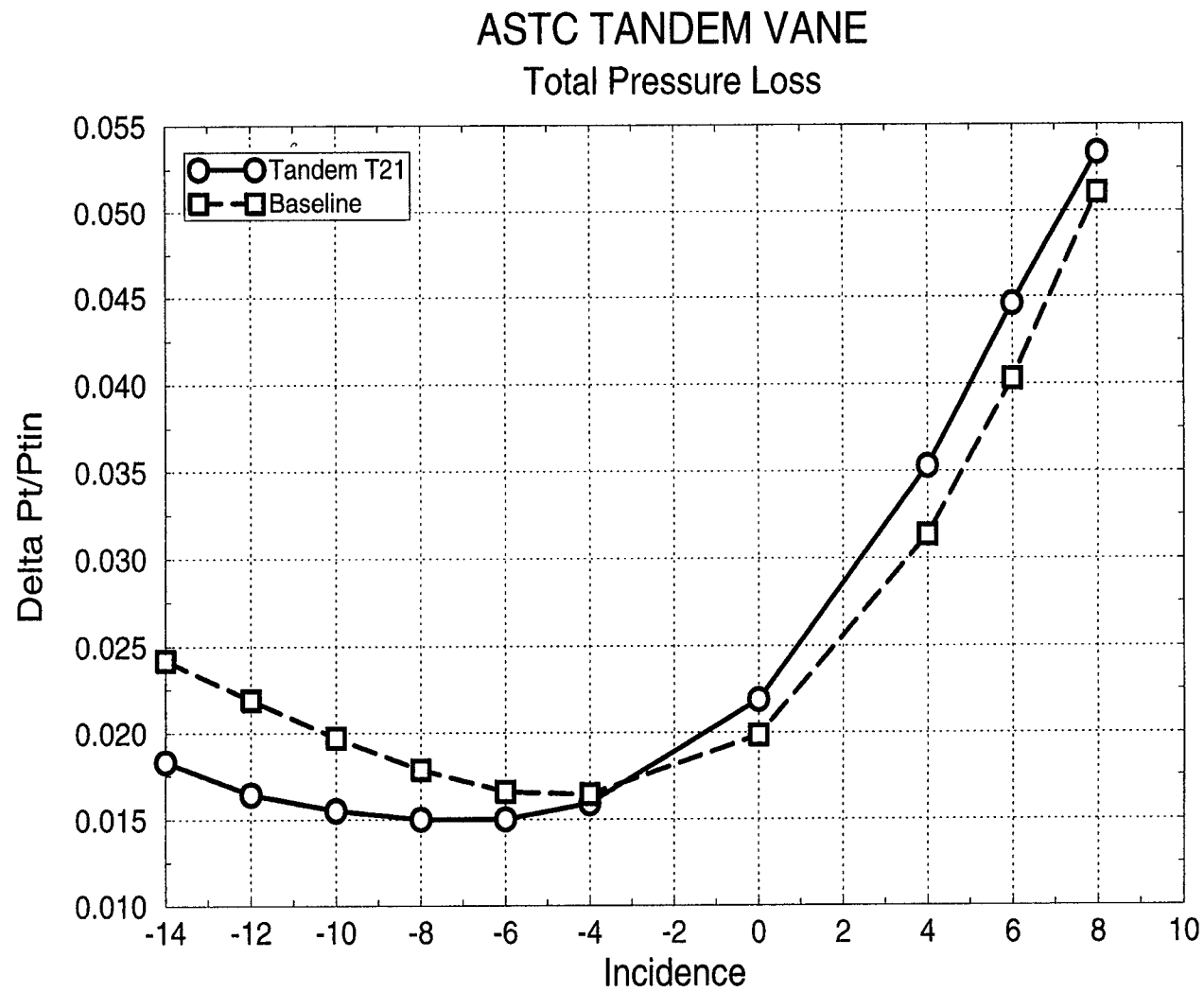
ASTC TANDEM VANE
Total Pressure Loss

Figure 5-15. Predicted total pressure loss as a function of incidence.
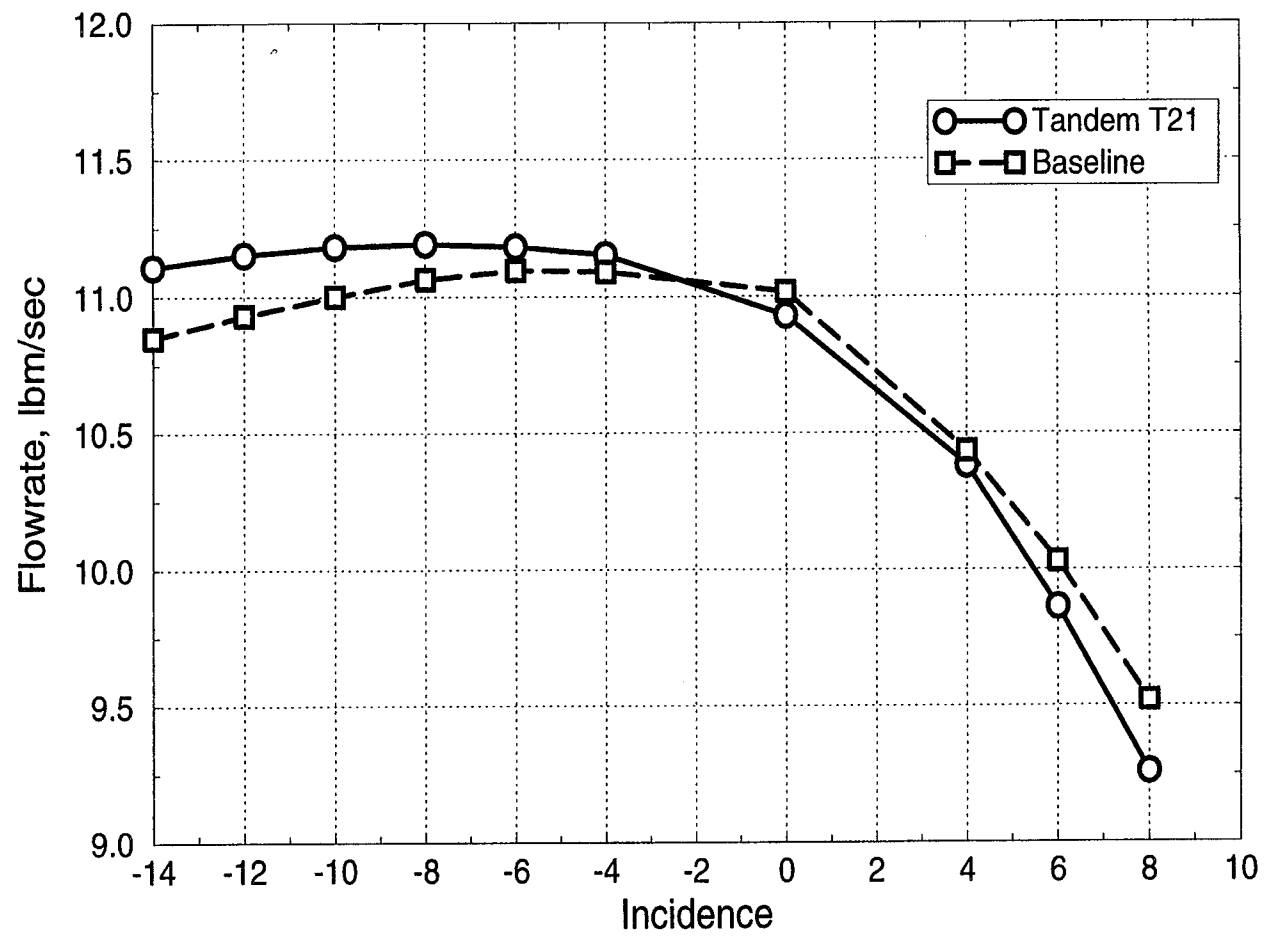
Figure 5-16. Predicted flowrate as a function of incidence.

6.0 REFERENCES

1. Adamczyk, J. J., "Model Equations for Simulating Flows in Multistage Turbomachinery", ASME Paper 85-GT-226, 1985.

2. Adamczyk, J. J., Mulac, R. A., Celestina, M. L., "A Model for Closing the Inviscid Form of the Average-Passage Equation System", ASME Paper 86-GT-227, 1986.

3. Adamczyk, J. J., Celestina, M. L., Beach, T. A., and Barnett, M., "Simulation of Three-Dimensional Viscous Flow Within a Multistage Turbine," ASME Paper 89-GT-152, 1989.

4. Brokopp, R. A., Gronski, R. S., "Small Engine Components Test Facility Compressor Testing Cell at NASA Lewis Research Center." AIAA Paper 92-3980, July 1992.

5. Hall, E. J., Delaney, R. A., and Bettner, J. L., "Investigation of Advanced Counterrotation Blade Configuration Concepts for High Speed Turboprop Systems: Task I - Ducted Propfan Analysis", NASA CR 185217, NASA Contract NAS3-25270, 1990.

6. Hall, E. J. and Delaney, R. A., "Investigation of Advanced Counterrotation Blade Configuration Concepts for High Speed Turboprop Systems: Task II - Unsteady Ducted Propfan Analysis - Final Report", NASA CR 187106, NASA Contract NAS3-25270, 1992.

7. Hall, E. J. and Delaney, R. A., "Investigation of Advanced Counterrotation Blade Configuration Concepts for High Speed Turboprop Systems: Task V - Counterrotation Ducted Propfan Analysis, Final Report", NASA CR 187126, NASA Contract NAS3-25270, 1992.

8. Hall, E. J., Topp, D. A., Heidegger, N. J., and Delaney, R. A., "Investigation of Advanced Counterrotation Blade Configuration Concepts for High Speed Turboprop Systems: Task VIII - Heat Transfer/Cooling Flow Analysis, Final Report", NASA Contract NAS3-25270, to be published, 1994.

9.   Hall, E. J. and Delaney, R. A., "Investigation of Advanced Counterrotation Blade Configuration Concepts for High Speed Turboprop Systems: Task V - Counterrotation Ducted Propfan Analysis, Computer Program Users Manual", NASA CR 187125, NASA Contract NAS3-25270, 1992.

10.   Hall, E. J., Topp, D. A., Heidegger, N. J., and Delaney, R. A., "Investigationof Advanced Counterrotation Blade Configuration Concepts for High Speed Turboprop Systems: Task VIII - Heat Transfer/Cooling Flow Analysis, Computer Program User's Manual", NASA Contract NAS3-25270, to be published, 1994.

11.   Jameson, A., Schmidt, W., and Turkel, E., "Numerical Solutions of the Euler Equations by Finite Volume Methods Using Runge-Kutta Time-Stepping Schemes," AIAA Paper 81-1259, 1981.

12.   Chima, R. V., "Inviscid and Viscous Flows in Cascades with an Explicit Multiple-Grid Algorithm", AIAA Journal Vol. 23, pp. 1156-1563, 1985.

13. Radespiel, R., Rossow, C., and Swanson, R. C., "Efficient Cell Vertex Multigrid Scheme for the Three-Dimensional Navier-Stokes Equations", AIAA Journal, Vol. 28, No. 8, pp. 1464-1472, 1990.

14. Jameson, A., and Baker, T. J., "Solution of the Euler Equations for Complex Configurations," AIAA Paper 83-1929, 1983.

15. Jorgensen, P. C. E., and Chima, R. V., "An Unconditionally Stable Runge-Kutta Method for Unsteady Flows," NASA TM 101347, 1989.

16. Baldwin, B. S., and Lomax, H. "Thin Layer Approximation and Algebraic Model for Separated Turbulent Flows", AIAA Paper 78-257, 1978.

17. Goyal, R. K., and Dawes, W. N.,"A Comparison of the Measured and Predicted Flowfield in a Modern Fan-Bypass Configuration", ASME Paper 92-GT-298, 1992.

18. Hall, E. J., and Delaney, R. A., "3D Euler Analysis of Ducted Propfan Flowfields", AIAA Paper 90-3034-CP, 1990.

19. Hall, E. J., and Delaney, R. A., "Time-Dependent Aerodynamic Analysis of Ducted and Unducted Propfans at Angle of Attack", ASME Paper 91-GT-190, June, 1991.

20. Hall, E. J., Topp, D. A., and Delaney, R. A., "Aerodynamic/Heat Transfer Analysis of Discrete Site Film Cooled Turbine Airfoils", AIAA Paper 94-3070, June, 1994.

21. Hall, E. J., Crook, A. J., and Delaney, R. A., "Aerodynamic Analysis of Compressor Casing Treatment with a 3-D Navier-Stokes Solver", AIAA Paper 94-2796, June, 1994.

22. Weber, K. F., Delaney, R. A., "Viscous Analysis of Three-Dimensional Turbomachinery Flows on Body Conforming Grids Using an Implicit Solver", ASME Paper 91-GT-205, 1991.

23. Benek, J. A., Buning, P. G., and Steger, J. L., "A 3-D Grid Embedding Technique", AIAA Paper 85-1523, 1985.

24. Thomas, P. D., "Numerical Method for Predicting Flow Characteristics and Performance of Nonaxisymmetric Nozzles--Theory." Langley Research Center, NASA CR 3147, September 1979.

25. Miller, D. P., Prahst, P. S., "Inlet Flow Test Calibration for a Small Axial Compressor Facility. Part I- Design and Experimental Results", AIAA Paper 94-2690, 1994.

REPORT DOCUMENTATION PAGE

Form Approved
OMB No. 0704-0188

1. AGENCY USE ONLY (Leave blank)	2. REPORT DATE March 1997	3. REPORT TYPE AND DATES COVERED Final Contractor Report

4. TITLE AND SUBTITLE

Small Engine Technology
Task 4: Advanced Small Turboshaft Compressor (ASTC) Performance
and Range Investigation

5. FUNDING NUMBERS

WU–505–62–10
C–NAS3–27394

6. AUTHOR(S)

Jeff L. Hansen and Robert A. Delaney

7. PERFORMING ORGANIZATION NAME(S) AND ADDRESS(ES)

Allison Engine Company
2059 S. Tibbs Avenue
Indianapolis, Indiana 46241

8. PERFORMING ORGANIZATION REPORT NUMBER

E–10333

9. SPONSORING/MONITORING AGENCY NAME(S) AND ADDRESS(ES)

National Aeronautics and Space Administration
Lewis Research Center
Cleveland, Ohio 44135–3191

10. SPONSORING/MONITORING AGENCY REPORT NUMBER

NASA CR–198503

11. SUPPLEMENTARY NOTES

12a. DISTRIBUTION/AVAILABILITY STATEMENT

Unclassified - Unlimited
Subject Category 07

This publication is available from the NASA Center for AeroSpace Information, (301) 621–0390.

12b. DISTRIBUTION CODE

13. ABSTRACT (Maximum 200 words)

This contact had two main objectives involving both numerical and experimental investigations of a small highly loaded two-stage axial compressor designated Advanced Small Turboshaft Compressor (ASTC) which had a design pressure ratio goal of 5:1 at a flowrate of 10.53 lbm/s. The first objective was to conduct 3–D Navier Stokes multistage analyses of the ASTC using several different flow modelling schemes. The second main objective was to complete a numerical/experimental investigation into stall range enhancement of the ASTC. This compressor was designed under a cooperative Space Act Agreement and all testing was completed at NASA Lewis Research Center. For the multistage analyses, four different flow model schemes were used, namely: (1) steady-state *ADPAC* analysis, (2) unsteady *ADPAC* analysis, (3) steady-state *APNASA* analysis, and (4) steady state *OCOM3D* analysis. The results of all the predictions were compared to the experimental data. The steady-state *ADPAC* and *APNASA* codes predicted similar overall performance and produced good agreement with data, however the blade row performance and flowfield details were quite different. In general, it can be concluded that the *APNASA* average-passage code does a better job of predicting the performance and flowfield details of the highly loaded ASTC compressor.

14. SUBJECT TERMS

Turbomachinery axial compressor; Tandem vane; Forward sweep;
Computational fluid dynamic Navier-Stokes

15. NUMBER OF PAGES 131
16. PRICE CODE A07

17. SECURITY CLASSIFICATION OF REPORT Unclassified	18. SECURITY CLASSIFICATION OF THIS PAGE Unclassified	19. SECURITY CLASSIFICATION OF ABSTRACT Unclassified	20. LIMITATION OF ABSTRACT

NSN 7540-01-280-5500

Standard Form 298 (Rev. 2-89)
Prescribed by ANSI Std. Z39-18
298-102

National Aeronautics and
Space Administration

Lewis Research Center
21000 Brookpark Rd.
Cleveland, OH 44135-3191